THE UNIVERSITY *of* EDINBURGH

A microscopic study of the freeze-thaw stability of particle-stabilised emulsions

Katy Louise Dickinson

Doctor of Philosophy
The University of Edinburgh
May 2019

Abstract

Particle-stabilised, or Pickering, emulsions are widely used in the food and personal care industries and are present in common household products such as homogenised milk and food spreads. Pickering stabilisation has also been suggested as a method of increasing product shelf life over conventional surfactant stabilisation. It is therefore important to characterise the behaviour and stability of Pickering emulsions subjected to processes used in industry and daily life. These processes have the potential to alter the taste of food products or the effectiveness of personal care or pharmaceutical products. Freezing is one process of interest as it is used for product transport and in order to increase shelf life. Some products are also used when frozen, such as ice cream and frozen desserts.

In this thesis, confocal fluorescence microscopy is used to study the microscopic behaviour of model water-in-oil Pickering emulsions subjected to freeze-thaw cycling of the continuous phase. Hexadecane oil and poly(methyl methacrylate) particles are used and both are fluorescently labelled, allowing all three emulsion components to be distinguished individually.

Initially, we study the behaviour of the oil alone, both experimentally and in simulation, under uniform and non-uniform cooling. In non-uniform cooling, the sample is cooled more rapidly from one end, whereas in the uniform setup the sample is cooled evenly. Simulation results show that the two setups lead to different temperature and fluid flow profiles throughout the sample: the non-uniform setup causes a temperature gradient through the oil which is essentially eliminated in the uniform setup. Experiments confirm the presence/absence of these gradients and show that the temperature gradient affects the crystal growth in the oil.

Dilute emulsions are studied under two different non-uniform configurations. In the first, droplets interact with crystals growing from many directions.

Deformation of the droplets is observed as growing crystals progressively trap the droplets, stretching them towards parts of the sample where the oil is still liquid. The droplet deformation is characterised via image analysis to compare the droplet shape before and after freeze-thaw cycling. Irreversible shape changes are explained by the behaviour of the particles on the interface. Particles initially jammed on the interface become unjammed as the interfacial area increases during droplet deformation in the freezing process. Upon thaw, the particles rejam at a lower packing fraction meaning that droplets are permanently deformed. In the second configuration, the droplets interact with a moving solidification front in which crystal growth is unidirectional. Again deformation of the droplets is observed as droplets are trapped by the front. In some cases particles are trapped and pulled off the droplet interface, temporarily releasing the droplet and leaving it with a lower surface coverage of particles. In both cases, particle behaviour at the interface is key in determining the droplet behaviour.

Finally undiluted emulsions are subjected to freeze-thaw cycles under both uniform and non-uniform conditions. In both cases droplets are deformed by the crystal growth, but during non-uniform freezing biliquid foam regions are formed which are not present in the uniformly frozen samples. The effects of droplet size and cooling rate are also explored for uniform freezing. In both cases, irreversible changes are observed in the emulsion structure as a result of the process. As in the single droplet case, these results suggest that particles at the interface become unjammed during the freeze cycle and upon thawing re-jam at a different packing fraction. Here deformation is enhanced by partial coalescence which promotes jamming in a deformed state through reduction of interfacial area at fixed volume. In the absence of particles, similar freeze-thaw cycling of surfactant emulsions does not cause the same irreversible change to the emulsion structure as in the particle-stabilised emulsions. In addition, under certain conditions, Pickering emulsions after a freeze-thaw cycle exhibit some bicontinuity, suggesting that freeze-thaw cycling may be a promising route to producing bicontinuous emulsions.

Collectively, these results improve our understanding of the behaviour of particle-stabilised emulsions under freeze-thaw cycling, which is an industrially relevant process. They show the importance of the interfacial particles in controlling emulsion structure and they provide insight into the interaction between soft materials, like droplets, and hard materials, such as ice crystals, at the microscopic level. Although freezing can prolong shelf life, and Pickering

stabilisation can enhance emulsion stability, the combination of these two must be treated with care as together they can cause irreversible structural damage, reducing rather than enhancing product stability.

Lay Summary

It is a fairly well known fact that oil and water do not mix and will generally separate if mixing is attempted. However, it is possible to force oil and water to mix and this is the foundation of products such as butter and salad dressing. These mixtures contain droplets of one liquid dispersed in the other and require an extra ingredient to prevent the droplets from joining together. This extra component, known as an emulsifier, sits on the surfaces of the droplets and comes in two main forms; the first is a surfactant - a molecule with one end which is soluble in water and one end soluble in oil - and the second is a small solid particle. These oil-water mixtures are called emulsions and in the case of solid particle stabilisers they are called Pickering emulsions.

In Pickering emulsions, the solid particles on the droplet surface make a physical barrier around the droplet, so the liquid inside the droplets cannot flow into another droplet. This type of emulsion is interesting because it can be very stable, meaning it takes longer for the oil and water to separate. This is a useful property for many products used in everyday life, like milk and mayonnaise.

In this thesis, experiments studying the behaviour of Pickering emulsions during freezing and thawing are carried out. Freezing is an important industrial process both for products that are consumed while frozen and for those which are frozen to extend their shelf life. Therefore it is useful to understand how freezing changes the shape of the emulsion droplets and whether or not freezing causes the oil and water to separate because doing so could alter the texture or taste of food products and reduce the effectiveness of personal care products and pharmaceuticals.

Emulsions are studied both when the droplets are close together, or even touching, and when the droplets are far enough apart that they do not come into contact at all. In addition, the importance of how the emulsions are frozen is studied by considering two different cases; first, when the temperature throughout the

emulsion is uniform at any given time and second when one end of the emulsion sample is cooled more quickly than the other, so the temperature across the emulsion varies.

The results show that the way samples are cooled affects their final structure. Uniformly cooled samples appear uniform after a freeze-thaw cycle, while non-uniformly cooled samples show a range of structures from individual droplets to foam-like areas. In both cases, the emulsion is permanently damaged as a result of the process. Droplets are deformed due to the interaction with the oil crystals so that even when droplets are observed alone using a very dilute emulsion, the droplets deform either by stretching or crumpling. The way the droplets deform depends on the growth of the oil crystals, whether they grow from one direction towards the droplet or from many directions around the droplet. The droplets do not usually return back to their original spherical shape after freeze-thaw cycles.

The behaviour of the droplets is a result of the particles on the droplet surface. As the droplet is deformed during freezing, the surface area of the droplet increases and the particles can move around on the droplet interface. When the sample thaws, the droplet begins to relax back towards a sphere, but before it can do so, the particles become jammed on the interface in a different arrangement to their initial configuration and so the droplets become 'stuck' in a non-spherical shape.

Although particle-stabilised emulsions are considered to have good stability in general, this may not be true when freezing is involved. Damage to the emulsion structure is a problem for any applications where the emulsion has been carefully designed for a specific function and so care must be taken when using Pickering emulsions for products which will require freezing during their processing or use.

Declaration

I declare that this thesis was composed by myself, that the work contained herein is my own except where explicitly stated otherwise in the text, and that this work has not been submitted for any other degree or professional qualification except as specified.

The work presented in Chapter 7 has been submitted to arXiv and can be found in Reference [1].

(*Katy Louise Dickinson, May 2019*)

Acknowledgements

There are a number of people who I would like to thank without whom this thesis would never have been started, let alone completed. Firstly huge thanks to my supervisor Job Thijssen for his patience, support and encouragement throughout. Thanks also to my second supervisor Paul Clegg for his advice and support.

Thanks to Andy Schofield for the provision of particles and all the lab advice and to Rolly Wiegand for his help with the two-photon microscopy. Special thanks go to Anne Pawsey for her friendship, encouragement, advice on all things lab-related and for introducing me to outreach which has been a hugely enjoyable experience.

Thanks to the CM-CDT both for funding me and giving me the opportunity to spend three months on an industrial placement with Macphie.

Thank you to Sylvain Deville and the group at CNRS/Saint Gobain in Cavaillon for all their help with experiments in their lab. It was a pleasure to spend two sunny weeks in France obtaining some really interesting results.

The last four years would not have been the same without my lovely office-mates in room 1511; to Ana, Carolina, Hanna and Yair, thank you for all our conversations, putting up with my lab issues and for keeping me sane. In addition thank you to my other friends in JCMB, in particular to Katherine, Ava, Xuemao and Martina.

Lastly, but by no means least, thanks go to my family and friends, especially to my Dad and my sisters Hannah and Emily for their love and support throughout.

Contents

List of Figures

List of Tables

Chapter 1

Introduction

Emulsions are found in a range of everyday, household products such as milk, margarine, mayonnaise and salad dressing as well as in some cosmetics and pharmaceuticals. They are one of a class of materials which can neither be described as crystalline solids, nor as simple liquids but are instead known as 'soft matter'. These materials are characterised by mesoscopic lengthscales, *i.e.* above atomic length scales but below macroscopic length scales, and display at least some local order even though long-range crystalline order may be absent. They also exhibit large-scale responses to weak forces and can be affected by thermal fluctuations resulting, for example, in Brownian motion [2, 3]. Other examples of soft matter include gels, foams and polymer solutions.

Emulsions are defined simply as droplets of one liquid dispersed in another, either water-in-oil or oil-in-water. The two liquids do not mix and typically separate unless a stabiliser is added. This stabiliser commonly takes the form either of surfactants such as lecithin, which have a head group to associate with one liquid and a tail group which associates with the other, or of solid particles which physically prevent liquid transfer between droplets. The latter are known as Pickering emulsions and are the subject of this thesis.

As emulsions are industrially relevant, there are many processes to which emulsions are subjected and in each case their stability is key. The emulsion structure is designed for a purpose and must therefore be maintained in order for the product to function as intended. One process of particular interest is freezing - a technique which industry and consumer alike make use of on a regular basis both for product storage and transport as well as enhanced shelf life. Freezing

is commonly characterised by crystal growth within the freezing phase. These crystals interact with any structure around them and there are multiple factors which affect this interaction, such as crystal size and growth speed. These factors can be controlled by the freezing conditions through parameters such as cooling rate and final temperature.

Pickering stabilisation has been suggested as a method for improving emulsion stability over surfactant stabilisation and thus improving product shelf life. However, the literature is divided as to whether this is true in the case of emulsions undergoing freeze-thaw cycles and as to how factors such as cooling rate affect the outcome [4, 5]. In some cases, Pickering stabilisation has been shown to improve emulsion freeze-thaw stability [6, 7] but understanding of the microscopic behaviour of Pickering emulsions during freezing is limited.

In this thesis, the behaviour of model particle-stabilised emulsions subjected to freeze-thaw cycles of the continuous phase is studied. A range of different freezing conditions are studied with varying degrees of crystal growth control in order to gain insight into the interaction between particle-stabilised droplets and crystal growth. Experimental studies on the behaviour of the continuous phase alone alongside simulations are also carried out to assist in this understanding.

This thesis is laid out as follows.

Chapter 2 details the relevant theoretical background on particle-stabilised emulsions and factors affecting emulsions freeze-thaw stability. It also covers the crystal nucleation theory for homogeneous and heterogeneous nucleation. Chapter 3 discusses the materials and experimental techniques used in multiple chapters of this thesis. Chapter 4 contains simulations of the temperature and solid-liquid interface velocity profile in oil freezing under two distinct conditions - uniform and non-uniform freezing. It also covers the effect of millimetre-sized water droplets on those profiles. Experimental observations of crystallisation and thermal behaviour of oil undergoing freeze-thaw cycles under uniform and non-uniform freezing are then discussed.

Chapter 5 discusses the effects of oil crystallisation on individual particle-stabilised droplets and the ramifications for droplet shape. In Chapter 6, a novel cryo-confocal temperature stage is used to study the effects of uni-directional freezing on droplets, probing directly the interaction between droplets and a freezing front. Chapter 7 builds on the single droplet results by exploring the collective effects of droplets in an emulsion during freeze-thaw cycling of the

continuous phase. It also explores the effects of cooling rate and droplet size on emulsion freeze-thaw stability.

Chapter 8 contains preliminary results on the formation of bicontinuous particle-stabilised structures via freeze-thaw cycling. Finally in Chapter 9 the results presented in this thesis are summarised along with their implications and suggested future work.

Chapter 2

Background

This chapter explains the relevant physics behind the systems and processes used in this thesis. First, the physics of Pickering emulsions and emulsion stability are discussed. Then the relevance of freezing and the necessity of understanding the process and its effects on emulsions is discussed along with the concepts of homogeneous and heterogeneous crystal nucleation.

2.1 Emulsions

Emulsions are thermodynamically metastable systems consisting of one immiscible liquid dispersed in another, typically water-in-oil or oil-in-water [8]. In the absence of any additional stabilisers or electrostatic effects [9], phase separation of the two fluids will occur because doing so reduces the interfacial area between them. Due to the interfacial tension which exists at the liquid-liquid interface, larger interfacial area leads to an increase in free energy as described by the equation

$$\Delta G = \gamma_{\mathrm{ow}} \Delta A \ , \tag{2.1}$$

where ΔG is the change in interfacial free energy between a phase-separated state and a mixed state, γ_{ow} is the oil-water interfacial tension and ΔA the change in interfacial area [10]. Therefore, it is energetically favourable to lower the interfacial area, *i.e.* phase separate.

2.1.1 Laplace pressure

For a curved liquid surface in equilibrium, the interfacial tension leads to a pressure difference across the surface. To force a planar surface to curve, the pressure must be greater on the 'inside', or concave side of the curve, meaning for a droplet such as an emulsion droplet, the pressure on the inside of the droplet, P_i, is greater than the pressure outside the droplet, P_o. The difference between these two pressures, ΔP is related to the two principal radii of curvature of the surface, R_1 and R_2, via the Young-Laplace equation [11, 12]:

$$\Delta P = P_i - P_o = \gamma(\frac{1}{R_1} + \frac{1}{R_2}) \ , \tag{2.2}$$

where γ is the surface tension and ΔP is also known as the Laplace pressure, P_L. For a spherical droplet, $R_1 = R_2 = R$, therefore

$$P_L = \frac{2\gamma}{R} \ . \tag{2.3}$$

2.1.2 Emulsion stability

There are four main destabilisation mechanisms which lead to the phase separation of an emulsion: creaming/sedimentation, where the density mismatch between droplets and continuous phase causes the droplets either to rise to the top (cream) or fall to the bottom (sediment); flocculation, in which droplets aggregate into clusters; Ostwald ripening, where liquid with limited solubility in the continuous phase is transferred from small droplets into larger droplets, causing smaller droplets to shrink and larger ones to grow; and coalescence, where multiple droplets make contact and are joined together into a single droplet with a lower surface to volume ratio. Each of these is shown schematically in Fig. 2.1.

While each of these processes individually does not necessarily lead to phase separation, both creaming and flocculation can be followed by coalescence which, if unhindered, will ultimately cause phase separation [13]. The time taken for these processes may vary from one emulsion to another, and some emulsions will be stable against one or more of these depending on any stabilisers present [10].

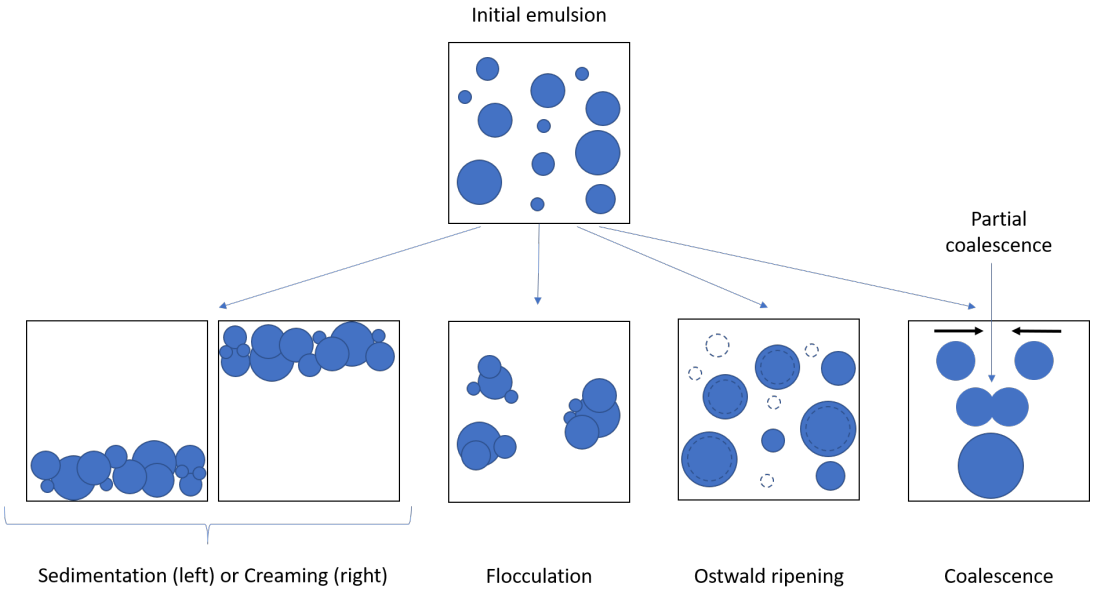

Figure 2.1 *Schematic showing the four primary mechanisms by which emulsions are destabilised. Droplets are shown in blue with a white continuous phase. See text for details.*

2.1.3 Surfactant-stabilised emulsions

One route to obtaining kinetic emulsion stability, is to lower the interfacial tension of the water-oil interface. This is achieved by the addition of surfactants, amphiphilic molecules with a hydrophilic head group and a hydrophobic tail [2]. These molecules preferentially attach to the water-oil interface, reducing the interfacial tension and thus the energy cost of forming the increased water-oil surface area obtained during emulsion formation compared to a flat water-oil interface. They can reduce droplet coalescence by repulsive interactions between surfactants on neighbouring droplets through charge or steric mechanisms [14, 15].

2.1.4 Pickering emulsions

An alternative route to obtaining emulsion stability is to provide a physical barrier against coalescence by the addition of interfacial particles, producing particle-stabilised emulsions [16]. Particle-stabilised emulsions, otherwise known as Pickering or Pickering-Ramsden emulsions, have been studied since their discovery at the turn of the 20th century [17, 18], and interest has increased

over recent years as their range of applications has increased [19–21].

Particle stabilisation

In order to form a particle-stabilised emulsion, the stabilising particles must be partially wetted by both liquids, a characteristic defined by the three-phase contact angle, θ, shown in Fig. 2.2. The contact angle is typically measured through the water phase, thus hydrophilic particles have $\theta < 90\ ^\circ$, while hydrophobic particles have $\theta > 90\ ^\circ$. In the particular case of $\theta = 90\ ^\circ$, particles are said to be neutrally wetting. This contact angle is also the primary factor in determining which is the continuous and which the dispersed phase in an emulsion: hydrophilic particles typically stabilise an oil-in-water emulsion and hydrophobic particles a water-in-oil emulsion, thus the continuous phase is generally the one in which the larger proportion of the particle is present [10, 22]. It has been shown that other factors, such as the volume ratio of oil to water, can also affect which phase is continuous [23].

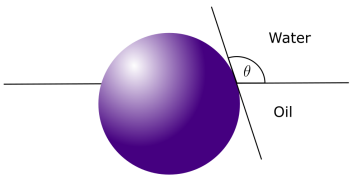

Figure 2.2 *Solid particle at a water-oil interface. The position of the particle at the interface depends on the three-phase contact angle θ as measured through the water phase.*

Once a particle reaches and adsorbs onto the interface, there is an energy cost, E, associated with its detachment, given by

$$E = \pi r^2 \gamma_{\mathrm{ow}} (1 - |\cos\theta|)^2 \ , \tag{2.4}$$

where γ_{ow} is the oil-water interfacial tension, r the radius of the particles and θ the three-phase contact angle [23]. For micron-sized solid particles at a water-alkane interface, $\gamma_{\mathrm{ow}} \approx 50$ mN/m [24, 25] and the detachment energy, for a contact angle of $\theta = 90°$, is $\mathcal{O}(10^7)\ k_{\mathrm{B}}T$ (Boltzmann constant k_{B} and room temperature T) [26]. Even for contact angles approaching 160°, as for the systems in this thesis, E is

still many orders of magnitude higher than $k_{\mathrm{B}}T$. Therefore without any external energy input, the particles are irreversibly adsorbed to the interface. This is unlike the situation in surfactant-stabilised emulsions where the attachment energy is $\mathcal{O}(k_{\mathrm{B}}T)$ and thus the surfactants adsorb and desorb on a much faster timescale [23].

Particle choice in Pickering emulsions is important both in size and composition because of the effects on the resultant emulsion stability as well as the requirements of the desired application. Particle sizes typically range from tens of nanometres up to a few microns [20, 27]. Both organic and inorganic particles have been used, with materials varying from silica [28], clays [29] and latex [27] to food-grade particles such as starch granules [30] and fat crystals [31, 32]. Although model Pickering emulsions are commonly stabilised by spherical particles, a range of other shapes, such as discs [29], rods [33] and cubes [34], have also been explored, as well as food-grade particles which are often non-spherical [19].

Droplet size

In a Pickering emulsion, the droplet diameter, D, is determined both by the total volume of droplet phase added, V_{d}, and the mass of particles added, m_{P}, according to the following relation

$$\frac{1}{\langle D \rangle} = \frac{s_{\mathrm{f}} m_{\mathrm{P}}}{6 V_{\mathrm{d}}} \ , \tag{2.5}$$

where s_{f} is the specific surface area. This assumes that particles are spherical and that all the particles reach the liquid interface [35, 36]. The specific surface area can be estimated by considering the total surface area of all the droplets and how it is covered by the particles [37]. The surface area, A, is given by

$$A = N A_{\mathrm{d}} = N \pi D^2 \ , \tag{2.6}$$

where A_{d} is the surface area of a single droplet and N the number of droplets. Given that the number of droplets is equal to

$$N = \frac{V_{\mathrm{d}}}{V_{\mathrm{droplet}}} = \frac{6 V_{\mathrm{d}}}{\pi D^3} \ , \tag{2.7}$$

where V_{droplet} is the volume of a single droplet, Equation (2.6) yields an expression for A as

$$A = \frac{6V_{\text{d}}}{D} \ . \tag{2.8}$$

Now considering the area of interface taken up by the particles, assuming the particles have a contact angle of 90°, this can be expressed as some proportion C of the total surface area A, giving a second expression for A as

$$CA = nA_{\text{p}} = \left(\frac{m_{\text{p}}}{m_{\text{single}}}\right)\left(\pi {r_{\text{p}}}^2\right) \ , \tag{2.9}$$

where n is the number of interfacial particles, A_{p} the area taken up by a single particle, m_{p} is the mass of particles added, m_{single} is the mass of a single particle and r_{p} the radius of a particle. This leads to

$$A = m_{\text{p}}\frac{3}{4}\frac{1}{\rho_{\text{p}} r_{\text{p}} C} \ , \tag{2.10}$$

where ρ_{p} is the density of a particle. Equating this to Equation (2.8) and then comparing to Equation (2.5) shows that s_{f} can be expressed as

$$s_{\text{f}} = \frac{3}{4C\rho_{\text{p}} r_{\text{p}}} \ . \tag{2.11}$$

Using Equations (2.5) and (2.11) the expected droplet size of an emulsion can be calculated. These equations can also be used with the measured average droplet size in an emulsion in order to determine a value for s_{f}, providing information about the configuration of the particle layer [35].

The value of s_{f} depends on the proportion of the interface taken up by particles, C, which in the ideal case of hexagonally close packed, monodisperse particles is equal to $\pi/(2/\sqrt{3}) \approx 0.9$ [35]. A higher measured value for s_{f} indicates either particle clustering or the formation of a multilayer at the interface [38] while a lower observed value indicates either that the particles have not all reached the interface, or that the particles are more loosely packed. It has been shown that in certain circumstances emulsions can be stable with lower surface coverage, even with patches of bare interface [39, 40].

Preparation of Pickering emulsions

Experimentally, Pickering emulsion preparation requires two steps: first, dispersal of the particles into their preferred fluid phase and second droplet creation via shear. While droplet size is controlled by the volume fraction and size of particles, the shear rate also affects the obtainable droplet size because the shear must generate sufficient liquid-liquid interface for all the particles added into the system. Shear via ultrasound or homogenizer can produce sub-micron-sized droplets, while gentle stirring or shaking produces droplets hundreds of microns to millimetres in diameter, with intermediate droplet sizes produced using, for example, a rotor stator with a range of shear rates [20]. As shear is applied and droplets are created, particles from the continuous phase will attach to the droplet interfaces. Limited coalescence then takes place and the average droplet size will increase via droplet coalescence until it reaches the limiting value set by the mass of particles in the system and the specific surface area according to Equation (2.5) [36, 37]. In the case of close packing, this is the point where there is just enough liquid interface to accommodate all the particles.

Pickering emulsion stability

The use of particle stabilisation in emulsions is a good method for overcoming some of the destabilisation mechanisms discussed in Section 2.1.2. Firstly it can prevent coalescence because the particles provide a physical barrier, meaning the fluid in the two droplets cannot come into contact unless particles are expelled from the interface, a phenomenon which has a high energy cost. For lower surface coverage of particles, it is possible for droplets to begin to coalesce as particles are able to move laterally, creating a region of bare interface in the contact region [41]. However, this process is usually arrested by the jamming of particles at the interface; for two droplets to coalesce to a single spherical droplet, the surface area of the coalesced droplet is smaller than the two separate droplets given the volume is fixed, thus the coalescence will be arrested when the particles fully cover the droplets (see Fig. 2.3) [42].

By a similar argument, Ostwald ripening is prevented because to remove fluid from smaller droplets would again require removal of particles from the interface [29, 43] so while this process may occur during emulsion formation, given a high enough surface coverage of particles it will not happen at later times. Creaming

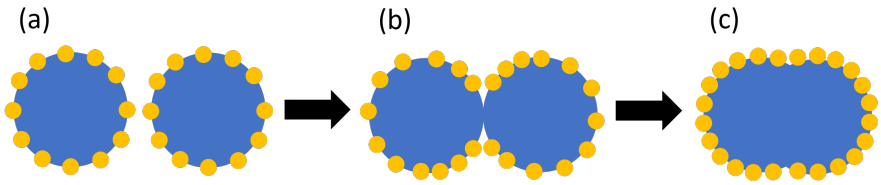

Figure 2.3 *(a) Droplets(blue) partially coated with solid particles(yellow). (b) Droplets come into contact and particles are displaced along the interface away from the contact region. (c) Droplets coalesce until the particles jam on the interface, producing a non-spherical droplet.*

and sedimentation are generally not preventable by particle-stabilisation alone unless the particle mass is carefully tuned such that the particle-stabilisation causes the droplets to be density matched with the continuous phase. Rather these can be prevented by adjusting the density of either of the liquid phases such that the two match. Finally droplet flocculation in particle-stabilised emulsions can be controlled by the choice of stabilising particles. It has been shown that in some cases, a low degree of flocculation in the stabilising colloids can prevent or reduce droplet flocculation [28] while increased particle flocculation can destabilise the emulsion via flocculation and coalescence [44]. Alternatively, adding steric interactions between the stabilising particles by grafting polymer hairs onto the particles also reduces or prevents droplet flocculation [45].

The stability and behaviour of the emulsion is highly dependent on the mechanical properties of the interface, specifically its response to stress [46]. The deformation of an interface can take two forms: dilatational, where the area is changed at constant shape; and shear, where the shape is changed at constant area [47]. The study of a material's response to deformation is rheology, or interfacial rheology when probing the properties of an interface. Using rheology, the presence of particles has been shown to affect the viscoelastic properties of a liquid-liquid interface [46], even causing particle-stabilised droplets to show solid-like behaviour under certain conditions [48]. Simulations and experiments have also shown the movement of particles around droplet interface under shear and their effects on the droplet deformation and breakup [49, 50]. This is dependent on the choice of particles and their arrangement at the interface, *e.g.* whether or not they aggregate on the interface and whether inter-particle interactions are present [51]. The mechanical properties of the interface then can affect the behaviour of emulsions from the point of formation via limited coalescence [52] to their

response to external stresses and the resultant collisions of droplets which may or may not cause partial coalescence to occur.

The importance of stability varies between applications. There are industries in which undesirable emulsions form, and the destabilisation of such emulsions is necessary. One example of this is the oil refinement industry, where water must be removed from the crude oil. Commonly, the water takes the form of droplets stabilised by particles, such as waxes, and/or surfactants, such as asphaltenes [53]. In order to refine the oil, these emulsions must be broken down via techniques such as solvent extraction, ultrasound and heating [4, 53–56].

It is, however, more common to retain or enhance emulsion stability because the emulsion structure is key to the function of the product. In particular, in the food industry stability is important as destabilising an emulsion can damage the product or reduce shelf life [57, 58]. Even if the damage is reversible, such as redispersing creamed droplets by mixing [20], the visual appeal of the product on the shelf is important from a consumer perspective, thus a separated emulsion, though recoverable, may not appeal to the consumer [59, 60].

In comparison to surfactant-stabilised emulsions, particle-stabilised emulsions can exhibit enhanced stability because particle-stabilised emulsions can be less susceptible to some destabilisation mechanisms such as Ostwald ripening and coalescence [41, 43]. Particle-stabilised emulsions have also been proposed as a route to reducing the usage of environmentally harmful surfactants as well as those which are regarded as irritants or provoke allergic reactions [61–63]

2.2 Freezing - its purpose and consequences

2.2.1 The necessity of freeze-thaw stability

Freezing is a process commonly used in a range of industries such as the food industry [64], pharmaceuticals [65] and construction [66]. In each case, control of the freezing and thawing processes is key either to control the product structure or, as in the case of construction, to allow other processes to be carried out successfully.

The food industry is of particular interest as Pickering emulsions have a number

of current applications in that field such as salad dressing, margarine and mayonnaise. There are also potential applications in encapsulation for controlled release and in fat replacement [19, 67]. Within the food industry, there are two main reasons for freezing products. Firstly, there are products such as ice cream [68] which are consumed while frozen, and thus the effects of the freezing process on the product longevity and taste, and therefore the structural integrity, must be understood. Secondly, freezing is a common method for increasing product shelf life by delaying the deterioration of foods due to bacterial growth and enzyme activity [69].

In the first case, crystal properties are important in their own right as they affect the texture and taste of products [70], but in both cases the growth of crystals is also important in the effects on the structure and stability of the product. Crystallisation in the continuous phase of an emulsion for example is likely to force emulsion droplets together, altering the emulsion structure [71]. Equally, recrystallisation, which is dependent primarily on storage conditions and the presence, or absence, of stabilisers, is also an important consideration because changes in crystal structure also affect the product [70]. As such, the conditions under which products are frozen are often carefully controlled in order to achieve the desired crystal growth rate or size [72].

When considering freezing for storage, the way in which a product thaws is also important as the product is ultimately used in its thawed state. For example, breakdown of internal structure may begin during freezing, but the structure may be (partially) preserved until thaw, at which time the structure collapses, *e.g.* an emulsion separates [73].

2.2.2 Freeze-thaw stability of emulsions

Having seen that Pickering emulsions are proposed as advantageous due to their enhanced stability and reduced allergenic risk, and that freezing products is an industrially relevant process which has potential to damage or alter product structure, it is useful to understand how the freezing process affects Pickering emulsions. There are a number of factors affecting the freeze-thaw stability of emulsions relating to the emulsion composition and to the freezing process. The material properties of the two liquid phases are important as factors such as the composition of the oil and its crystal formation process affect the freeze-thaw stability [74]. Equally, the presence and/or type of stabilisers in the system also

plays a role [7]. Concerning the freezing process, the order in which the phases freeze, the cooling rate and crystal growth rates as well as the freezer temperature may each play a role in the emulsion behaviour [5, 75].

The freeze-thaw behaviour of an emulsion can be affected by which of the two phases (continuous or droplet) freeze and the order in which they freeze. A freezing continuous phase is capable of pushing droplets together, and if the droplets are still liquid, there is the potential for the droplets to (partially) coalesce before freezing [57]. Additionally, if the droplet phase is water, then as water expands on freezing this can cause cracks to develop in the already frozen continuous phase. As smaller droplets can freeze more slowly than larger ones, smaller still-liquid droplets can fill cracks made by larger droplets, creating a network between the droplets and leading to coalescence on thaw [75]. Alternatively, for a system with an oil droplet phase, the droplets freezing first can also cause destabilisation as collisions between semi-crystalline droplets can allow any crystals protruding from one droplet to rupture the interface of the other, causing the droplets to coalesce [71, 76]. In some cases, the difference in the order of component freezing can mean the difference between a freeze-thaw stable emulsion and an unstable one [75].

In addition, the effects of freezing on pH and ionic strength or solute concentration within an emulsion may lead to emulsion destabilisation during the freeze-thaw cycle due to 'freeze-concentration'. This occurs when solutes from the continuous phase are excluded during freezing and migrate to unfrozen regions. It leads to regions of higher and lower solute concentration, changing the pH or ionic strength and thus changing the electrostatic interactions between charged droplets or the conformation of surfactants/proteins on the interface and increasing the probability of flocculation and thus destabilisation [57, 73].

In each of these cases, the nature of the emulsifier is important in determining whether emulsions destabilise during freeze-thaw cycling [77]. It has been shown for example, that protein-stabilised droplets are more stable to freeze-thaw cycling than (small-molecule) surfactant-stabilised droplets because proteins provide a thicker membrane around the droplet, particularly in the case of a multi-layered membrane, which enhances steric repulsions between the droplets to further prevent coalescence [7, 78, 79]. In the case of surfactant stabilisation, the choice of surfactant is important as some surfactants can change the crystallisation dynamics of fat droplets during freeze-thaw cycling and improve the freeze-thaw stability by preventing fat crystals from protruding out of one droplet and

penetrating another [80] while other combinations can cause dewetting of the liquid from the crystalline droplet leading to non-spherical solid fat droplets [81].

With Pickering stabilisation, some of these issues may be resolved as the particles may present a barrier both to the inner phase leaving a liquid droplet and to a semi-crystalline inner phase from making contact with other droplets [76, 82]. Existing studies have primarily considered two classes of stabilising particles: protein-based particles [7, 83, 84] and starch-based particles [5, 76, 82, 85] which have advantages as they are typically food-grade and so have the potential to be used in food applications. In many of these cases, high freeze-thaw stability has been observed, but this is dependent on the freezing conditions and there is debate over the optimal freezing conditions, whether fast or slow freezing is best for emulsion stability [5]. It may also be dependent on the order of component freezing. In some cases, the starch particles were observed to be forced off of the interface, increasing the probability of coalescence [5, 85]. In addition in some of these cases, the enhanced stability may be the result of particle gelation at the interface [5, 7].

To our knowledge there is little information about how the freeze-thaw process affects the emulsion microscopically, not just after the cycle but during both the freezing and thawing stages. In particular, there are limited studies on model systems in which particle gelation/crosslinking at the interface does not occur or in which other additional stabilisers such as polymers are not present [86]. Typically also the cooling rate is not systematically controlled but samples are placed directly into a freezer for a given length of time and it would be of interest to study more closely the effect of cooling rate because, as discussed earlier, it has an effect on the emulsion stability.

2.3 Crystal nucleation theory

In order to understand the effect of freezing on emulsions, the crystallisation process must be understood. There are four stages to the freezing process in a liquid: undercooling, crystal nucleation, crystal growth and recrystallisation [57]. Crystal nucleation and growth are the most difficult to achieve, primarily because of the energy barrier to crystal formation.

The liquid-solid transition is a first-order (discontinuous) phase transition,

meaning that the first derivative of the free energy is discontinous at the transition [87]. As shown in Fig. 2.4, above the melting temperature, it is more energetically favourable for the material to be in the liquid state as the Gibbs free energy is lower for the liquid than the solid. At the melting temperature, the bulk free energy is the same for both liquid and solid states. However, it still costs energy to form a crystal, therefore in a liquid free of impurities, crystallisation will not begin at the melting temperature. In order for crystal nucleation to begin, the liquid temperature must drop below the melting temperature, a phenomenon known as undercooling or supercooling.

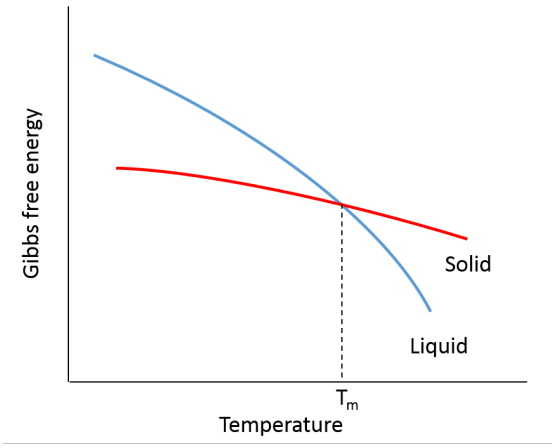

Figure 2.4 *Free energy as a function of temperature for a material in its solid and liquid phases. The melting temperature, T_m marks the crossover point of the two curves.*

There are two mechanisms by which crystal nucleation can occur - homogeneous and heterogeneous nucleation. Homogeneous nucleation is spontaneous, while heterogeneous is instigated by a favourable crystallisation surface within the liquid, such as a dust particle.

Homogeneous nucleation

In order to understand homoegeneous nucleation, the Classical Nucleation Theory is the most commonly used description [88]. Homogeneous nucleation is a spontaneous event driven by the free energy of the system and there is a balance to be struck between the favourability of the solid phase over the liquid and the unfavourability of creating a solid-liquid interface [88]. This is shown in Fig.

2.5. While the bulk free energy from the presence of the solid promotes crystal growth, the surface free energy from the solid creation promotes the remelting of the crystal.

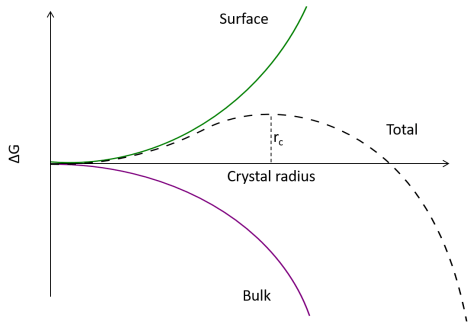

Figure 2.5 *Contributions to the change in free energy from the surface and bulk of a nucleating crystal with the dashed line showing the total free energy change as the sum of the two contributions.*

The total free energy change, ΔG, is the sum of these two free energy changes and, assuming a spherical crystal, is described by the equation [87]

$$\Delta G = \underbrace{\frac{4}{3}\pi r^3 \Delta G_\mathrm{b}}_{\text{bulk term}} + \underbrace{4\pi r^2 \gamma_\mathrm{sl}}_{\text{surface term}} \quad , \tag{2.12}$$

where r is the crystal radius and γ_sl the solid-liquid surface tension. ΔG_b is the change in bulk free energy per unit volume and is negative. It is proportional to the undercooling, ΔT and the latent heat, ΔH_m [87]. This curve passes through a maximum at a critical radius, r_c, and this denotes the turning point between crystal growth and crystal dissolution; below r_c the crystals are not stable as increasing their size increases the energy cost to the system, but above r_c, increasing the crystal size will lower the free energy, thus the crystals will grow.

The rate of crystallisation, J, is defined as

$$J = A \exp\left(-\frac{\Delta G^*}{k_\mathrm{B} T}\right) \quad , \tag{2.13}$$

where A is a prefactor relating to the number density of nucleation sites, the rate

at which molecules from the liquid attach to the nucleus and the probability that a nucleus at the critical size will form a stable crystal [89], T temperature and ΔG^* the height of the energy barrier at r_c (see Reference [90] for the detailed derivation of this equation). The exponential factor relates to the probability of a crystal nucleus forming at the top of the energy barrier at all and is dependent on both the critical free energy and the thermal energy of the system [89]. If the energy barrier to crystal nucleation is small in comparison to the thermal energy, the crystallisation rate will be high. The energy barrier is inversely proportional to ΔG_b and thus it is also inversely proportional to ΔT, meaning that increasing undercooling lowers the energy barrier and increases the crystallisation rate [87]. Therefore undercooling is advantageous to crystal nucleation and growth.

Heterogeneous nucleation

In general, the probability of homogeneous nucleation occurring is low, and crystallisation more often begins via heterogeneous nucleation. This is a mechanism which requires the presence of an impurity either on the surface of the vessel containing the fluid or within the fluid itself, such as a dust particle. Such an impurity provides an extra nucleation site upon which a crystal nucleus can form.

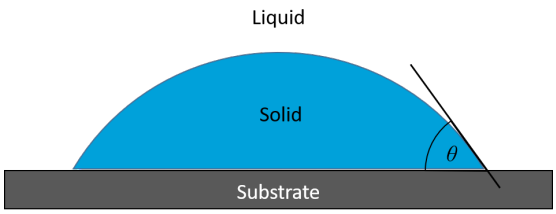

Figure 2.6 *Heterogeneous nucleation of a crystal (blue) on a surface (grey) modelled as a spherical cap with contact angle θ.*

If we consider the simple case of a crystal nucleus forming a spherical cap on a flat surface, as shown in Fig. 2.6, the free energy of the system can be described in a similar manner to that for homogeneous nucleation, but there are now three surface contributions rather than one: the nucleus-substrate (ns), nucleus-liquid (nl) and liquid-substrate (ls) interfaces, each characterised by its own interfacial tension. The interfacial tensions can be related via the contact angle, θ, as follows

$$\gamma_{\mathrm{nl}} \cos\theta = \gamma_{\mathrm{ns}} - \gamma_{\mathrm{ls}} \ . \tag{2.14}$$

When these contributions are added into the free energy, it can be shown that the free energy barrier, $\Delta G^*_{\mathrm{hetero}}$ can be expressed in terms of the homogeneous free energy barrier as [89, 91]

$$\Delta G^*_{\mathrm{hetero}} = \Delta G^*_{\mathrm{homo}} f(\theta) \ , \tag{2.15}$$

where $f(\theta)$ is given by the expression

$$f(\theta) = \frac{1}{4}\left(2 - 3\cos\theta + \cos^3\theta\right) \ . \tag{2.16}$$

This function is contact-angle dependent, and thus the barrier to nucleation is lowered for $\theta < 90°$. This means that a lower degree of undercooling is required in order to activate heterogeneous nucleation [87].

Chapter 3

Experimental Methods

This chapter details the materials and experimental techniques relevant to multiple results chapters; techniques used only in one chapter are detailed in the relevant chapter.

3.1 Particles

3.1.1 DiIC-labelled poly(methyl methacrylate) particles

Poly(methyl methacrylate) (PMMA) particles are the primary colloidal particles used throughout this thesis. They were synthesized within the University of Edinburgh by Dr. Andrew Schofield according to the procedure described in Reference 92. Particles were labelled with the fluorescent dye DiIC-18 and stabilised by poly(12-hydroxystearic acid) (PHSA).

Particles were sized using transmission electron microscopy (TEM) and one of the images obtained is included in Fig. 3.1. To size particles, images were loaded into ImageJ [93] and then thresholded appropriately to leave the particles in black against a white background. In order to separate any touching particles, a 'watershed' was applied to the image, and then the particle areas were measured using 'analyze particles'. From this, the radius of the particles was determined on the assumption that the particles were spherical.

In order to determine the particle size distribution, particles were sorted by radius

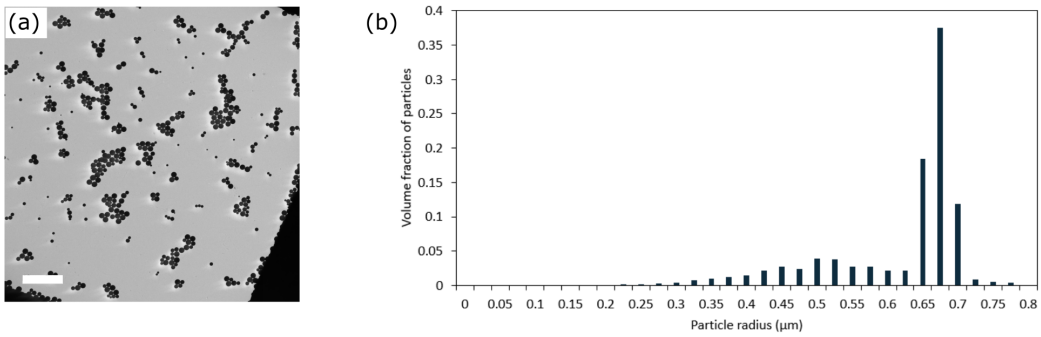

Figure 3.1 *(a)TEM image of the PMMA particles used to stabilise emulsions. Scale bar: 10 μm. (b) Size distribution of particles as measured from TEM images. This distribution shows a sharp peak at 675 - 700 nm and a lower, broader peak around 500 nm, indicating the polydispersity*

into bins 25 nm in size and the fraction of the total number of particles per bin was then plotted against radius. This plot is shown in Fig. 3.1(b). From this plot, we see a sharp peak around 675-700 nm and we also see a lower, broader peak around 500 nm, meaning that we have a non-monomodal particle dispersion.

We attribute the polydispersity to the DiIC-18 dye used to label the particles. This particular dye was required as it fulfilled two criteria: it covalently bonded with the particles, meaning that it will not leak out of the particles, as physically absorbed dyes can do, and act as a surfactant [94]; in addition, it is excited with the 555nm laser, allowing us to use Nile red to fluorescently dye the oil and excite with the 488nm laser, thus enabling us to see the three components in our emulsions simultaneously but distinguishably.

Although these particles are non-monomodal, we obtained similar results in experiments using emulsions stabilised by monomodal, NBD-dyed particles. In addition, other particles commonly used in model systems, such as fumed silica, can be polydisperse either due to processing [95, 96] or to flocculation [97, 98]. In considering the application of Pickering emulsions to food products, polydispersity is also not unrealistic as many food-grade particles are also polydisperse, some due to aggregation of primary particles such as starch granules [99–101].

3.1.2 NBD-labelled PMMA particles

In some experiments, NBD-dyed PMMA particles were used. These were synthesized within the University of Edinburgh by Dr. Andrew Schofield according to the procedure described in Reference 102. Particles were stabilised by poly(12-hydroxystearic acid) (PHSA) and labelled with 4-chloro-7-nitrobenzo-2-oxa-1,3-diazol (NBD) which was chemically linked to the particles. The particle radius was determined via TEM to be 477 nm with a polydispersity of 8%.

3.2 Hexadecane

The oil used in the majority of emulsions was *n*-hexadecane. To ensure the oil was free of surfactants which could affect emulsion behaviour,*n*-Hexadecane (ReagentPlus 99%, Sigma-Aldrich) was filtered twice through aluminium oxide (activated, basic, Fluka). Nile red (technical grade, Sigma Aldrich) was dissolved into the oil at a maximum concentration of 0.7 mM in order to image the oil phase via fluorescence microscopy.

3.2.1 Pendant drop tensiometry

Pendant drop tensiometry was used to determine the surface tension of undyed, filtered hexadecane in order to ensure the cleaning process removed impurities in the oil sufficiently that the measured bare air-oil interfacial tension was close to the literature value. A Krüss EasyDrop tensiometer (model 65 FM40Mk2)was used and a syringe with a steel needle used to produce a drop of oil with volume in the region of 13-15 μl - as large as possible before the droplet drops off the needle. The Krüss shape analysis software was used to take images of the droplet shape and then given that shape to calculate the interfacial tension. The average measured interfacial tension over 3 droplets was 26.89(3) mN/m. Compared with the literature value of 27.05 mN/m [26], this suggests that the cleaning process is sufficient in removing surfactants from the hexadecane that it can then be used for making emulsion samples.

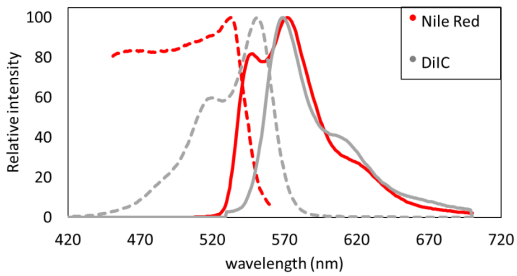

Figure 3.2 *Excitation/emission spectra for Nile red in hexadecane (red) and DiI (grey). Dashed lines show excitation, solid lines emission. Nile red data was measured as described in the text, DiI data taken from ThermoFisher Spectraviewer [105]*

.

3.2.2 Fluorimetry

The fluorescence excitation and emission spectra of Nile red in hexadecane were probed using fluorimetry as Nile red is known to be a solvatochromic dye, meaning that its absorption and emission spectra shift depending on the polarity of the solvent in which it is dissolved [103, 104]. A Cary Eclipse fluorescence spectrometer was used to determine the excitation and emission spectra of Nile red-dyed hexadecane. First undyed hexadecane was loaded into the glass sample cell, placed into the spectrometer and then the machine calibrated. Then Nile red-dyed hexadecane was loaded into the same sample cell and measurements taken. First a sweep of the emission wavelengths at a fixed excitation wavelength was carried out, and then vice versa. Given that Nile red fluorescence was detected in confocal microscopy when using a 488nm excitation laser beam, this wavelength was chosen as the excitation wavelength for the emission sweep. The peak of the emission curve was then taken as the emission wavelength for the excitation sweep.

The measured excitation/emission spectra for Nile red in hexadecane are included in Fig. 3.2(b) (red curves). It can be seen that there is a broad region of high relative intensity in the excitation curve with a peak around 525 nm before a sharp drop-off at longer wavelengths. The emission spectrum has two peaks, one just below 550 nm and the other around 575 nm.

The spectra for the DiIC-18 dye (grey curves), which are taken from Reference 105, are also included in the same plot. Although there is much overlap between the Nile red and the DiIC, particularly with the emission spectra, provided that

the excitation lasers and emission filters on the confocal microscope are used correctly, little crossover is observed. Only when the Nile red signal is weak do we observe any signal from the particles in the oil channel.

3.3 Pickering emulsion preparation

In order to make the emulsions, PMMA particles were transferred from decalin, in which they were initially stored, into *n*-hexadecane. This is a two-stage process via tranfer first into hexane as follows. PMMA particles were transferred from decalin into *n*-hexane (97%, Fisher Scientific) through centrifugation, to force the particles to the bottom of the vial, supernatant removal and replacement with *n*-hexane (97%, Fisher Scientific) and then particle redispersal. Both sonication (VWR ultrasonic bath, 80 W, 45 kHz) and vortex mixing (Fisons WhirlMixer) were used to ensure no particle aggregates remained. After five repetitions of this process, the particles were transferred from *n*-hexane into *n*-hexadecane following the same protocol.

Distilled water was deionized using a Milli-Q (MilliPore) filtration system (to a resisitivity of at least 18 MΩ·cm). The oil was then fluorescently labelled with Nile red and undissolved Nile red was then removed by filtration once through filter paper. The maximum concentration of Nile red was 0.7 mM. As the Nile red is diluted with undyed oil during emulsion preparation, the emulsions will contain lower concentrations of dye.

Water-in-hexadecane emulsions were then made according to the following protocol. The particle dispersion was placed into the sonic bath for 30 minutes and then vortex-mixed for 10 s. After this the dispersion was returned to the sonic bath for at least another 15 minutes followed by 10 s vortex mixing and this was repeated until the particles were fully redispersed with no aggregates visible by eye. Nile red-dyed hexadecane was then added to the particle dispersion, with the volumes of the two varying according to the desired emulsion droplet size. The ratios for each droplet size are given in Table 3.1 and in each case, the mass of oil + particles remained constant at 2.449 g. The mixture was then returned to the sonic bath for 15 minutes, followed by 15 s of vortex mixing. Deionized water was added, the same mass for each sample (2.0 g) and the samples were then emulsified via 60 s of vortex mixing, followed by 5 minutes standing time, repeated 3 times to ensure emulsification was complete and the excess oil supernatant was

Predicted droplet size (μm)	mass of oil (g)	mass of particles (g)
25	1.854	0.595
50	2.151	0.298
75	2.251	0.198
100	2.300	0.149
125	2.330	0.119

Table 3.1 *Emulsion composition for each predicted average droplet size. The mass of water added was the same in each emulsion with a value of 2.0 g*

clear *i.e.* all particles have reached a droplet interface. The emulsion droplet diameter was controlled by the mass of particles added to the oil as described in Chapter 2.

3.3.1 Sample cell preparation

Rectangular, glass sample cells (5 mm internal path length, 1.56 ml volume, Starna Scientific Ltd) were coated with PHSA stabilising hairs to prevent the particle-coated droplets from sticking to the glass. This was achieved by soaking the sample cells overnight in a solution of PHSA-Si in tetrahydrofuran (THF) and then rinsing with hexane and toluene. PHSA-Si is a comb stabilizer of PHSA chains attached to a PMMA backbone containg 5% trimethoxysilyl propyl methacrylate and the PHSA-Si in THF solution was made in-house. Cells were filled using an Eppendorf pipette with the end of the plastic tip cut off to increase the tip diameter and lower the risk of damaging emulsion droplets during cell filling. A volume of 300 μl of emulsion was decanted into the cell, lower than the total cell volume, so that the emulsion did not touch the glass lid, preventing structural changes due to capillary forces when putting the lid on to prevent evaporation and associated flows.

3.4 Microscopy

3.4.1 Confocal microscopy

Principles of confocal microscopy

Confocal laser scanning microscopy (CLSM) is a technique commonly used for imaging fluorescently labelled samples. The primary advantage confocal microscopy has over standard microscopy is the rejection of out of focus light by a pinhole in front of the detector. A schematic of a confocal microscope is shown in Fig. 3.3. A coherent beam of laser light is used to excite the fluorescence at a single point in a sample, causing the sample to emit light at a different frequency to the excitation beam. This light is then collected by the detector, typically a photomultiplier tube (PMT). Before that, the light must pass through a pinhole. The pinhole is positioned such that only light emitted from the focal plane passes to the detector, while light from elsewhere is blocked. This configuration leads to improved axial resolution, thus improving image quality [106].

In order to build up an image of the sample, scanning mirrors are used to image a series of points line-by-line in the xy plane. Given the improved axial resolution, using confocal microscopy also allows for optical sectioning, thus also for 3D imaging which is useful for understanding sample structure, particularly when a sample structure is not uniform.

By using multiple lasers with separate PMT detectors, it is possible to excite the fluorescence of multiple fluorophores within a single sample, thus imaging several components simultaneously. This is typically achieved by using appropriate filters just in front of the PMT detectors, though prisms can be used instead for greater flexibility, to ensure there is minimal crossover of signal. When raster scanning, the lasers each scan line-by line, with one laser following the other such that both images build up almost simultaneously.

Confocal imaging methods

Samples were observed using a confocal laser scanning microscope (Zeiss LSM 700) coupled to a Zeiss Observer Z1 with an LD Plan Neofluar 20 $\times$/0.4 Korr objective. The 488 nm laser line was used to excite the Nile red in hexadecane

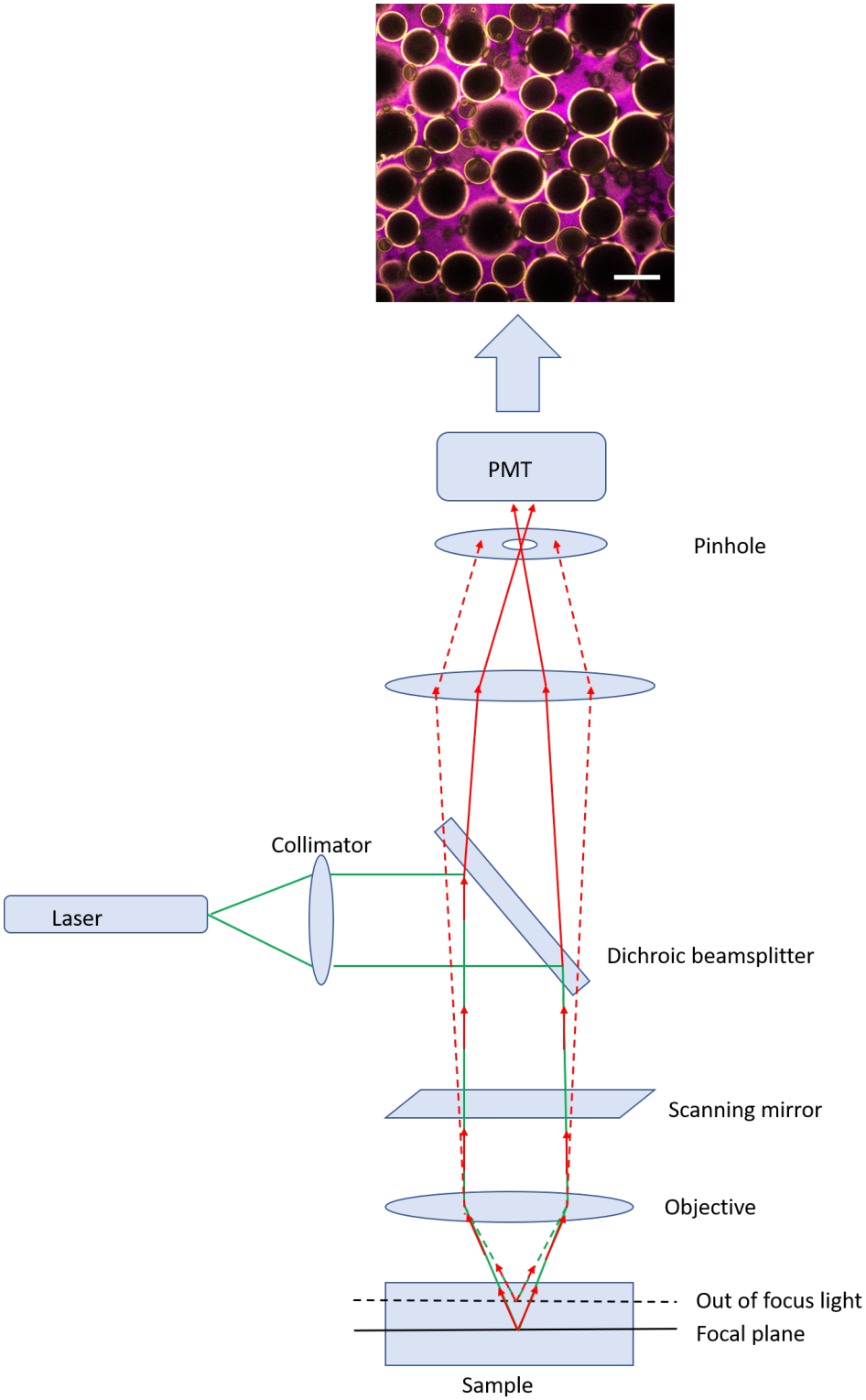

Figure 3.3 *Schematic showing the light path through the components of a confocal microscope. Green lines show the excitation beam while red lines the emitted light. Solid red lines show the emitted light from the focal plane as it passes through the pinhole to reach the detector while out-of-focus light, represented by the dashed red line, is blocked by the pinhole. A typical image of a particle(yellow)-stabilised water(black)-in-oil(magenta) emulsion sample obtained from the confocal microscope is shown at the top of the schematic.*

and the 555 nm line to excite DiIC-18 in PMMA particles. Emission filters were used as appropriate and samples were observed in fluorescence and transmission. A typical confocal image of a particle-stabilised emulsion sample is shown in Fig. 3.3. The PMMA particles are coloured yellow, the oil magenta and the water in black. This colour scheme will be used throughout this thesis unless specified otherwise.

It should also be noted that the fluorescence of Nile red is lost as the hexadecane freezes, thus the magenta becomes black on freezing. This may be due to a shift of the fluorescence spectrum as a change in colour is observed by eye upon freezing in the sample cells and also in a 4ml vial of Nile red-labelled oil placed in the fridge. It may also be due either to scattering of the emitted light by the crystals or to the rejection of dye from the oil crystals [107].

3.4.2 Multiphoton excitation microscopy

Although confocal fluorescence microscopy has many advantages over conventional optical microscopy, it doesn't easily allow imaging deep into a sample where the components are not refractive index matched and without using high laser intensities which can cause photobleaching [108]. For experiments in which higher imaging depth is important, such as biological tissue imaging, multiphoton microscopy is a better choice of microscope as the alternative method of fluorescence excitation can allow imaging over hundreds of microns in depth.

In single photon excitation a single photon is absorbed by a fluorescent molecule in its ground state, causing an electron to be raised to an excited state. The decay of this electron then leads to photon emission at a different wavelength to the excitation photon as shown in Fig. 3.4(a). In two-photon excitation (2PE), two lower energy, longer wavelength photons are absorbed almost together. The first excites the electron to an intermediate state, then the second excites the electron to the excited state, as shown in Fig. 3.4. Fluorescence emission then occurs in the same manner as single photon excitation. In this way, the lower energy photons are less damaging to the sample, hence this technique is also useful for biological samples. More importantly, the longer wavelength photons are less likely to be absorbed or scattered by the sample, thus the imaging depth is better than for confocal microscopy [109, 110].

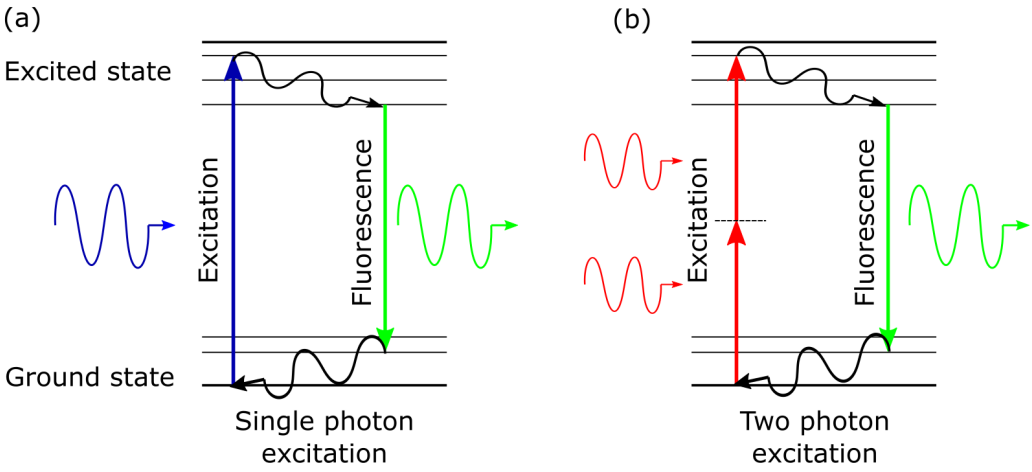

Figure 3.4 *Jablonski diagrams showing (a) single photon excitation and (b) two-photon excitation.*

3.5 Temperature control

3.5.1 Instec temperature stage

To allow temperature control of the samples during confocal imaging, a temperature stage (Instec TSA02i with mk1000 temperature controller) was used, shown in Fig. 3.5(a). The stage temperature was both recorded and controlled using the temperature controller software (WinTemp for mk1000). The stage was cooled by pumping iced water through two peltier cooling elements which control the sample chamber temperature.

Emulsion samples were studied under two stage configurations, shown in Fig. 3.5; the first is considered 'non-uniform' cooling, and the second 'uniform cooling'. Temperature gradients were observed inside the temperature stage during test experiments and this translates into a temperature gradient within the sample when the sample is left open in the stage, as shown in panel (a). To reduce the effects of these gradients, the sample is placed inside an aluminium casing such that, apart from a small portion at one end, the whole sample is enclosed. In addition, the sample is rotated 90° compared to the non-uniform configuration so that the long axis of the sample cell is perpendicular to the direction of the temperature gradient, thus the direction of greatest temperature gradient

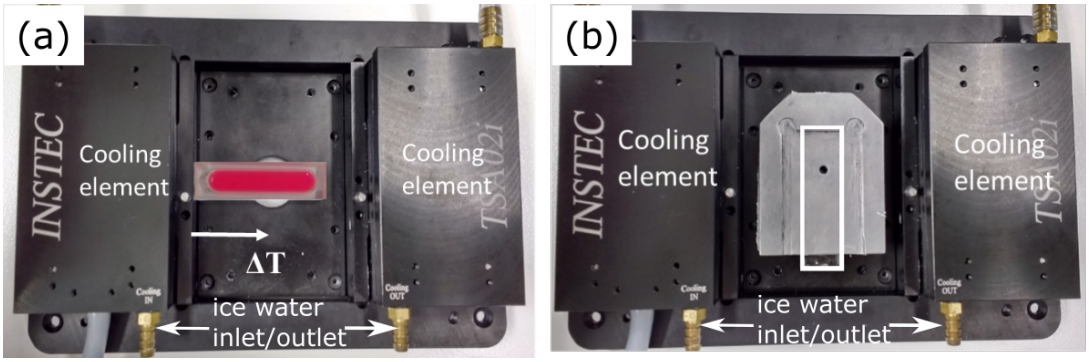

Figure 3.5 *Temperature stage with sample configurations for (a) non-uniform and (b) uniform cooling.*

is aligned with the shorter sample cell axis, reducing the effect on the sample. The nature of the temperature gradients observed are discussed in more detail in Chapter 4.

Non-uniform freezing

In the case of non-uniform freezing the sample was positioned such that one end of the sample cell was in contact with one of the cooling elements while further along, the sample cell was situated about 0.5 mm above the viewing window which acted as a heat source, the ambient temperature being higher than the stage temperature. This is shown in Fig. 3.5 (a). In this way, the temperature at a given time varied with position along the sample length.

Uniform freezing

In the case of uniform freezing, the sample cell was placed into a metal casing sealed with silicone thermal grease (RS heat sink compound plus) such that only a small part of the sample cell was not enclosed, as shown in Fig. 7.1 (b). This reduced the effect on the sample of the temperature gradient in the stage arising from the positioning of the cooling elements and the presence of the lower and upper glass viewing windows.

Freezing samples

Before placing samples into the stage, the stage temperature was set to 20 °C and allowed to equilibrate. Samples were then placed into the stage in one of the two configurations shown in Fig. 3.5. As the melting temperature of hexadecane is higher than water, lying between 18.1 to 18.2 °C [26, 111, 112], reducing the stage temperature to 10 °C was sufficient to freeze the oil in the samples, while the water remained above its melting temperature throughout. The cooling rates used were in the range 0.5 °C/min to 8 °C/min. In order to ensure the oil in the samples was completely frozen, the stage temperature was held at 10 °C for 20 to 25 minutes in each freeze-thaw cycle. Following this, the stage temperature was raised back to 20 °C at the same rate used in the freezing phase in order to thaw the samples.

3.6 Interfacial rheology

Interfacial rheology experiments were carried out with the aim of understanding the behaviour of the particles used in emulsions at a flat water-oil interface. However, the results of those experiments yielded little information about the behaviour of the system due to the dominance of the instrument response over the interface behaviour. The results do provide useful technical information and have thus been included in Appendix B. The materials and methods used are contained within that appendix and are therefore omitted here.

Chapter 4

Thermal profile and crystallisation of freezing hexadecane in simulation and experiment

4.1 Introduction

When considering the freeze-thaw stability of emulsions, it is important to consider the conditions under which emulsions are frozen as this can affect how the emulsion structure is altered during the process [5]. For example, an emulsion can be placed into a freezer at a fixed temperature and then thawed at room temperature or above [4, 113, 114]. In this case, the freezer temperature and the cooling rate, set by the freezer/sample temperatures and the sample material properties [115], can affect the emulsion stability to freeze-thaw cycles [5]. Any non-uniformity in sample temperature could lead to one part of the sample freezing before another - a vital condition for directional freezing [116] which will be discussed in detail in Chapter 6. This can result in the structure of the sample changing in a different manner to the case where the temperature is the same throughout the sample at any given moment in time [117, 118].

In addition, understanding the crystal growth kinetics within the sample is useful as varying the crystallite structure can affect the product structure, a fact well known in the production of food products such as ice cream [119]. By using a freezer, these factors cannot easily be directly probed, only the end result

can be observed. Thus it is useful to observe the freezing process in real time while controlling parameters such as the cooling rate as this can provide an understanding of how the experimental conditions affect the sample behaviour. Before considering the behaviour of emulsions, characterising the experimental setup with oil alone is important in allowing features in emulsion behaviour which result from the experimental setup to be distinguished from those which result from the presence of emulsion droplets. Characterisation can be achieved using a combination of simulations and experiments.

Experimentally, the temperature profile of a whole sample is not always easily measured, particularly when the sample is small and enclosed within a temperature stage. Measuring with thermocouples is achievable, but this at most records the temperature at a few select points. In addition, these kinds of measurements are invasive, potentially providing extra crystal nucleation sites which could disrupt or mask the undisturbed sample behaviour. Given these experimental challenges, simulations are employed to provide an understanding of the temperature profile. COMSOL Multiphysics [120] is the finite-element analysis software used in this thesis. A model of the experimental setup can be drawn up with the appropriate material properties and experimental conditions (*e.g.* cooling rate) allowing the study of the thermal and fluid flow profiles within the experimental setup under the same conditions used in experiments.

Although simulations provide information about the temperature profile, the crystallisation kinetics of a sample are more easily understood via experimental observation. In a range of applications, the crystal growth requires careful control in order to produce the desired product structure and texture [72]. This means that the experimental setup can be an important factor in determining the shape, direction and speed of crystal growth [121]. For example, rapid cooling to temperatures far below the material's freezing temperature can produce smaller crystals which cause less structural damage than the larger crystals produced by slower cooling [57]. In this case, experiments are used to make the connection between temperature profile and crystal growth.

In this chapter, the main aim is to understand the effects of the experimental setup used to freeze samples on the temperature profile throughout the sample and on the crystal growth behaviour. Simulations and experiments are used on samples containing oil alone in order to distinguish between the effects of experimental conditions and the presence of droplets.

COMSOL simulations are used to model the experimental setup under typical experimental conditions in order to understand the heat propagation and fluid flow inside the sample. Uniform and non-uniform cooling configurations (as discussed in Chapter 3) are compared and the effect of adding droplets into the system is discussed as a representation of droplets in a (dilute) emulsion.

In experiments, oil samples are subjected to uniform and non-uniform freeze-thaw cycles at varying cooling rates. Temperature profiles for both configurations are recorded and the results discussed in light of the simulation results. Confocal microscopy and image analysis are employed to elucidate quantitative differences in crystallisation between uniform and non-uniform configurations. In addition, the effects of cooling rate on crystal growth are explored. Conclusions about the overall sample behaviour are drawn by considering both simulation and experimental results.

4.2 Simulation Methods

4.2.1 Geometries

To model the experimental setup in COMSOL, the relevant components were measured using vernier calipers and the model was drawn according to those dimensions. The appropriate materials were then assigned to each component of the model. Aside from hexadecane, all other materials were predefined within COMSOL and used as provided. Hexadecane was not predefined, so it was defined using the material properties given in References 122–126. For temperature-varying properties, either piecewise functions or interpolations were used depending on the data available. Where necessary, material properties of solid hexadecane were used for temperatures below 18 °C, the freezing temperature of hexadecane. Both the uniform and non-uniform setups described in Chapter 3 were modelled in the software, and the geometries are shown in Fig. 4.1 with components colour-coded by material. In both cases, the geometry is halved along the symmetry axis to allow for shorter simulation times, but at least one simulation per model was tested with the full model to ensure the symmetry did not affect the results.

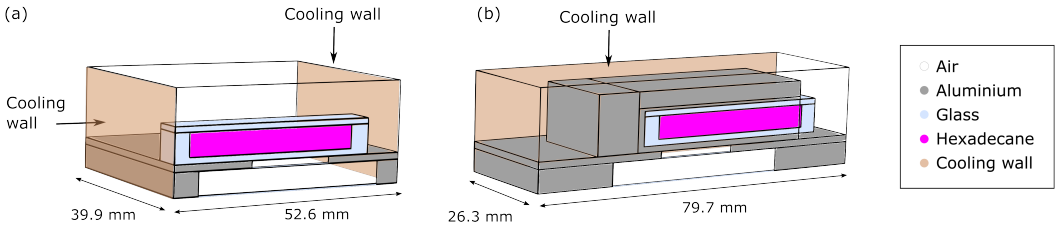

Figure 4.1 *(a) Non-uniform and (b) uniform geometries modelled in COMSOL. Both geometries are halved down the symmetry axis. Components are colour coded by material according to the key on the right hand side. Outer non-cooling walls are defined as insulating to represent the presence of the rest of the stage not modelled explicitly here.*

4.2.2 Physics

The two physics modules used here are heat transfer and fluid flow. The phase change is not modelled explicitly here, the reasons for which will be discussed in Section 4.2.4. Note that in this chapter, temperatures and cooling rates are reported in Kelvin to be consistent with the COMSOL software.

Heat transfer

The temperature change in the experimental system is achieved by cooling the peltier elements of the temperature stage. This is modelled by applying a fixed cooling rate to the appropriate wall(s) of the model, coloured in orange in Fig. 4.1. It is implemented by applying a piecewise function

$$\begin{cases} 293.15 - \frac{r}{60}t & \text{for } 0 \leq t \leq \frac{600}{r} \\ 283.15 & \text{for } \frac{600}{r} \leq t \leq 1000 \end{cases} \tag{4.1}$$

where t is time from the start of the simulation and r the cooling rate in K/min. The sample cools until the wall temperature reaches 283.15 K (10 °C) and then remains fixed. This mimics the experimental setup where the software is set to lower the stage temperature to 10 °C and then hold the stage at that temperature. This is far enough below the oil freezing temperature to ensure all the oil is frozen.

All other external walls are set to be insulating apart from the bottom glass

window which has a convective heat flux applied on the underside, meaning it allows heat from outside the stage, where the temperature is fixed at 298.15K, to transfer through the glass into the stage, as experienced in experiments.

In order to solve the heat transfer, COMSOL employs two equations, one for solids and one for liquids. The equation for solids is presented in Equation 4.2 and the equation for liquids is presented in Equation 4.3:

$$\rho C_p \left(\frac{\partial T}{\partial t} + \boldsymbol{u}_{\text{trans}} \cdot \nabla T \right) + \nabla \cdot (\boldsymbol{q} + \boldsymbol{q}_r) = -\alpha_p T : \frac{dS}{dt} + \mathcal{Q} \ . \tag{4.2}$$

$$\rho C_p \left(\frac{\partial T}{\partial t} + \boldsymbol{u} \cdot \nabla T \right) + \nabla \cdot (\boldsymbol{q} + \boldsymbol{q}_r) = \alpha_p T \left(\frac{\partial p}{\partial t} + \boldsymbol{u} \cdot \nabla p \right) + \tau : \nabla \boldsymbol{u} + \mathcal{Q} \ . \tag{4.3}$$

The two equations are functions of temperature, T and pressure, p and the other quantities are: density, ρ; specific heat capacity at constant pressure, C_{p}; velocity vector, $\mathbf{u}$; velocity vector of translational motion,$\boldsymbol{u}_{\text{trans}}$; heat flux by conduction, $\mathbf{q}$; heat flux by radiation,$\boldsymbol{q}_r$; coefficient of thermal expansion, α_P; viscous stress tensor, τ; the second Piola-Kirchhoff stress tensor, S and heat sources other than dissipation, $\mathcal{Q}$.

Laminar flow

For the air and hexadecane regions, laminar flow is applied with non-slip boundary conditions at the walls and zero initial velocity. For simulation convenience, a pressure point constraint is also applied to one top corner of the fluid inside the sample cell such that only hydrostatic pressure is experienced there. Gravity is also accounted for. The flow is coupled with the heat transfer to allow nonisothermal flow in all fluid regions, meaning that flow in the fluid is driven by the changing temperature. In order to achieve this, the fully compressible forms of the continuity and momentum equations are used as shown in Equations 4.4 and 4.5.

$$\frac{\partial \rho}{\partial t} + \nabla \cdot (\rho \boldsymbol{u}) = 0 \tag{4.4}$$

$$\rho\frac{\partial \boldsymbol{u}}{\partial t} + \rho\boldsymbol{u}\cdot\nabla\boldsymbol{u} = -\nabla p + \nabla\cdot\tau + \boldsymbol{F} \tag{4.5}$$

where **F** is the body force vector and other quantities are defined as for the heat transfer equations. Solving these equations includes solving the heat transfer equation for fluids but the heat transfer in solids remains separate as there is no flow to affect the heat transfer.

Mesh

A mesh is applied to the system in order to solve the system via finite element analysis. This was typically chosen as either the 'normal' or 'coarse' mesh and was determined by COMSOL according to the physics and geometry of the system such that edges and smaller components were divided using a finer mesh than larger central regions.

4.2.3 Model with droplets

In both uniform and non-uniform configurations, water droplets were added 1.25 mm from the symmetry wall at relative positions shown in Fig. 4.2. The set of 3 droplets are spaced 0.7 mm and 0.6 mm between centres and the pair of droplets spaced 2 mm apart. In order for droplets to be larger than the normal mesh size, the droplet size was increased from the typical experimental diameter of 20 - 100 μm to 0.5 mm. The single droplet simulates how a droplet in a dilute emulsion may behave, where there is no effect from neighbouring droplets. Two droplets close but not touching leaves space for oil to flow between the droplets, and the three almost touching droplets show the cumulative effect which may be observed in a more dense emulsion where the oil is forced around the droplets.

4.2.4 Simplifications applied to the model

In these simulations, several assumptions/simplifications are made compared to the experimental system in order to make the simulations feasible. The most significant simplification is that the phase change behaviour of the samples is not included in the model due to challenges with simulating this in COMSOL. Instead, at the freezing temperature (291K) the hexadecane material properties

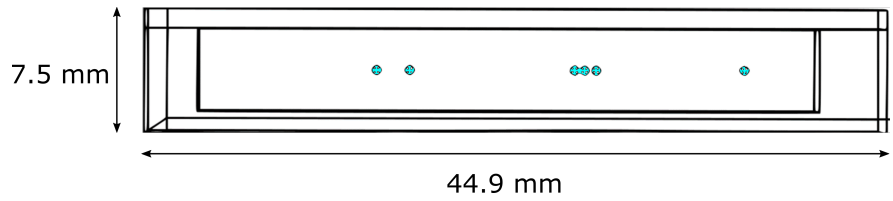

Figure 4.2 *Position of droplets in cuvettes in COMSOL. Droplets marked in blue.*

Material property	Liquid values	Solid values
Density	$f(T)$ (equation)	ρ (solid)
Dynamic viscosity	$f(T)$ (interpolation)	$f(T)$ (extrapolated)
Heat capacity at constant pressure	$f(T)$ (equation)	C_{P}(solid)
Speed of sound	$f(T)$ (interpolation)	c_{s}(solid)

Table 4.1 *Material properties required for the simulations. Each property is defined either by a fixed value, denoted by the appropriate symbol, or by some function of temperature, denoted $f(T)$. Functions are defined either by an equation or an interpolation between known values as denoted in the second and third columns of the table. References for each are given in the text.*

switch to those of solid hexadecane but the material is still defined as a 'liquid' in COMSOL, meaning that it can still flow. The material properties and the function types used to represent them are included in Table 4.1. Density, heat capacity and the speed of sound remain constant below the freezing temperature, while for dynamic viscosity, the function was extrapolated as the available data covered only temperatures above the maximum temperature applied in the simulation. As such, viscosity does not become infinite once the hexadecane goes below its freezing temperature as it would do if the hexadecane became solid. This means that the simulated sample will not show the temporary, constant temperature signature observed during a phase change as latent heat is released, rather the temperature in the sample should decrease as expected for a fluid. Our simulation results are therefore only reliable for temperatures above the oil freezing temperature.

In simulations, the whole sample is filled with hexadecane whereas in experiments the sample cell was only partially filled to prevent capillary effects. In addition fluid flow is modelled as laminar only so any turbulence would not be captured.

In modelling the temperature stage, the stage lid is not modelled explicitly, rather insulating walls on the 'air' in the stage are used to simulate this lid. In the uniform case, the viewing hole in the aluminium casing is not modelled, the main effect of which would be to cause a slight disturbance to the fluid flow and/or temperature profile in that region.

Finally, in addition to the increased size, droplets introduced into the system are stationary and do not move or deform under continuous phase fluid flow, as could be expected experimentally. The particle-stabilisation of the droplets used in experiments is neglected as this would require a very fine mesh, vastly increasing computing time. As the droplets in the simulation neither move, deform nor coalesce in these simulations, the effect of adding the particles into the simulation is expected to be limited. Only a limited number of droplets is considered as simulating many droplets requires the co-ordinates of each droplet to be manually entered and the extra droplets would have significantly increased simulation time.

4.3 Experimental Methods

4.3.1 Freezing oil with confocal microscopy

Sample cells were filled with 450 μl of nile red-dyed hexadecane prepared as described in Chapter 3. All experiments were carried out in the temperature stage in the uniform and non-uniform configurations introduced in Chapter 3 and included again for convenience in Fig. 4.3.

4.3.2 Temperature measurements

Undyed hexadecane was used here as no imaging was carried out during these measurements. Two thermocouples (RS Pro K-type) were used in each experiment, placed at positions marked (i) and (ii) in Fig. 4.3. Thermocouples were connected to a computer-controlled data logger (Pico TC-08) and temperatures recorded every second.

In order to correct for systematic errors due to thermocouple/data logger port difference, sample temperatures were recorded for a period of time at constant stage temperature until equilibrium in sample temperature was reached.

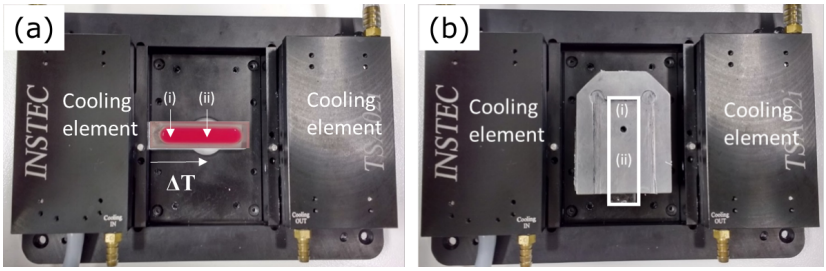

Figure 4.3 *(a) Temperature stage configuration for non-uniform freezing. One end of the sample cell (i) is in contact with a cooling element, while the sample cell is situated about 0.5 mm above the viewing window at (ii). (b) Temperature stage configuration for uniform freezing. The sample cell position is marked with a white outline. In both (a) and (b), points (i) and (ii) mark the positions of the thermocouples when taking temperature measurements.*

The average difference in temperature between (i) and (ii) at equilibrium was subtracted from all temperature values at point (i) so that at equilibrium the recorded temperatures at (i) and (ii) were the same.

4.3.3 Image analysis

Fluorescent channel analysis

Analysing crystal behaviour from the fluorescent channel was possible due to the loss of fluorescent intensity of the oil upon crystallisation. By importing image stacks into ImageJ [93] and extracting the fluorescent channel, the 'mean gray value,'$\langle I \rangle$, for each slice could be recorded in a spreadsheet (Microsoft Excel). The values were normalised against the first image value, I_0, in which no crystals were present. This accounts for differences in fluorescent intensity between runs and any uneven background illumination. Mean gray values were converted into crystalline fraction by subtracting the normalised values from 1. This means that a value of 1 for $(1 - (\langle I \rangle / I_0))$ denotes a fully crystalline image and a value of 0 indicates that the sample is fully liquid.

Transmission channel analysis

Image stacks were loaded into ImageJ and the transmission channel extracted. The 'subtract background' was used with a suitable rolling ball radius in order

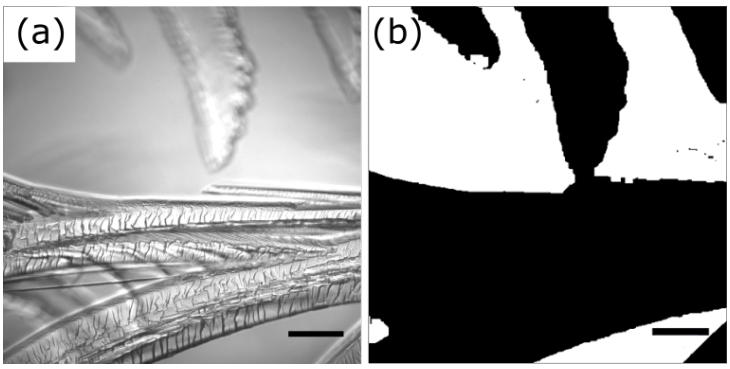

Figure 4.4 *(a) Hexadecane crystallisation as observed in the transmission channel. Both in-plane and out of focus crystals are visible. (b) Post-processing, binarised image of the picture in (a). Crystals appear in black and liquid oil in white. See text for details of image processing. Scale bars: 100 μm*

to reduce the effects of uneven background illumination. A threshold was then applied to produce a binary image with the crystalline areas appearing black and liquid regions white. To fill in crystalline areas not captured by the threshold, the 'despeckle', 'close' and 'fill holes' tools are used. The white border introduced into images by these processes was removed by cropping the canvas by 2 pixels on each side. Each image is then compared to the original transmission image and the pencil or bucket fill tools are used to fill any crystalline regions not captured by the threshold. Note that some crystals were not completely in focus, indicating they were slightly out of plane, but these were included in the processing. Figure 4.4 shows an example of an original transmission image and its binary counterpart. Finally, the crystalline area per image was recorded in a spreadsheet using the 'area fraction' measurement. As with the fluorescence channel, a value of 1 denotes a fully crystalline image and a value of 0 denotes a fully liquid image.

4.4 Simulation Results

Here the results of COMSOL simulations are discussed, firstly simulation results of oil-filled sample cells in non-uniform and uniform stage configurations and secondly with the addition of water droplets, modelling a dilute emulsion.

4.4.1 Hexadecane

Temperature profile

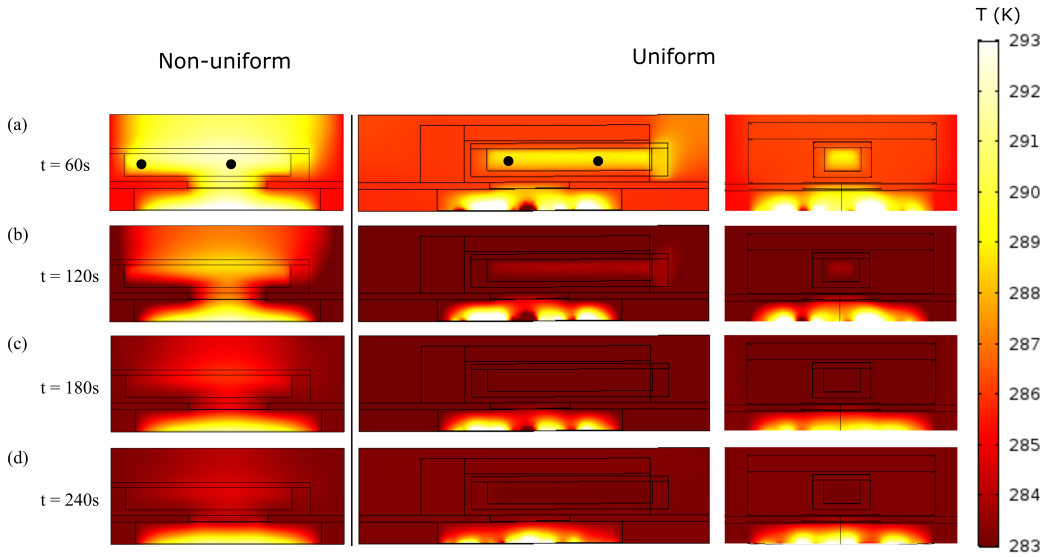

Figure 4.5 *Temperature profile simulation results of oil cooling in non-uniform and uniform configurations at selected timesteps. In the non-uniform setup, the temperature varies throughout the sample, whereas in the uniform setup the sample temperature is more uniform and the gradient through the sample lower. The uniform sample also reaches 283 K sooner than the non-uniform sample. Black dots mark the location of temperature measurements used to plot the graphs in Fig. 4.6.*

Figure 4.5 shows simulation results of a sample cooling in uniform and non-uniform setups at 8 K/min at 4 timepoints. A cooling rate of 8 K/min is used as this is the highest rate used in experiments and likely to show the strongest effect on the temperature profile. The whole setup begins at 293 K (20 °C) and is cooled to 283 K. The first column shows the non-uniform results and the next two columns show the uniform results. The uniform results are shown from 2 angles: the long axis of the cuvette is shown in column 2 to show the same *sample* orientation as the non-uniform case, and the short axis is shown in column 3 to show the same *stage* orientation as the non-uniform images (the sample is rotated in the stage between configurations as shown in Fig. 4.3).

In the non-uniform case, as the temperature is reduced at the cooling wall, the aluminium components cool at almost the same rate due to their direct contact with the cooling wall and their high thermal conductivity whereas the air surrounding the cuvette cools more slowly. In addition, the heat flux into the sample from the bottom glass window leads to a warmer region below that region of the sample. The combination of these different cooling rates around the sample leads to uneven cooling of the oil sample, with the region above the window the slowest to cool.

In the uniform case, the uneven cooling is significantly reduced by the surrounding the whole sample with a single material - the aluminium casing. This makes the sample more uniform in temperature along the long axis as shown in Fig. 4.5 column 2. The only exception is where the cuvette end sits outside the metal casing. There is a slight temperature difference between the bottom and top of the oil in the cuvette but not as significant as the differences observed in the non-uniform case. The third column shows that there is some variation between the outside and inside of the oil and the oil cools from the outside inwards, but again this is much lower than variations observed in the non-uniform case. The sample also cools more quickly than in the non-uniform case as seen by the colour difference between columns 1 and 2 in panels (b) and (c). Extracting the temperature at each timepoint for the locations shown in Fig. 4.5 shows that the non-uniform sample takes around 70s for both points to drop below the freezing temperature of hexadecane, while in the uniform case this takes only 40s.

It should be noted that the temperature profile in the air gap between the windows appears different between the two setups, but the reason for this is unclear. It may be that as the aluminium completely covers the glass window in the uniform case, unlike the non-uniform case where the window is only partly covered by the cuvette, this causes a change to the heat transfer in that region.

The temperature difference between two points in the sample cell can be plotted as a function of time for both uniform and non-uniform cooling. This is shown in Fig. 4.6 where the two points in the cuvette are at a similar location to that of the thermocouples used in experiments. As observed in the images, the temperature difference is much stronger in the non-uniform case than in the uniform case. The uniform results would be expected to show the same pattern in experiments, but in the non-uniform case, some differences could arise due to the phase change not being modelled here. A phase change could cause a larger temperature gradient as parts of the sample solidify at constant temperature

while other parts simultaneously continue to drop as they are yet to freeze.

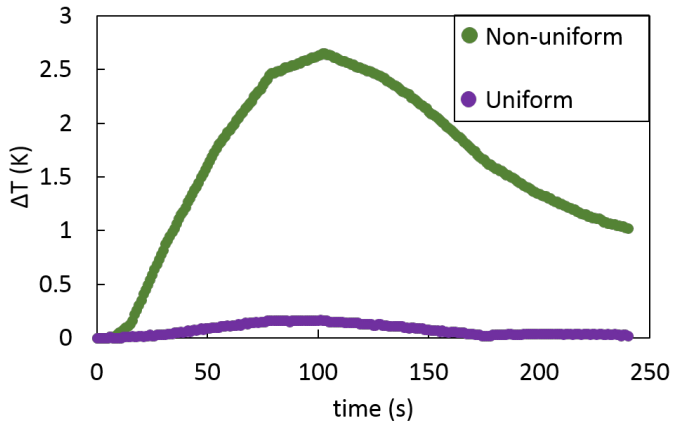

Figure 4.6 *Temperature difference between two points in the sample cell (marked in Fig. 4.5) as a function of time during uniform (purple) and non-uniform (green) cooling.*

Velocity profile

Figure 4.7 shows how the velocity in the fluid components varies during both non-uniform and uniform cooling. In both cases the velocity of the air is several orders of magnitude larger than the velocity of the hexadecane due to its lower dynamic viscosity. The hexadecane velocity is $\mathcal{O}$ (10^2 μm/s) in both cases, and the uniformity appears to affect the fluid flow profile more than the magnitude. In the non-uniform case the profile is affected by the presence of the glass window. The fluid flow is directed upwards at that point, but then splits and flows in a clockwise and and anti-clockwise loop into the two ends of the cuvette. This is a result of the temperature profile shown in Fig. 4.5 where there is heat drawn into the cuvette via the window. In the uniform case, the velocity is slightly higher at the enclosed end of the cuvette and at the centre than the edges, but is otherwise more uniform than the non-uniform case.

Effect of cooling rate

The cooling rate can be varied by altering the piecewise function, presented in Equation 4.1, controlling the cold wall temperature. Due to computational

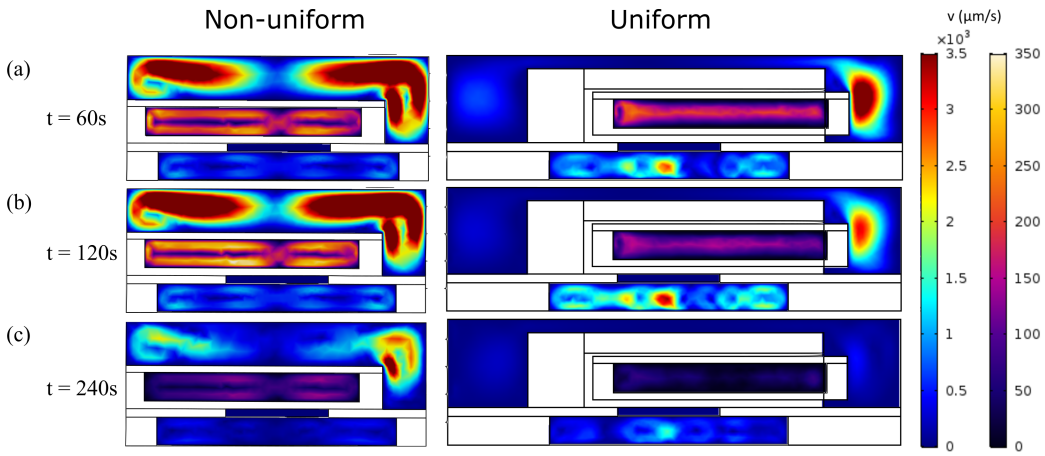

Figure 4.7 *Velocity profile results of oil cooling in both the non-uniform and uniform setups at (a) 60s, (b) 120s and (c) 240s. The oil and air are colour-coded differently due to the different orders of magnitude in the velocities.*

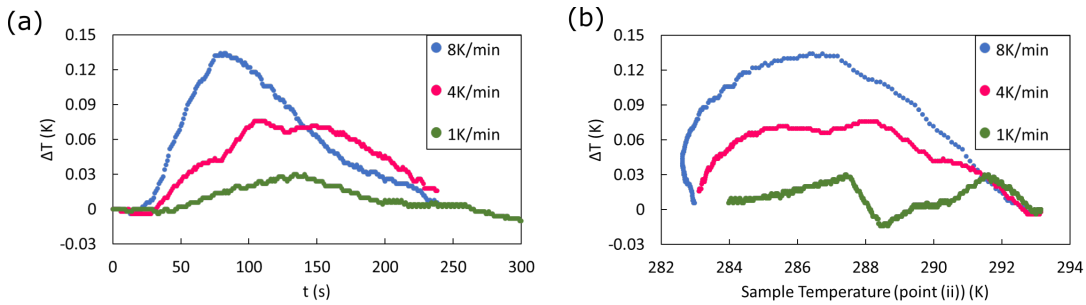

Figure 4.8 *Temperature profile results of oil freezing in the uniform setup as a function of cooling rate. Cooling rates of 1, 4 and 8 K/min. Values for ΔT have been smoothed using a central moving average of 5 points to reduce the noise in the plots. (a) Temperature difference between points (i) and (ii) as a function of time. (b) The same temperature difference plotted as a function of the temperature at point (ii). The peak temperature difference for each cooling rate occurs around the same sample temperature although the slowest cooling rate displays 2 peaks rather than 1. Towards the end of the simulation of an 8K/min run (blue curve), the sample temperature showed a slight increase, thus the curve appears double valued at low temperature.*

constraints, only uniform cooling simulations at different rates were carried out. The results of temperature variation along the sample for 3 different cooling rates during uniform freezing are shown in Fig. 4.8, where the temperature difference is calculated from two points as shown in Fig. 4.5. It can be seen that decreasing the cooling rate decreases the temperature gradient in the sample as the peak ΔT value decreases with decreasing cooling rate. Panel (a) shows that as cooling rate increases, the sample more quickly reaches the peak temperature difference, which, as panel (b) shows, occur at around the same temperature in each sample. At the slowest cooling rate, a second peak is also visible. The reason for this is unclear, however, the temperature differences there are so small that any fluctuations in the temperature at either point could cause a peak in the curve.

These temperature gradients may all be small in comparison to the measured temperature gradients because the freezing transition will affect these results, however it is still clear that the cooling rate does affect the temperature profile in the sample. Interestingly, the curves in panel (b) closely overlap at temperatures above the experimental freezing temperature of hexadecane (291 K) which may indicate that changing the cooling rate affects the temperature gradient less than simply the time taken to reach the freezing temperature.

4.4.2 Hexadecane with droplets

Simulations with oil alone are useful because they provide understanding of the heat transfer through the sample cell and of the difference between uniform and non-uniform configurations. However, in the majority of our experiments emulsions are used and these contain water droplets. Water has a heat capacity and thermal conductivity around twice as large as those of hexadecane and as such the droplets could be expected to alter the heat transfer in the sample cell. Droplets were added into the simulated sample cell for both uniform and non-uniform cooling, as shown in Fig. 4.2.

Temperature profile

Figure 4.9 shows a comparison of the temperature profiles of a sample with and without droplets cooling at 8K/min for the two stage configurations. In both cases, there is a difference in the temperature profile, with the droplets and the

surrounding region taking longer to cool. The higher heat capacity of water may be the cause of this *i.e.* more thermal energy must be removed to lower the water temperature, therefore it would be expected that the water would cool more slowly and this affects the surrounding oil. Similar effects are observed in both uniform and non-uniform cases although the global behaviour is still the same as without droplets.

Velocity profile

Given that the droplets change the temperature profile of the sample, it could be expected that this would result in an altered velocity profile. Indeed, looking at both uniform and non-uniform plots, shown in Fig. 4.10, the velocities are an order of magnitude higher in the region surrounding the droplets than in the bulk. The effect is greater in the non-uniform case initially, particularly for the three touching droplets which are in the region above the glass window, and then drops to a similar level as the uniform case at later times. The disturbance also lasts longer in the uniform case than the non-uniform case. The increased velocity may be a result of a larger local temperature gradient as observed in Fig. 4.9, but it may also be a result of constricted flow between the droplets and the wall. The droplets are an order of magnitude larger in simulation than in experiment, and also cannot deform or move in the simulation. This could lead to a larger disturbance to the flow than would be expected in experiments where the droplets are smaller and able to move and rotate in the flow.

4.5 Experimental results

In this section, the experimentally measured temperature profiles in both uniform and non-uniform setups are presented and discussed. Confocal fluorescence images of crystal growth are included and the differences between cooling rates and stage configurations are discussed.

4.5.1 Temperature profile

For both uniform and non-uniform freezing, temperature versus time measurements were taken at two points, marked as (i) and (ii) in Fig. 4.3, during freeze-

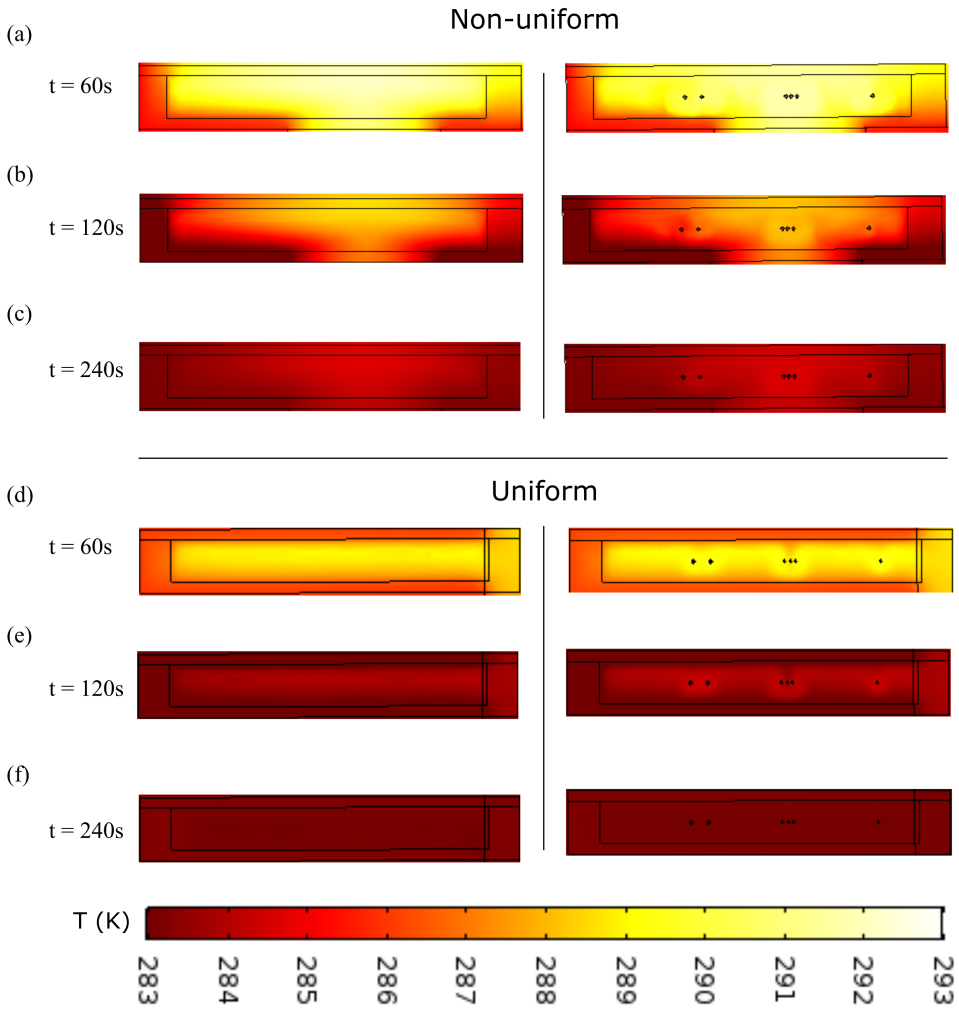

Figure 4.9 *COMSOL simulation results showing simulations of (a-c) non-uniform and (d-f) uniform samples cooling without droplets (left) and with droplets (right). In both cases, there is a small amount of disturbance in the temperature profile around the droplets shown by the difference in colour around them compared to the bulk oil. Further away from the droplets, the profile shows little noticeable change from the simulations without droplets.*

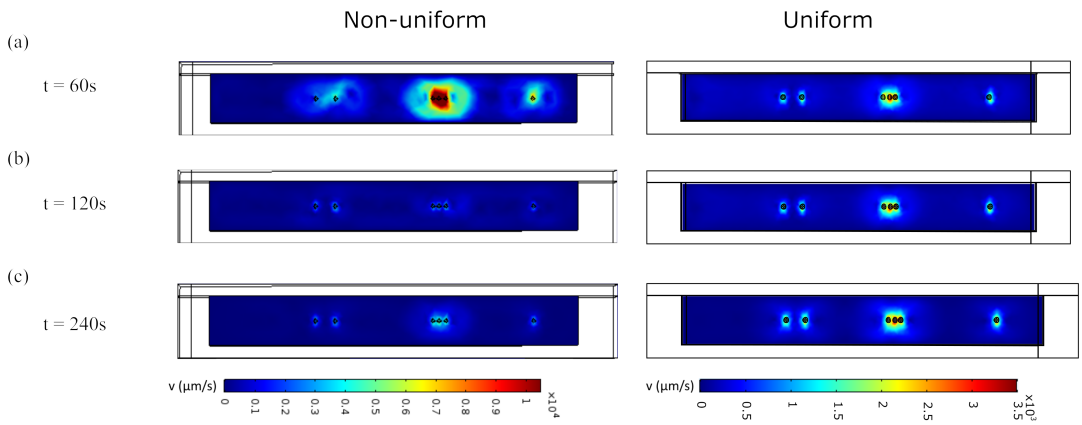

Figure 4.10 *COMSOL simulation results of the velocity profile in non-uniform and uniform simulations containing droplets at timesteps of (a)60s, (b) 120s and (c) 240s. In both cases the velocities are higher than those observed in Fig. 4.7 where no droplets are present.*

thaw cycles at varying rates. Figure 4.11 shows a typical pair of temperature-time curves recorded for (a) uniform and (b) non-uniform freezing at 8 °C/min. These curves show different profiles for uniform and non-uniform cooling.

In the uniform case, the curves for the two points within the sample overlap closely, apart from over one short time period, and both show undercooling followed by a sharp increase in temperature when the sample begins to freeze. In contrast in the non-uniform case, point (i) cools more quickly than point (ii) and thus freezes first. As the oil crystallises, latent heat is released, resulting in a plateau in the temperature-time curve. Point (i) also takes a shorter amount of time to freeze, seen in the shorter plateau in the curve. In this sample, undercooling is seen only at point (i). At point (ii), imaging shows that crystals are already present as the region reaches freezing temperature, therefore crystals here grow can by heterogeneous rather than homogeneous nucleation, reducing the need for undercooling.

Fig. 4.11 (c) shows the temperature difference over time between points (i) and (ii) for each setup. In the uniform case, there is a maximum temperature difference between the two thermocouples of less than 0.4 °C except at two points. The first, at around 180 s, is due to the oil freezing at point (ii) marginally before point (i). The second, at around 325 s, is most likely a residual effect of the viewing hole in the aluminium casing which, although much smaller than the

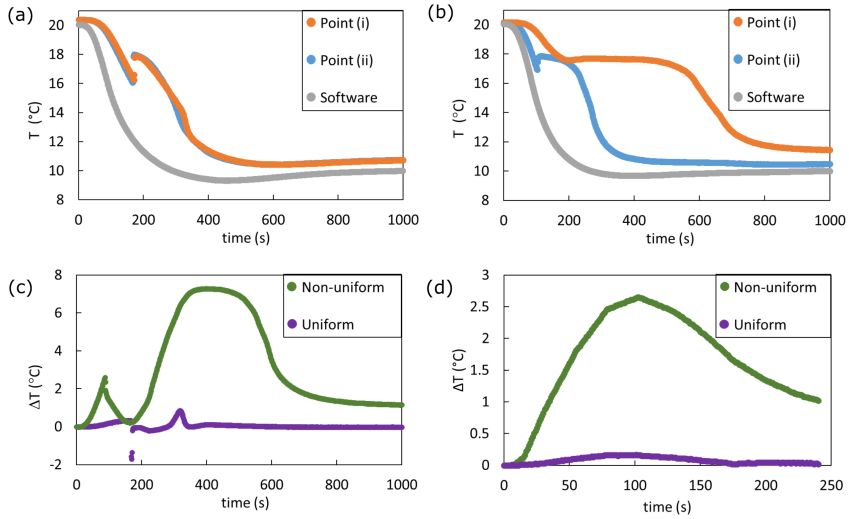

Figure 4.11 *(a)-(b) Typical temperature-time curves recorded at points (i)(orange) and (ii)(blue) marked in Fig. 4.3 in oil-filled sample cells during (a) uniform and (b) non-uniform freezing at 8 °C/min. Grey curves show the recorded software temperature in each case. (c-d) Temperature difference between points (i) and (ii) during uniform(purple) and non-uniform(green) freezing for (c) experiments and (d) COMSOL simulations*

window in the non-uniform case, may cause a small deviation in the temperature profile. In the non-uniform case, there is a more pronounced temperature gradient along the sample, with a maximum temperature difference of around 7 °C. This is due to the longer and later phase transition time at point (ii) than point (i), thus the temperature drops at (i) while the temperature at (ii) is constant, leading to a larger temperature difference. The curves are similar in trend to those observed in the COMSOL simulations, shown in Fig. 4.11 (d). Although the values of ΔT differ between experiment and simulation, this can be attributed to the phase change observed in experiments but not present in the simulations, as discussed earlier.

4.5.2 Software-to-sample temperature relation

The temperature recorded by the software during freezing experiments generally does not reflect the actual sample temperature. This can be seen in Fig. 4.11 (a) and (b), where the software recorded temperature (grey) is different to both measured points in the sample (orange and blue) at any given timepoint.

However, assuming that the samples behave in a similar manner during each freeze-thaw cycle, the same sample temperature will correspond to a given software temperature each time. Thus the results shown in Fig. 4.11(a)-(b) can be used if required to convert between software and sample temperature for each stage setup at a given cooling rate. This assumption may not be completely accurate as the simulations presented earlier do suggest that the emulsion samples may cool more slowly with the presence of droplets altering the temperature profile (see Fig. 4.9). However, the behaviour in emulsion samples is at least more closely aligned with the pure oil sample temperature than the software temperature which displays no signs of the freezing transition at all. Thus, using the relevant oil sample temperature as a measure of the emulsion sample temperature is more accurate than relying on the software temperature alone.

4.5.3 Crystal growth

Having observed that the temperature profile of a sample varies with the uniformity of cooling, the effects of these profiles on the crystal growth are now of interest. Using visual observations from confocal microscopy and image analysis, the main differences in the crystal growth mechanisms can be explored.

Uniform freezing

As uniform cooling produces a small temperature gradient along the length of a sample, the oil crystallises at almost the same time throughout the sample. This is observed in Figure 4.12 which shows oil crystallisation over time during an 8 °C/min temperature ramp in the uniform setup. When crystallisation begins, several crystals (black) appear in the field of view together and cross the whole length of the field of view in less than the time between frames (1.56 s). Once crystals have appeared, they continue to grow more slowly and over time more crystals grow into the field of view until the whole region is filled.

Non-uniform freezing

For the non-uniform case, different crystallisation kinetics are expected. As shown by the results in Fig. 4.11(b), the sample does not crystallise all at once, but the end in contact with the cooling wall freezes sooner than the region above the

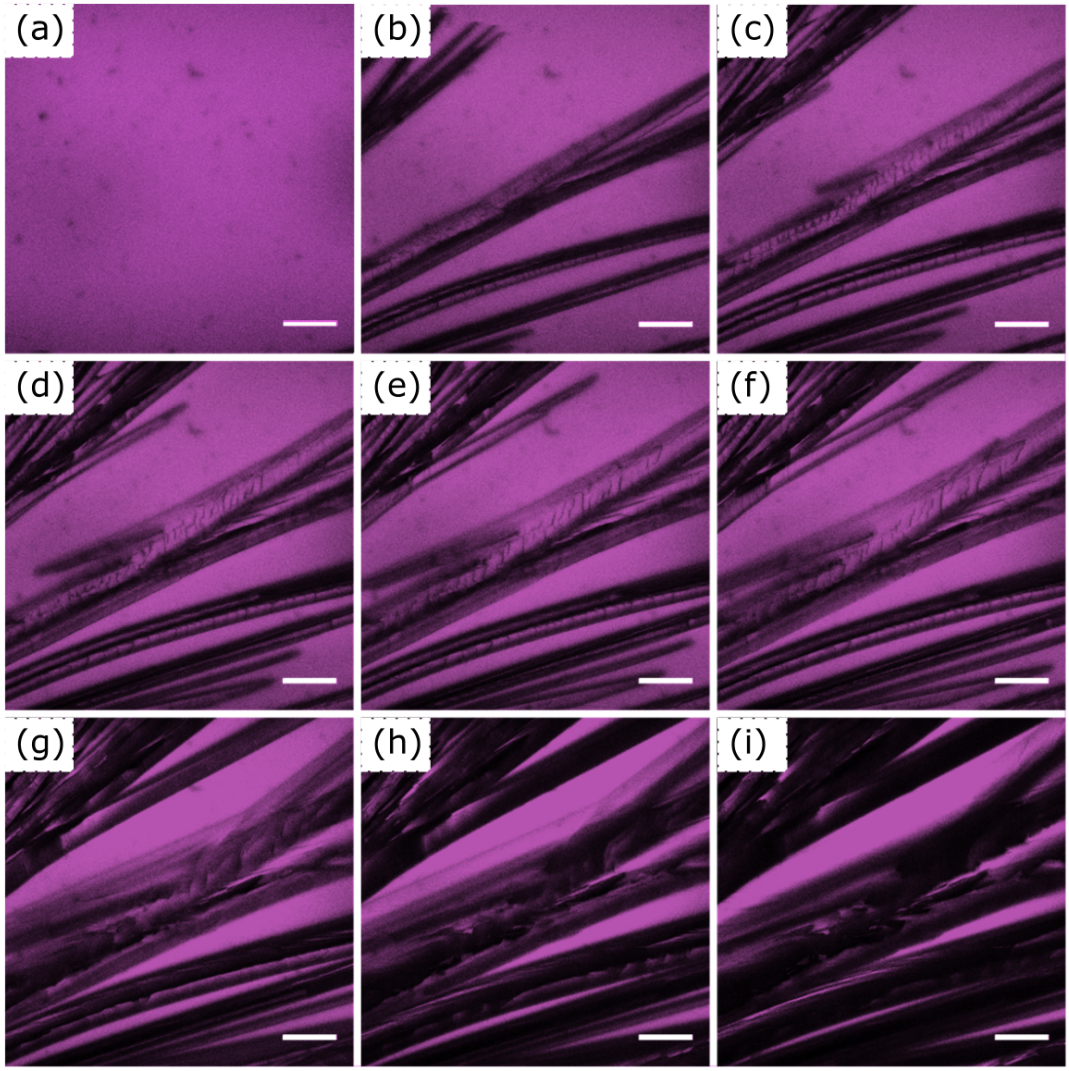

Figure 4.12 *Confocal images of oil freezing during 8 °C/min uniform cooling. Liquid oil is magenta, as oil freezes the fluorescent signal is lost, so crystalline regions are black. Images (a)-(f) spaced 1.6s (1 frame) apart, (f)-(i) spaced 9.4s apart. Scale bars: 100 μm.*

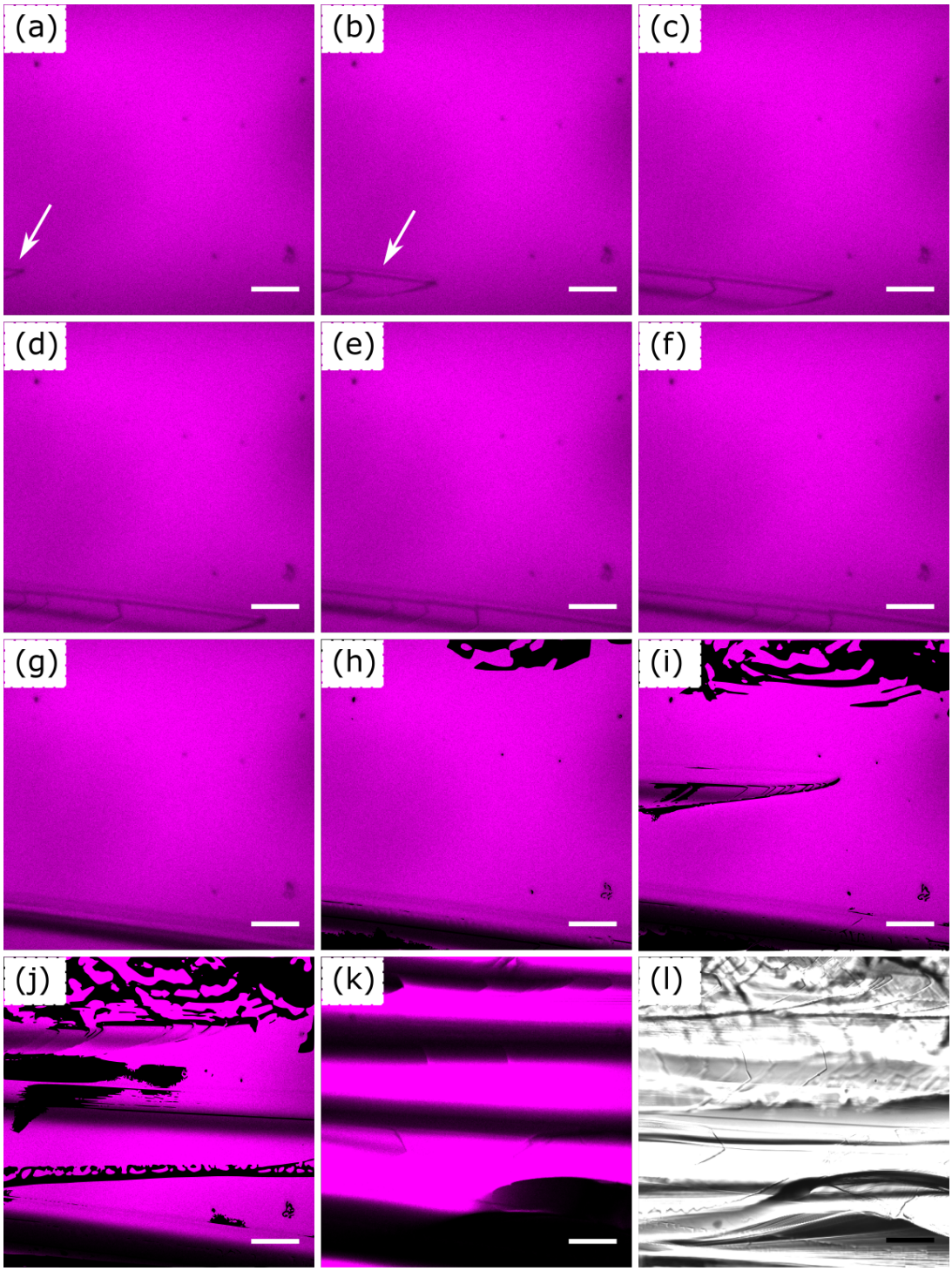

Figure 4.13 *Confocal images of oil freezing during 8 °C/min non-uniform cooling. (a)-(f) 1.6s apart, (f)-(j) 31.2s apart, (k)-(l) fully frozen sample in (k) fluorescence and (l) transmission channels. (h)-(j) have thresholded transmission images overlaid to show the large crystalline region at the top of the image visible in transmission but not in fluorescence (due to being out of plane). Scale bars: 100 μm.*

viewing window. In this case, crystals will grow from the cooler end of the sample towards the viewing region.

Figure 4.13 shows oil crystallisation over time for a sample undergoing non-uniform cooling at 8 °C/min. A single crystal (white arrow in panels (a-b)) grows into the field of view, taking around 6s to cross the whole field. Early on the crystal appears to grow primarily in the direction of travel. Some broadening of the crystal happens later on, seen in panels (g) - (k) as the black streak widens. More plate-like crystals grow from panel (i) onwards at the top of the image which do not show up in fluorescence, but are represented by overlaid outlines from the transmission channel images. Panels (k) and (l) show the field of view once completely frozen in fluorescence and transmission channels.

Compared to uniform freezing, in which many crystals appear in a single frame, crystallisation occurs over a much longer timescale. This difference in behaviour is likely to be due to the presence of the strong temperature gradient in the non-uniform sample. In the non-uniform setup, the ends of the sample freeze ahead of the region above the field of view, therefore crystals nucleate there and grow before they begin to nucleate in the viewing region.

Comparing uniform and non-uniform cooling via image analysis

Having observed the differences between uniform and non-uniform freezing visually, quantitative analysis of the differences is pursued. Thus image analysis of both fluorescence and transmission channels is carried out as described in Section 4.3.3.

One point to note is the difference in analysis methods between the fluorescent and transmission channels. Analysis of the transmission channel images is more labour intensive as it requires manual handling of each image, whereas analysis of fluorescent images is done automatically through ImageJ. However, the fluorescent channel does not always show the full crystal structure as any crystals out of the narrow focal plane may not be detected in the fluorescence channel. An example of this is shown in Fig. 4.13(k)-(l) where there are bright fluorescent regions in the fluorescence channel image, (k), but the transmission image, (l), is completely crystalline. In Fig. 4.14(a), the calculated crystal fraction is plotted as a function of time for both channels in uniform and non-uniform cooling. Although quantitatively the curves are different, qualitatively they show

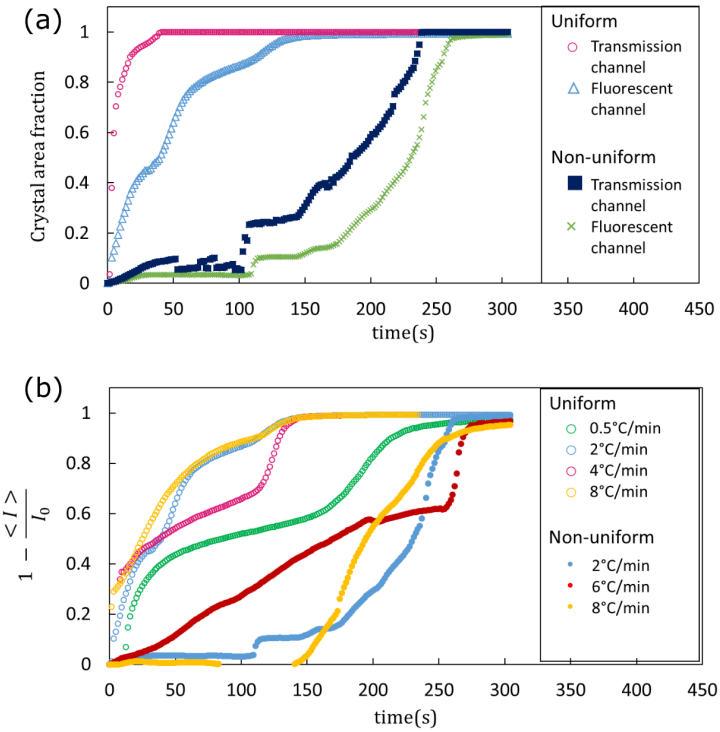

Figure 4.14 *(a) Crystal fraction extracted from fluorescent and transmission images for freezing of oil-filled sample cells at 8 °C/min. (b) Normalised average intensity of fluorescent channel images at different cooling rates. One curve drops below zero between 56-92s because as the oil begins to freeze, the intensity of the liquid oil increases to a higher value than prior to freezing, leading to negative values for* $1 - \frac{<I>}{I_0}$. *$t = 0$ is one frame (1.56 s) before crystals appear in the transmission channel.*

the same behaviour, therefore further analysis is carried out using the fluorescent channel data only.

The curves obtained for both uniform and non-uniform freezing can now be discussed in more detail. In Fig. 4.14(a), there is a clear difference between the crystallisation during uniform and non-uniform cooling. As observed in the confocal micrographs, the non-uniform samples reach complete crystallisation more slowly than the uniform samples once crystals begin to appear in the field of view. The shape of the curves is also different: in the uniform case, the curves have a steep gradient until nearly full crystallisation is achieved, whereas in the non-uniform case, the initial gradient is much shallower but becomes steeper later on. The reason for this is that generally in the uniform case, many crystals appear at once, therefore the crystal fraction increases rapidly and then slows down as the

remaining gaps are filled. In contrast in the non-uniform case, typically a single crystal is observed growing into the field of view which remains alone for a longer period of time, leading to a shallow gradient initially. Once crystals begin to form in the observation region as it reaches freezing temperature, crystallisation speeds up, thus the gradient of the curve increases.

4.5.4 Effect of cooling rate

Varying the cooling rate has been shown by the simulations above to affect the time taken for the sample to reach freezing temperature, but it is still unclear whether it also affects the temperature gradient along the sample. Both of these factors may affect the oil crystallisation, thus the cooling rate is varied in both stage configurations.

Fig. 4.14(b) shows the results of image analysis on experiments carried out at different cooling rates. It can be seen that the uniform and non-uniform results are clearly separated, except for the uniform cooling at 0.5 °C/min where the crystal signal in the fluorescent channel was poor. However, no clear trends appear with cooling rate. This shows that the primary effect of cooling rate is to alter the time until crystallisation begins, while crystallisation is dominated by crystal nucleation and the uniformity of the sample temperature profile.

4.6 Discussion

Both experimental and simulation results show that the set-up in Fig. 4.3 (a) yields non-uniform cooling, whereas the set-up in Fig. 4.3 (b) yields relatively uniform cooling. Although there are quantitative differences between simulation and experiment due to the simplifications made in the COMSOL model, qualitatively the behaviour is the same. Samples cooled in the 'uniform' setup exhibit a much lower temperature gradient along them and the whole sample reaches the oil freezing temperature at almost the same time, whereas non-uniformly cooled samples experience a stronger temperature gradient and freezing is progressive along the sample length. Both sets of results show the importance of understanding the experimental setup before measurements are carried out because the different setups produce vastly different temperature profiles.

The microscopy results show that the difference in temperature profiles has a clear effect on the kinetics of crystal growth, both in speed and structure. The use of temperature gradients to control structure in the field of freeze-casting and ice-templating is well known, as mentioned earlier. In these cases, the behaviour of the continuous phase crystallisation to expel particles and create porous materials relies, among other factors, upon the applied temperature gradient [118]. Therefore differences in temperature profiles would be expected to have an effect on the behaviour of particle-stabilised emulsions upon freeze-thaw cycling. Simulation results show the effect droplets have on the temperature profile and the droplets can be affected by the crystal formation. In addition, if heterogeneous nucleation is dominant, particle-stabilised droplets may provide additional nucleation sites on which crystals can nucleate.

It should be noted that the crystal growth behaviour observed here will not necessarily be mimicked by the emulsions directly. Here the oil crystallises in bulk, whereas in an emulsion the oil is filled with droplets which may impede the growth of larger crystals. In a dense emulsion, the oil may even be found only in thin films between the droplets. Thus although the behaviour here clearly indicates that the crystal growth is different between uniform and non-uniform cooling, the nature of the crystals forming in an emulsion may be different to those forming in bulk.

Finally, the difference in behaviour between the two cooling setups is industrially relevant as non-uniform cooling is common in production and consumer use, *e.g* using a freezer with an unknown temperature profile, but trends are difficult to extract. On the other hand, uniform cooling more easily allows the observation of trends because the temperature profile is more even, but is less representative of freezing in a real-life setting.

4.7 Conclusions and future work

In this chapter, COMSOL simulations have been used to determine the temperature profile through a sample using a model of the experimental setup described in Chapter 3. In the non-uniform setup, there is a strong temperature gradient in the sample resulting from differences in heat transfer through the different materials surrounding the sample cell. In the uniform case, the temperature gradient is much smaller than in the non-uniform case and less time is required for

the whole sample to drop below the oil freezing temperature. The experimental results corroborate the simulation results in showing that shifting from uniform to non-uniform cooling leads to substantial differences in temperature profiles.

Using confocal microscopy to image oil crystallisation in both stage configurations has shown that the temperature profile difference between configurations leads to significant differences in the oil crystallisation kinetics. The difference in crystallisation has also been quantified via image analysis. During uniform cooling, many crystals grow at the same time, while in non-uniform cooling crystals in the viewing region grow more slowly as crystals grow into the region from cooler parts of the sample before the oil in the viewing region begins to crystallise.

Overall these results show the importance of characterising the temperature profile in an experimental setup in order to understand the behaviour of more complex samples. The sample behaviour can then potentially be broken down into aspects which result from the temperature profile and those which are due to the sample structure itself.

In future simulations, it would be interesting to observe the effects of many droplets in the sample cell, akin to the situation for an emulsion-filled sample. It is already clear that even a few droplets affect the temperature and velocity profiles, thus many droplets would be expected to enhance the effect. The simulations could also be improved by modelling the phase change as this would give a more realistic view of the temperature profile as the sample freezes. Finally, modelling mobile, rather than static, droplets would show how the heat transfer would be different for an emulsion and how the phase change affects the droplet motion and thus the temperature profile.

In future experimental work, it would be interesting to scale up the sample size in order to understand both how the temperature profile is affected by size, as well as how the crystallisation may change. It would also be beneficial to observe the behaviour of a sample placed into a pre-cooled environment rather than placing into a chamber at room temperature and cooling from there. These changes would link our results more directly to household or industrial applications where the products used are generally much larger than the samples available here and are typically placed directly into a freezer already below the freezing temperature of the product.

Chapter 5

Individual particle-stabilised droplets interacting with growing crystals

5.1 Introduction

Particle-stabilisation of emulsion droplets, effective due to the partial wetting by the particles of both fluid phases [10], has been of interest since the start of the 20^{th} century [17, 18]. The theory behind this stabilisation has been discussed in Chapter 2. On a single droplet level, in the last couple of decades interest has increased with the development of 'armoured droplets' from the discovery by Aussillous and Quéré that hydrophobic grains would attach to a water droplet, producing what they called 'Liquid marbles' [127], to the use of particle stabilisation in the formation of colloidosomes - microcapsules with a shell of colloidal particles [128, 129]. Liquid marbles tend to be $\mathcal{O}$(mm) in radius and are stabilised by hydrophobic particles $\mathcal{O}$ (10^1 - $10^2\mu$m) so are larger than typical colloid-stabilised emulsion droplets where the particles are $\mathcal{O}(\mu\text{m})$. Colloidosomes are formed from particle-coated emulsion droplets, where the particle shell is then reinforced using mechanisms such as polymerisation of the particles or thermal annealing. The resultant microcapsules have applications in industries such as the pharmaceutical, personal care and agrochemcial sectors for the controlled release of active ingredients such as drugs [130] .

The deformation of particle-coated droplets has been studied under a range of conditions such as: buckling under internal fluid removal/evaporation [131–

133] shear flow [49, 134–136] and electric fields [50]. The dynamics of droplet deformation are important for the processing of particle-stabilised emulsions for use in industries such as food and cosmetics. In addition, some industries, in particular the oil industry, desire the breakup of particle-stabilised emulsions and as such understanding droplet breakup is a key part of the process [4]. It has also been suggested that in some cases, such as drug delivery, non-spherical droplet geometries may be more appropriate than spherical ones [137, 138], thus there may be a requirement for the stabilisation of deformed droplets, an outcome that requires the use of techniques such as arrested coalescence or the deformation of droplets in the presence of excess particles [139–141].

Particle stabilised droplets have been shown to relax over longer timescales after deforming under an applied stress than bare droplets, with relaxation timescales increasing from milliseconds for bare droplets to hours or even days for particle-coated droplets [131, 142]. It is particularly dependant on the surface coverage of particles - lower coverage makes it easier for the droplets to return to spherical whereas at higher coverage it is more difficult as the particles jam more easily [135]. This shows that in droplet deformation, the particle behaviour at the interface is key in determining the droplet response to applied external stress as the particles cause the interface to become a two-dimensional solid [131, 133]. Computational simulations of particles on droplet interfaces show that during a deformation, the particles are free to move around on the interface and as such affect the deformation of a droplet by moving to regions of low shear or high curvature, leading to inhomogeneous particle distribution over the surface [49]. Experimental studies of particle jamming at droplet interfaces have shown that the extent and timescale of droplet deformation also affect the jamming of the particles [143].

As discussed in Chapter 2, freezing is a technique commonly used in the food and pharmaceutical industries both for transport and storage. With regard to a droplet suspended in another fluid during freezing, there are two cases to consider: either the droplet freezes (first) or the continuous phase freezes (first). When a continuous phase freezes around an insoluble second object, whether that be solid particles, liquid droplets or air bubbles, an interaction takes place between the crystals of the continuous phase and the object, known as an inclusion [144]. The alternative situation is when the inner phase of a droplet freezes. In this case, the surrounding phase is less important, but the droplet is still affected, as the crystallisation of the inner droplet phase can force a change in droplet shape,

as has been shown for liquid marbles [145] and surfactant-stabilised oil-in-water emulsions [81, 146]. Here, the first of these cases *i.e.* a freezing continuous phase with a liquid droplet remaining unfrozen, is considered.

In this chapter, experiments on the deformation of particle-stabilised water droplets interacting with growing crystals are presented. This is achieved using a dilute water-in-hexadecane emulsion subjected to freeze-thaw cycles. The hexadecane freezes but the droplets remain liquid, allowing the behaviour of the droplets to be determined by the growing oil crystals. The crystallisation of hexadecane has been discussed in Chapter 4 and now the interaction of these crystals with particle-stabilised droplets is explored. The particles enhance droplet stability and thus would be expected to provide some resistance to droplet deformation, but should the force applied by the crystals be much larger than that resistive force, the droplets will inevitably deform. Confocal microscopy is used to study the droplet shape before, during and after freeze-thaw cycling, in particular to observe whether or not it reverts back to its original shape. The effects of particle jamming at the interface and its effect on the droplet structure are also discussed.

5.2 Theoretical framework

During the freeze-thaw process, the droplets feel pressure from growing oil crystals resulting in droplet deformation. From our observations, two main shape characteristics can occur - buckling of the droplet interface and stretching of the interface. In both cases, the surface area of the droplet increases, but in the first case the droplets may remain spherical on average, while in the second the surface is smooth but the overall shape non-spherical. The two cases are shown schematically in Fig. 5.1

Quantitative analysis of droplet behaviour will illuminate the predominant shape changes during freeze-thaw cycling and any recovery of droplet shape which may occur upon thawing. The shape of a droplet is characterised by taking a 2D slice through the centre of the droplet. The changing shape of the droplets is then quantified using two shape descriptors: circularity and Feret diameter. Two-dimensional analysis is considered here due to imaging constraints in the experimental setup *i.e.* the size of the droplets is typically $\mathcal{O}(10 - 100\mu\text{m})$ and as such the whole depth of the droplet cannot always be imaged in the confocal

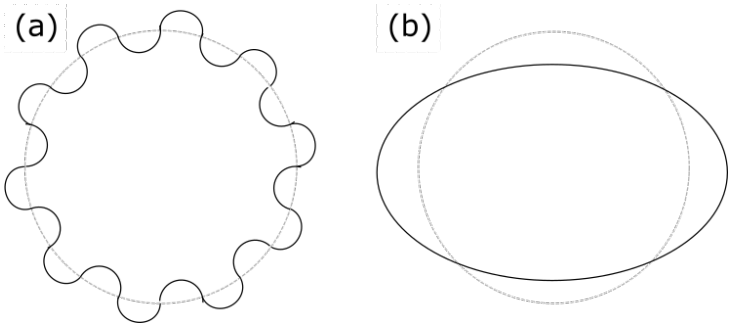

Figure 5.1 *Schematics of (a) buckled droplet distortion and (b) stretched droplet distortion. Solid lines show the distorted shape and dashed lines a perfect circle.*

microscope, even prior to freeze-thaw cycling. This is due to the large distance between objective and sample resulting from the configuration of the temperature stage and confocal microscope, as described in Chapter 3.

5.2.1 Circularity

Circularity, also known as the Isoperimetric Quotient [147], is a measure of how close a shape is to a circle. It is defined as

$$C = 4\pi \frac{A}{P^2} \ , \tag{5.1}$$

where C is circularity, A is shape area and P is shape perimeter.

It is derived by determining the ratio of a shape's area to the area of a circle with the same perimeter.

The area and perimeter of a circle are given by

$$P_{\text{circle}} = 2\pi r_{\text{circle}} \ . \tag{5.2}$$

$$A_{\text{circle}} = \pi r_{\text{circle}}^2 = \frac{P_{\text{circle}}^2}{4\pi} \ . \tag{5.3}$$

where r_{circle} is the radius of the circle. For a shape of given perimeter P_{s} and area

A_s, a circle with the same perimeter has an area

$$A_{\text{circle}} = \frac{P_s^2}{4\pi} \ . \tag{5.4}$$

Thus

$$C = \frac{A_s}{A_{\text{circle}}} = \frac{A_s}{\left(\frac{P_s^2}{4\pi}\right)} = \frac{4\pi A_s}{{P_s}^2} \ . \tag{5.5}$$

For a circle, $C = 1$ and as the perimeter-area ratio increases, $C \to 0$.

5.2.2 Feret Diameter

Feret diameter, D_f, also called the calliper diameter, is defined as the perpendicular distance between two parallel tangents on the surface of an object, as shown in Fig 5.2 [148].

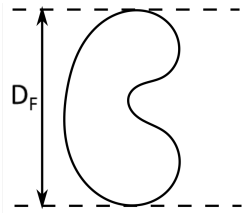

Figure 5.2 *Schematic showing the (maximum) Feret diameter of an arbitrarily shaped 2D object.*

For any shape, the maximum and minimum Feret diameters, f_+ and f_- , can be determined. The ratio of these two values,

$$F = \frac{f_-}{f_+} \ , \tag{5.6}$$

gives an indication of how elongated a droplet is, as a circle has $F = 1$ whereas an elongated droplet has $F << 1$.

5.2.3 Feret-circularity phase space

Of the two shape descriptors defined above, neither can alone distinguish between the different droplet shapes or behaviours. It would be useful to be able to distinguish between the two droplet shapes identified above in order to elucidate more easily the effects of oil crystallisation on a droplet, by comparing droplet shapes before and after a freeze-thaw cycle. Thus the results from circularity and Feret ratio must be combined.

Circularity distinguishes the two types of deformed droplets from a circle but not from each other. Any deformed droplet with a perimeter much larger than that of a circle will have a lower circularity, irrespective of what that shape actually is. Therefore a buckled droplet could have equally low circularity as a smooth droplet with a stretched, elliptical profile, despite the overall shape being more circular. F distinguishes between the two types of deformed droplets, but not between a crumpled, almost-circular droplet and a smooth circular droplet (due to the size of the errors in F due to image processing during image analysis and the fact that circular droplets are rarely perfectly circular).

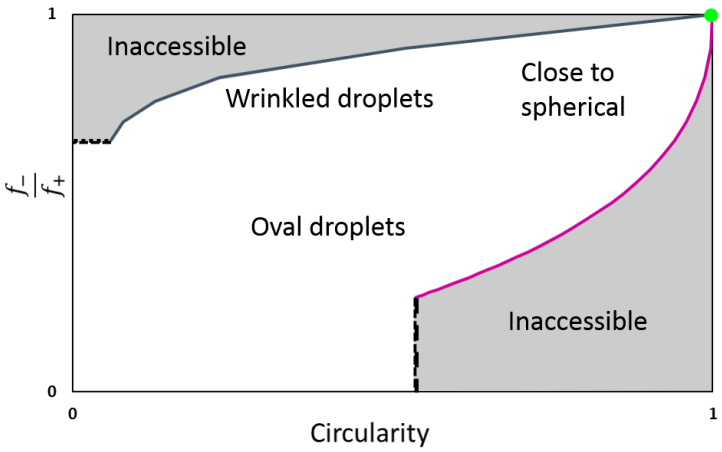

Figure 5.3 *Theoretical phase space for Feret ratio, F, vs circularity, C. The green point at (1,1) denotes the position of a perfect circle and the dark blue and magenta lines the theoretical upper and lower boundaries of droplet existence, calculated as described in the text. Grey regions are inaccessible and dashed lines show the limits of the theories used to calculate the inaccessible regions. Wrinkled droplets which are close to spherical have low circularities but F values close to 1, while elliptical droplets have low circularities and low F values.*

Plotting droplets in a Feret ratio-circularity phase space as shown in Fig. 5.3 does allow different droplet shapes to be distinguishable, as a droplet's location within that space gives an indication of a droplet's shape. Droplets which are perfectly spherical are found at the co-ordinates (1,1). Wrinkled droplets appear at lower circularity values but with F values close to 1. Droplets which are oval will appear at low circularities and at lower F values. The boundary between the wrinkled and eliptical regions is in general ill-defined, therefore unless droplets are deep within these regions, their shape is still not easily identifiable from the phase space alone and images are required. However, useful information can still be derived from this phase space as it allows for both circularity and smoothness to be taken into account simultaneously but distinguishably.

There are boundaries on this phase space which are found by considering ideal or model droplet cases and how they fit into the space, knowing that any droplet observed in experiments will not be expected to cross this 'ideal' boundary.

Inaccessible regions - oval limit

To determine the regions of inaccessibility within this phase space, the behaviour of an 'ideal' ellipse, i.e. an ellipse with no wrinkles is explored. In order to calculate the maximum value of circularity for each value of F, a relationship between F and the ellipse perimeter is required.

The perimeter of an ellipse cannot be exactly expressed analytically, but for ellipses where the ratio semi-major:semi-minor axes $<<$ 4, Ramanujan's Approximation Theorem can be used [149].

$$P = \pi(a+b)\left(1 + \frac{3\lambda^2}{10+\sqrt{4-3\lambda^2}}\right) \ , \tag{5.7}$$

where a and b are the semi-major and semi-minor axis respectively and $\lambda = \frac{a-b}{a+b}$. Using the definition for F given in Equation 5.6 shows that for an ellipse, $F = \frac{b}{a}$. This means P can be re-expressed in terms of F to obtain

$$P = (\frac{\pi b}{F})\left(F + 1 + \frac{3(F-1)^2}{10(F+1)+\sqrt{F^2+14F+1}}\right) \ . \tag{5.8}$$

Now there is still a single explicit dependence on b, but when this expression for

perimeter is used to calculate circularity (by Equation 5.1), circularity becomes

$$C = \frac{4F}{\left(F + 1 + \frac{3(F-1)^2}{10(F+1)+\sqrt{F^2+14F+1}}\right)^2} \ , \tag{5.9}$$

where there is only a dependence on F. Plotting this curve in the F-C phase space shows the series of points a completely smooth ellipse would lie on and, as can be seen in Fig. 5.3 where it is plotted as a magenta curve, this marks out the grey shaded region of high C, low F in the phase space which is inaccessible to elliptical droplets. It can be argued that this region is also inaccessible to wrinkled droplets because these have higher values of F than an elliptical droplet.

Inaccessible regions - wrinkle limit

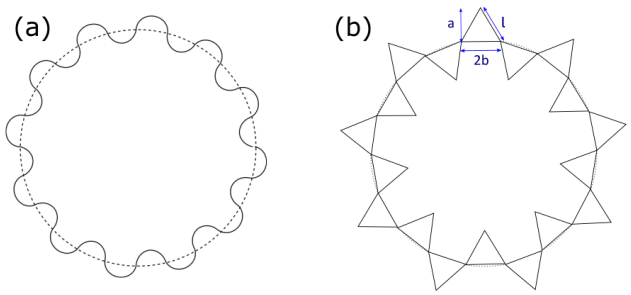

Figure 5.4 *Schematics of (a) Circle with sine wave distortion of perimeter with equal areas of the curve above and below the undistorted circle (dotted line) and (b) Triangular wave distortion of circle perimeter. Triangle has height a and half-width b.*

The inaccessible regions for a wrinkled droplet can now be determined. The 'ideal' case is considered to be a droplet which is on average spherical, but has a surface distortion with equal portions outside and inside the average sphere. In 2D, this translates to a circle with a line distortion such that the area of the circle is still given by πr^2, where r is the 'undistorted' circle radius.

The first requirement is a function to model the wrinkles on a droplet surface. As before, the aim is to obtain an analytic expression relating circularity and the ratio of min/max Feret diameters. It would seem at first that the obvious

choice would be a sinusoidal approximation, i.e. a circle radius r with a sine wave overlaid on the circle perimeter as shown in Fig. 5.4(a). The perimeter is then given by the arc length of a sine curve multiplied by the number of periods. The general expression for arc length, l, is given by the integral [147]

$$l = \int_a^b \sqrt{1 + \left(\frac{\mathrm{d}y}{\mathrm{d}x}\right)^2}\mathrm{d}x \ . \tag{5.10}$$

For a sine curve of the form $y = A\sin(Bx)$, this integral becomes

$$\alpha \int_c^d \sqrt{1 - \beta\sin^2(x)}\mathrm{d}x \tag{5.11}$$

for α, β, c and d constants. This is an elliptic integral of the second kind and is not solvable analytically [147]. Therefore an analytic expression relating C and F cannot be obtained and thus a sine wave approximation is not an appropriate choice here.

As a more basic approximation a sine wave can be modelled simply as a series of semi-circles, each with radius a. An even number of semi-circles is used, such that the area of the distorted circle is equal to the area of the undistorted circle, thus $A = \pi r^2$, where r is the radius of the undistorted circle. Each semi-circle has a perimeter of length $P_{\text{semi-circle}} = \pi a$, (curved portion only) thus the total perimeter is given by $P = n_{\text{semi-circles}} \cdot P_{\text{semi-circle}}$ The number of semi-circles is related to the radius of the undistorted droplet, r, and the radius of the semi-circles, a, by

$$n_{\text{semi-circles}} = \frac{\pi r}{a} \ , \tag{5.12}$$

thus

$$P = \frac{\pi r}{a} \cdot \pi a = \pi^2 r \ . \tag{5.13}$$

From here it can be seen that

$$C = \frac{4\pi A}{P^2} = \frac{4}{\pi^2} \approx 0.4 \ . \tag{5.14}$$

This value for circularity is independent of the size of the 'wrinkles' due to the relationship between r and a and to the height and width of the semicircles being the same.

In order to obtain a more realistic representation of the droplets, a 'wrinkle' profile which has independent height and width is required. For algebraic convenience, a triangular wave distortion to the circle perimeter can be used, as shown in Fig. 5.4 (b). An even number of triangles of side l is used such that the areas of the distorted and undistorted droplets are equal. In this case, the droplet perimeter is expressed as

$$P = n_{\text{triangles}} \cdot 2l = \frac{\pi r}{b} \cdot 2l \ , \tag{5.15}$$

where $n_{\text{triangles}}$ is the number of triangles around the perimeter, r is the radius of the circle and l is the triangle side length, given by

$$l = \sqrt{a^2 + b^2} \ . \tag{5.16}$$

This leads to

$$P = 2\pi r \sqrt{(\frac{a}{b})^2 + 1} \tag{5.17}$$

and

$$C = \frac{1}{(\frac{a}{b})^2 + 1} \ . \tag{5.18}$$

Now F is given by

$$F = \frac{r - a}{r + a} \ . \tag{5.19}$$

Here C cannot easily be expressed directly and solely in terms of F because C depends on both a and b, while F depends on a and r. However, knowing the typical value for r by the average droplet size measured in experiments, and considering the fact that the minimum value for b is the radius of a PMMA particle, both C and the corresponding value of F can be calculated. Plotting

this in the F-C phase space for $r = 50\mu$m and $b_{min} \approx 0.6\mu$m, gives the blue line shown in Fig. 5.3. This can be considered an empirical high F - low C bound on droplets, leading to the second grey inaccessible area on the plot. It will apply both to wrinkled droplets and also to oval droplets which cannot reach such high F values without wrinkles.

5.2.4 Measure of deviation from a smooth, spherical droplet

By combining the results from 5.2.3 together, a relative measure of how close the 2D image of a given droplet is to being both smooth and circular can be obtained. This measure takes into account both the wrinkles on a droplet and the larger-scale droplet deformations away from a circular shape. Considering both the ratio of feret diameters and the circularity in equal measure, the distance between the co-ordinates of a droplet in the phase diagram and the co-ordinates of a perfect circle can be calculated. Using Pythagoras, an expression for the distance between a given data point (C,F) in the F-C phase space and the 'ideal' circular state (1,1) can be determined:

$$R_{\mathrm{NSC}} = \sqrt{(C-1)^2 + (F-1)^2}\ , \tag{5.20}$$

where we define R_{NSC} to be the 'non-smooth-circular' number. The larger the value of R_{NSC}, the less smooth-circular the droplet profile is. This allows the comparison of individual droplets before and after a freeze-thaw cycle, as well as providing collective information about how droplets are typically altered by a cyle and whether there is permanent change done to the droplets as a result of their interaction with the growing oil crystals.

5.3 Materials and Methods

5.3.1 Emulsion preparation

Emulsions were prepared as described in Chapter 3. To allow the study of individual droplets, the emulsions were diluted to increase the average distance between droplets. As the emulsions sediment, due to the mismatch in oil and water densities, a small amount of the dense emulsion from the bottom of the

emulsion vial was taken and diluted in pure nile red-dyed hexadecane at a weight fraction of 0.9%. The sample was then gently shaken by hand to disperse the droplets through the oil. Before transferring emulsion into a sample cuvette, the vial was gently shaken again to redisperse the sedimenting droplets evenly. Sample cuvettes were then placed into the temperature stage and frozen in the non-uniform setup as described in Chapter 3.

5.3.2 Sample charaterisation

Confocal microscopy was used to size the droplets imaged during freeze-thaw cycles. The droplets were generally chosen by eye using the eyepiece on the confocal microscope as any crumpling of droplets and proximity of neighbouring droplets was easily observed over a wide field of view. The droplets chosen were typically those which were initially close to spherical, unwrinkled droplets and were far enough from any other droplets that no interaction was expected during the process. This ensured that the behaviour observed was due to the interaction between the droplet and the growing crystals alone. Image analysis was then used to determine the other shape characteristics of the droplets.

5.3.3 Image analysis

In order to analyse droplets and extract the shape descriptors described in Section 5.2, an xyz-stack is imported into ImageJ and from there the particle fluorescence channel image in which the observed shell of particles is brightest and of maximal width is extracted. This is assumed to be the centre of the droplet to within the distance between slices in the z-direction (typically 3μm). The image is then thresholded by eye to leave only the ring of particles. If necessary, the 'Fill holes' tool is used to fill gaps in the thresholded edge and any remaining gaps are filled using the 'paintbrush' tool so that when 'Fill holes' is used again, the centre of the droplet becomes black. Then the outline of the droplet is extracted using the 'Find edges' tool. Finally, the 'Shape filter' tool was used to obtain values for Feret diameter and circularity. This process was carried out for droplets prior to freezing and after a single freeze-thaw cycle. Droplets which were broken up were not analysed after thaw. In a small number of cases, droplets were observed to split during the cycle and/or another droplet came into contact with the droplet of interest. These were also not analysed after thaw if the droplets were too close

to analyse individually or were not the same volume as the original droplet.

5.4 Results and Discussion

This section discusses confocal microscopy results of particle-stabilised emulsion droplets deforming as a result of the continuous phase undergoing a freeze-thaw cycle. At all points, the droplets remain liquid as the temperature of the sample remains far above the freezing temperature of water. The behaviour of droplets varies and is dependant both on the initial shape of the droplet as well as the shape and direction of oil crystal formation. Nevertheless, visual inspection of confocal images for individual droplets taken from 25 separate freeze-thaw cycles revealed trends which are discussed below.

5.4.1 Freezing

Figure 5.5 shows a time series of images of a single particle-stabilised emulsion droplet as the continuous phase freezes. The sample was cooled at a rate of 4 °C/min from 20 °C to 10 °C. Initially, the droplet is close to spherical and the oil is completely liquid, as shown in panel (a). As the oil freezes, crystals begin to appear in black, seen in (b)-(d). Many of the oil crystals are initially pointed, having a tip diameter smaller than the droplet diameter, meaning crystals only come into contact with part of the droplet at one time. In addition, several crystals can come into contact with the droplet either at the same time or with slight delays between them, as seen in panel (f).

The different directions of crystal growth relative to the droplet affect the way the droplet is distorted. A slight distortion is caused as the crystal to the left of the droplet widens towards the droplet (see panel (d)-(e)). Then the crystals which seem to penetrate the droplet in panel (f) broaden in panels (g)-(k) and stretch the droplet out until the other crystals grow around it and further distortion is halted as the droplet is encased in solid hexadecane.

Deformation of the droplet changes the surface coverage of particles because for a fixed volume, a sphere provides the minimum surface area, thus any deviation from that increases the surface area. This can be seen in Fig 5.5(j)-(k) (inset and arrows) as patches of bare interface begin to appear where the droplet is

stretched. This shows that the particle network on the surface has become unjammed and this will be important during thaw as the particles again rearrange on the interface.

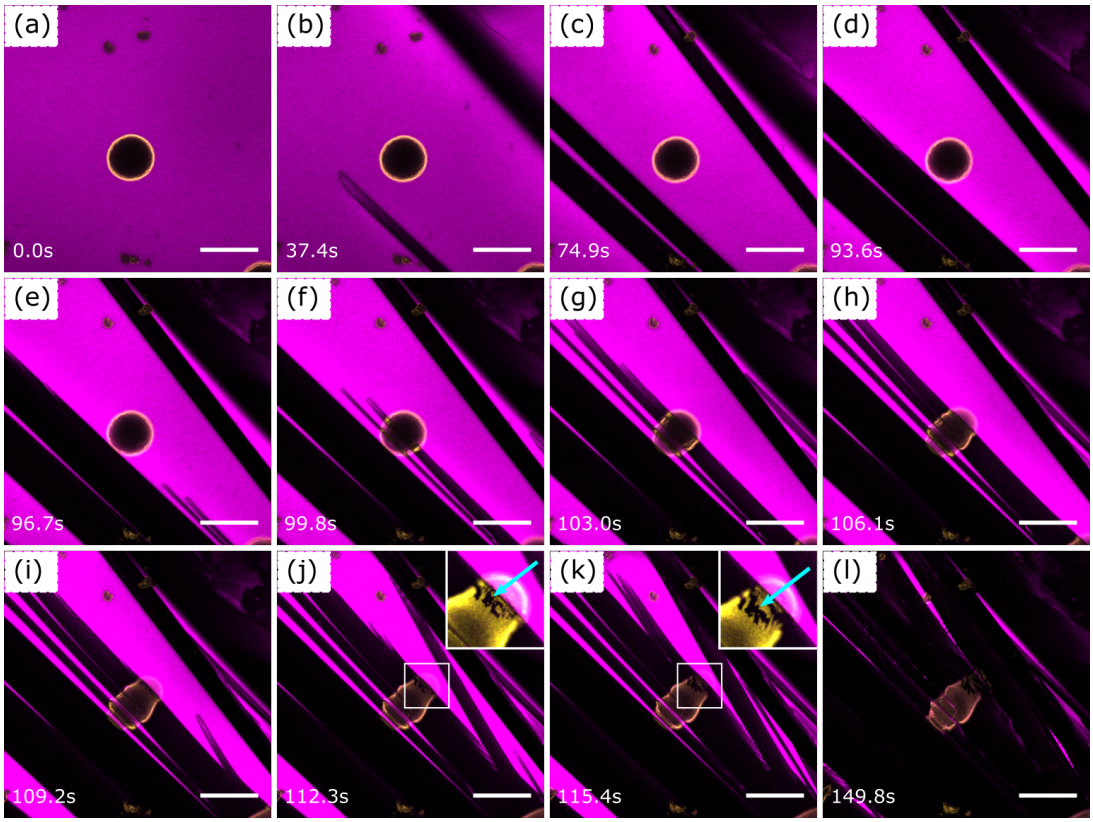

Figure 5.5 *Images of a PMMA(yellow)-stabilised water(black) droplet in oil(magenta) as the oil freezes at a rate of 4 °C/min. Images are taken at significant points during the crystal-droplet interaction and are timestamped with t=0 taken as the time the temperature ramp was started. (a) Initial unfrozen sample. (b)-(l) Oil crystallisation and droplet deformation due to the interaction between crystals and droplets. In (j)-(k) the inset images show the region in the white box and arrows point to the bare surface patches without particles. Scale bars: 100 μm.*

A second example is given in Fig 5.6. In this case the initial droplet appears wrinkled due to water evaporation from the droplets prior to the start of the experiment. As the oil crystals appear, one crystal grows through the edge of the droplet, trapping part of the droplet surface (Fig. 5.6(b)-(c)). The crystal then begins to broaden, and as it does so it progressively traps more of the droplet (Fig. 5.6(d)). More crystals grow into the region and eventually the droplet becomes completely encased in the frozen oil (Fig. 5.6(e)-(f)). As the droplet

becomes trapped by the crystal, the untrapped region of the droplet becomes less wrinkled. Comparing the droplet shape between Fig 5.6(c) and (d), it can be seen that the droplet surface in the trapped region is more crumpled than at the start, but in the untrapped region is smoothed out. The reason for this is that as the droplet is trapped, the particles on the interface unjam and are free to move. The surface to volume ratio of the untrapped droplet portion changes, meaning that there are fewer interfacial particles, allowing the untrapped region to return towards a spherical cap.

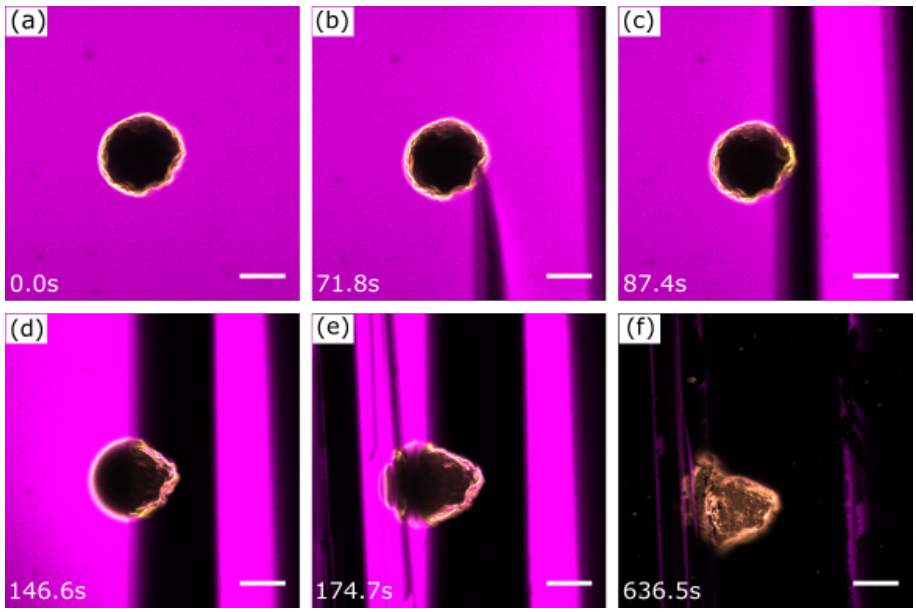

Figure 5.6 *Images of a PMMA-stabilised water droplet in oil as the oil freezes at a rate of 4 °C/min. Images are taken at significant points during the crystal-droplet interaction. Images are timestamped and t=0 corresponds to one frame (3.1s) before crystals appear in the field of view. Scale bars: 50 μm.*

In Chapter 4, simulations suggested that droplets would disrupt the fluid causing fluid flow at velocities of magnitude $\mathcal{O}(10^3)$ μm/s. It would be expected that in experiment this would cause droplets to move across the field of view as the oil cools, but this is not observed here. Rather, droplets barely move unless pushed by an ice crystal. There are several factors which can account for this difference. The first is that the droplets in the simulation are fixed and do not move, thus would be expected to disturb the flow more than droplets which are free to move. This could mean that the magnitude of the velocity is larger in simulation than in experiment. In addition, as discussed in Chapter 4, the droplets here are 1-2

orders of magnitude smaller than in the simulation and this would reduce the effect of the droplets on the fluid flow. As the density of the droplets is higher than that of the oil, the droplets are also likely to be found near the bottom of the cuvette. Although they are not expected to stick to the cuvette due to the coating applied to the glass, the different position of the droplets compared to the simulation would further alter the fluid flow observed in simulation. Thus in combination with the phase change and crystal growth which change the dynamics of the system, these factors can explain why the droplets did not move far during experiments and why the fluid velocity may be lower than observed in simulation. Any flow within the empty regions of fluid would be hard to detect in this setup using confocal microscopy and other techniques would be required to observe experimentally the velocity of any fluid flow here.

5.4.2 Thawing

As the oil thaws, the shape of a droplet undergoes further change as the particles trapped in the crystals are released. Droplets do not generally return to their original shape, even those which began close to spherical. Figure 5.7 shows several droplets with their initial pre-freeze shape and their final post-thaw shape to illustrate the typical behaviour of droplets after a single freeze-thaw cycle. Some droplets are broken, as shown in panel (a)-(b), during the freezing stage and this becomes clear upon thaw. Others return to slightly elongated droplets, shown in panels (c)-(d) or closer to spherical, as shown in panel (e)-(f). Droplets which began wrinkled do not return to the same wrinkled shape, although some are wrinkled afterwards, as shown in panels (g)-(h). In other cases, wrinkled droplets are smoother post-thaw than they were initially.

5.4.3 Shape analysis and particle jamming

Using the theoretical framework outlined in Section 5.2, the spread of droplet shapes pre-freeze and post-thaw can be analysed using the circularity, C, and ratio of minimum and maximum Feret diameters, F. Although it is possible for both stretching and buckling to occur on the same droplet, the amplitude of wrinkles on a stretched/elliptical droplet is small in comparison to the semi-major/minor axes, thus they are not directly considered in this analysis.

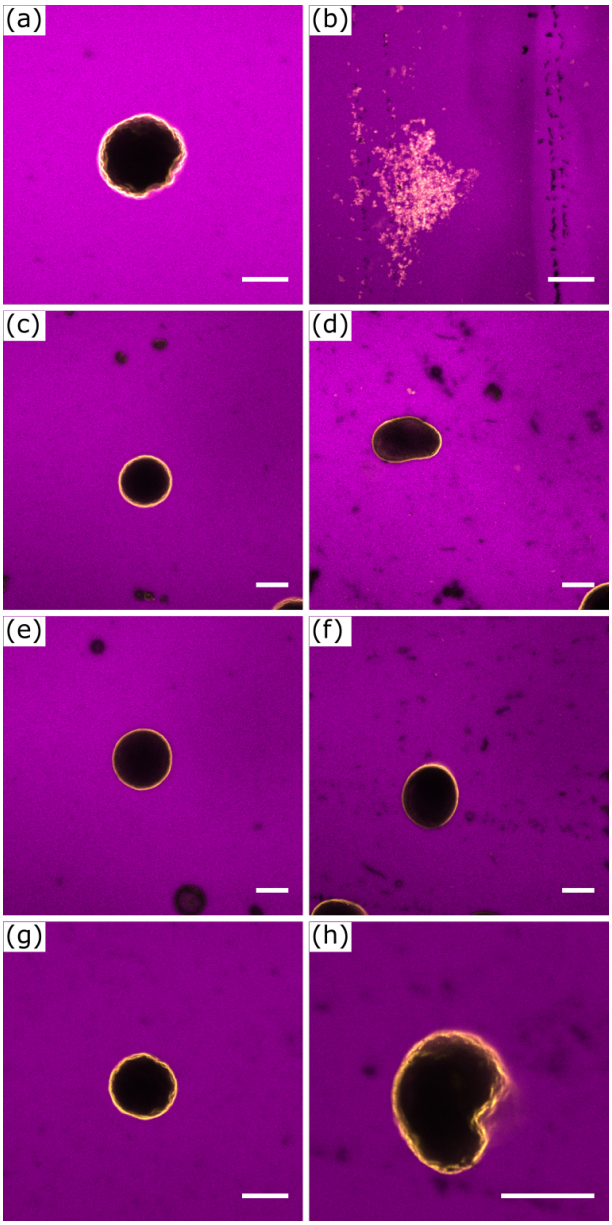

Figure 5.7 *Representative images of PMMA stabilised water droplets in oil pre-freeze (a, c, e, g) and post-thaw (b, d, f, h). (a-b) Droplet is pierced and split during freezing and so the water escapes on thaw. (c-d) Droplet is elongated by the freeze-thaw cycle. (e-f) Droplet is close to spherical, only slightly elongated. (g-h) Droplet begins wrinkled and finished both wrinkled and bean-shaped. Note the difference in magnification between (g) and (h) - scale bars represent the same length but the field of view in (h) is smaller. Scale bars: 50 µm.*

Fig. 5.8 shows experimental data points plotted in the F-C phase space, with initial droplets shown in (a) and droplets after a single freeze-thaw cycle shown in (b). The initial droplet points are much closer together than the final droplet points, as expected given droplets were mostly selected to be initially spherical. The final droplets are more spread out in the F-C phase space, as could be expected after the amount of distortion the droplets were subjected to by oil crystals. There are two main outliers in the initial droplet dataset, the corresponding droplet images of which are inset. As can be seen from the images, these droplets are clearly non-spherical before freeze-thaw cycling. The droplet at the lower circularity was broken during freeze-thaw cycling so is not included in the results of panel (b), and the droplet at the higher circularity is marked in blue in panel (b), showing it to be within the range of results of the more spherical initial droplets.

Within the final droplet results, the points are much closer to the 'ideal circle' than suggested in the theoretical considerations of Fig. 5.3. This is because in the wrinkled droplets, the amplitude of the wrinkles is very small in comparison to the droplet radius, so the extra perimeter they add is minimal, thus the circularity is closer to 1 than previously suggested. In the oval droplets, the ratio of semimajor to semiminor axes was low due to droplet recovery during thaw. The droplets return towards spherical until the particles jam, thus also here on the whole the droplets have a high circularity and Feret ratio. Due to errors in image processing and analysis, some of the droplets appear to have a higher circularity than 1 which is unphysical. Small errors in perimeter or area calculation by ImageJ are the reason for this.

Using the values calculated in Section 5.2.3, the average R_{NSC} for droplets before and after freezing is determined. As explained earlier, droplets which were broken during the freeze-thaw cycle were not included in the post-thaw data. The results are given in Table 5.1. From these it can be seen that R_{NSC} increases as a result of freeze-thaw cycles as does the spread of values, seen in the larger standard error on the mean. This shows that the net result of freeze-thaw cycles is to deform droplets. Observing that the average value for F for initial and final droplets decreases shows that the deformation at least partly takes the form of stretch or elongation.

For initially wrinkled droplets, it can be seen that, assuming no loss of particles, there are too many particles on the droplet interface to allow the droplet to be spherical as a sphere has the minimal surface-to-volume ratio. As the oil thaws

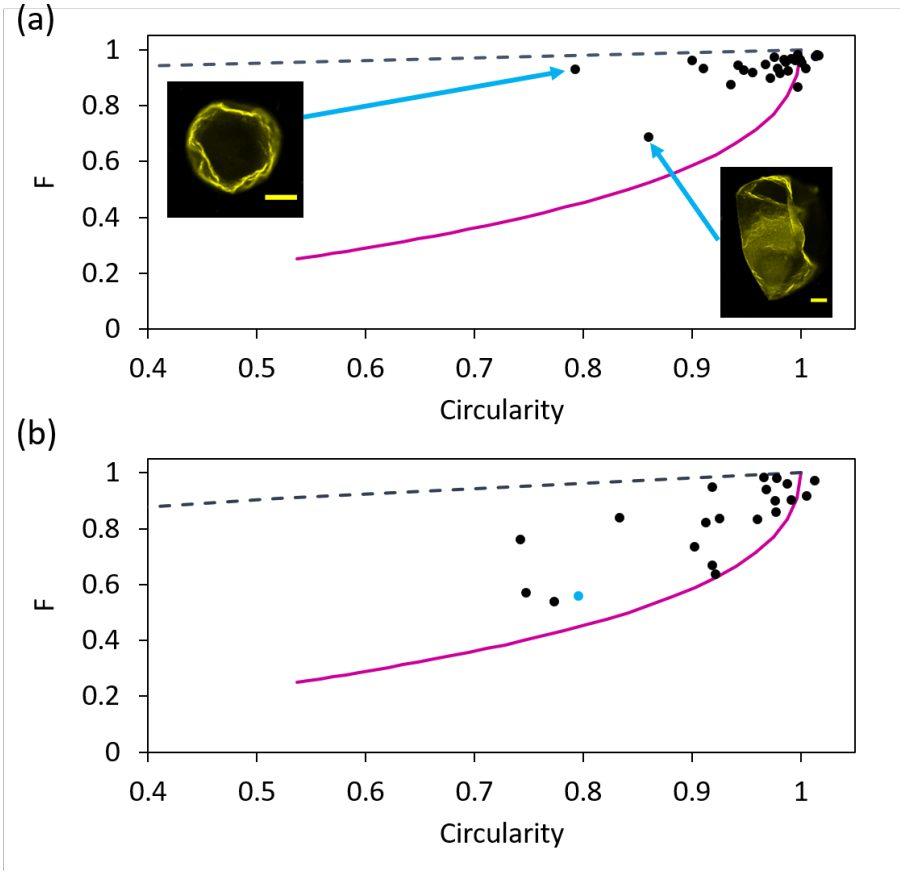

Figure 5.8 *Droplet shapes plotted in F-C phase space for (a) initial droplets and (b) droplets after a single freeze-thaw cycle. The dashed dark blue curve represents the 'wrinkled droplet' model and the solid magenta curve represents the 'ideal ellipse' predicted in Section 5.2.3. Images of the droplets corresponding to the two outlying data points are inset.*

and the droplet relaxes, the most energy effective shape change to make is to relax towards a sphere until the particles are jammed. There is no force to cause the droplet to buckle during this process, thus they are more likely to be elliptical than wrinkled, particularly in cases where the wrinkles have been smoothed out during the freeze part of the cycle.

For droplets initially close to spherical, the elongation can be explained by the rejamming of particles at a lower surface fraction than in the initial droplets. It has been shown by van Hooghten *et al* that on successive expansion-compression cycles of a particle-laden interface in a Langmuir trough, the interfacial area at which the surface pressure increases sharply, *i.e.* the area at which the

	R_{NSC}	F_{average}	C_{average}
Initial droplets	0.09(2)	0.93(1)	0.97(1)
Final droplets	0.28(6)	0.82(3)	0.91(2)

Table 5.1 *Table of Non-smooth-circular values, circularity and Feret ratio values for initial and final droplets. Uncertainties given as standard error on the mean*

particles are jammed, decreases [51]. This suggests that after a single expansion-compression cycle, the particles are jammed at a lower packing fraction than after further cycles.

During emulsion formation, the 3-component system is shaken vigorously using the vortex mixer, allowing the particles to attach to droplet interfaces. Droplets form via limited coalescence, thus particles reach (close to) maximal packing on the surface [36]. During the freezing phase of a cycle, the droplet surface is stretched, comparable to an expansion cycle on a Langmuir trough, breaking up the particle formation on the surface and allowing the particles to move and rearrange. Upon thaw, the droplet is gently allowed to relax in a less energetic process than emulsification and the particles again rearrange but may jam at a lower packing fraction than on the initial droplet.

As these results show that freeze-thaw cycling has the capability of deforming particle-stabilised droplets due to the droplet-crystal interaction, this reinforces the conclusions of Chapter 4 that crystal growth, and therefore temperature profile, in the sample is important in determining the behaviour of a sample. The results in this chapter show that the direction of crystal growth affects the deformation, and in some cases break-up, of the droplet and this may ultimately also affect the post-thaw droplet shape. This suggests that controlling the direction of crystal growth may control the droplet deformation, a hypothesis which will be studied in Chapter 6.

These results also agree with previous studies discussed in Section 5.1 in the deformation of particle-stabilised droplets which show the importance of the interfacial particles in determining the droplet structure [133]. Droplets which buckle when confined during freezing show similar structural behaviour to buckled droplets upon inner phase extraction, as is expected for a droplet with a solid interface [131, 150].

In this case, the emulsion droplets are separated such that they do not interact,

but in a less dilute emulsion, not only is there crystal-droplet interaction but it is possible there will also be droplet-droplet interactions. The stretching of droplets observed here leads to bare regions on the droplet interface as the increased surface area cannot fully be covered with a fixed number of particles. Particle coated droplets have previously been shown to partially coalesce in the case where bare patches come into contact [141, 151] and thus two single, deformed droplets brought into contact have the potential to partially coalesce, damaging the emulsion structure. This effect will be studied in Chapter 7

5.5 Conclusions and future work

Particle-stabilised droplets were imaged using confocal microscopy and observed to deform when interacting with a freezing continuous phase. Two forms of deformation have been discussed: buckling (wrinkling), of the droplet surface and elongation of the droplet. As the continuous phase freezes,the crystals which form interact with the droplet, trapping the droplet first only partially, then progressively more as the crystals grow. As the crystals grow and interact with the droplet, the droplet deforms, allowing smoothing of the untrapped interface. Upon thaw, droplets make a partial recovery but do not always recover their original, spherical shape.

Droplet profiles have been characterised in 2D via a combination of circularity and Feret diameters and this analysis has shown that droplets become less smooth-circular and more elongated as a result of freeze-thaw cycles. The droplet behaviour can be explained by the particles jamming, unjamming and re-jamming on the droplet interface at different packing fractions.

It would be interesting in future work to study the effect of the relative droplet and crystal sizes on the interaction between droplet and crystal. This could take two routes: firstly one could consider whether droplets with a much larger radius are more easily deformable than much smaller droplets. Secondly one could consider whether crystals with much wider tips interact differently with the droplets, perhaps having a greater tendency to push rather than skewer the droplets.

Having shown that particle jamming on the interface is important in determining droplet behaviour, it would also be interesting to explore the particle coverage

effects on droplet behaviour at a single-particle level. Lower initial particle coverage for example could lead to the droplets being more easily deformable, particularly if coverage was low enough that the shell on the droplet is no longer rigid. As mentioned in Section 5.1, excess particles in the continuous phase have been shown to trap non-equilibrium structures and it could be interesting here to add excess particles into the non-freezing droplet phase to see whether they would adsorb to any bare interface produced during droplet deformation.

Chapter 6

Directional freezing of dilute particle-stabilised emulsions

6.1 Introduction

In Chapter 5, the behaviour of droplets interacting with oil crystals was studied, including the deformation and breakup caused by those interactions, as well as the resultant shape changes. Due to the nature of the setup used, a controlled solidification front was not achieved in those experiments, so now an alternative setup is considered. Here a solidification front moving towards the droplets from one direction is achieved. This will allow further investigation into the interaction between the crystal growth and the particle-stabilised droplets with a higher level of control over that interaction by setting the direction of crystal growth rather than allowing crystallisation from all directions. It also shows the behaviour of particle-stabilised emulsions undergoing a process used in materials processing because of the increased level of control over the freezing parameters such as temperature gradient and velocity of the freezing front [121, 152]. This interaction has been widely studied in the case of solid particles and has also been studied in the case of surfactant-stabilised emulsions [153] but has not been studied with particle-stabilised droplets.

In this chapter the behaviour of emulsions in the 'cryoconfocal' [107] setup in the Ceramic Synthesis and Functionalization Laboratory (LSFC) is explored with the assistance of the group of Sylvain Deville. This setup is comprised of a

translational directional freezing mechanism attached to a confocal microscope which allows fluorescence imaging during freezing [107]. The behaviour of particle-stabilised emulsion droplets interacting with a hexadecane solidification front is studied and observations are made on the effects of temperature gradient and sample velocity on the droplet behaviour. The effects of the stabilising particles and their interaction with the front are also explored. The interaction is imaged in 4 dimensions (xyzt), allowing observation of the movement of particles on the droplet interface as a droplet is trapped by the freezing front.The droplet behaviour is compared to that observed in Chapter 5 where the freezing was multi-directional and the interaction was mostly between individual crystals and droplets rather than between a droplet and a solidification front.

6.1.1 Directional freezing

Assuming freezing to occur by a front moving through the sample, the front can interact with the object in a number of different ways: the object can be immediately trapped with the front growing directly around the object; the object can be pushed by the growing front into still-liquid regions until there is no more available space for the droplet to move into; or a combination of the two can occur, where the droplet is pushed and then completely trapped [154].

Freezing via a solidification front is an example of directional freezing, a technique used in a range of applications such as creating porous materials [155], rejecting impurities from materials [156] and producing aligned structures such as fibres [116, 157]. During directional freezing, a temperature gradient is applied across a sample, with the lowest temperature below the sample freezing temperature. This causes crystals to grow from one end of the sample to the other [158, 159]. In this way, impurities such as particles or droplets can be rejected in-between the ice crystals, leading to aligned structures, or rejected ahead of the front, leading to compressed structures such as foams [160].

Directional freezing can be achieved either in a static setup or a translational setup. In the static case, the temperature at one end of the sample is lowered below the sample freezing temperature, and the freezing front then propagates through the sample [161]. In the translational case, a stage is used to draw samples from a higher temperature environment into a lower temperature environment, providing control over the position of the solidification front [107, 162, 163]. This could be considered as a small-scale, single-sample

'conveyor belt' mechanism. On a much larger scale, conveyor belt technology is widely used in the food industry [164] for transport and treatment of products and it is also used in industrial freezing processes [165, 166]. This makes directional freezing via sample translation a useful process to study, even on a much smaller scale, as it can provide insight into the larger-scale behaviour occuring during production.

In some applications, directional freezing may also be combined with other techniques such as freeze-drying in which the frozen solvent is removed via sublimation, leaving only the templated structure [167]. Tuning the particle/droplet size and the crystal growth is important in achieving the desired final morphology with *e.g* the correct pore size [116, 168, 169]. While in many applications rejection of the impurities was required to obtain the templated structures, in other applications, such as food products, it is vital to the integrity of the product texture and stability that the 'impurities,' *i.e.* emulsion droplets, are engulfed rather than rejected so that upon thaw the product regains its original state. Mass rejection of droplets during solidification could cause droplet aggregation or separation from the bulk, both of which would destabilise the emulsion [170].

Having observed in Chapter 5 that non-directional freezing causes droplets to deform, and that droplets deform in the direction of crystal growth, it could be expected that directional freezing may cause droplet deformation only in the direction of the front growth. In addition, freezing via a planar solidification front removes the narrow crystal tips which in Chapter 5 were seen to pierce droplets, thus this form of damage may be prevented. It has been shown for surfactant-stabilised droplets that a moving front can trap the droplets without droplet deformation [153], but the same has not been probed for particle-stabilised droplets.

6.2 Theory of engulfment in a solidification front

An object, such as a particle or a droplet, approaching a solidification front can be either engulfed or pushed by the front. For particle-stabilised emulsion droplets, the first contact point between a droplet and the solidification front will be one of the stabilising particles, thus it is possible that the trapping of the droplet begins with the trapping of a particle. Alternatively, it is also possible that the droplet itself is engulfed as a whole with the particles not interacting individually with

the solidification front.

The key factor determining whether or not a particle will be engulfed is whether or not the front velocity is higher than the critical velocity. There are two main theories which have been used to describe this behaviour. As the application of these theories to a particle-stabilised emulsion droplet is non-trivial, both will be presented here and further discussed in Section 6.5.

6.2.1 Simple force balance

Following the theory presented by Uhlmann et al [171], the critical velocity for engulfment can be determined using a simple model which considers a force balance at the interface [116, 171, 172].

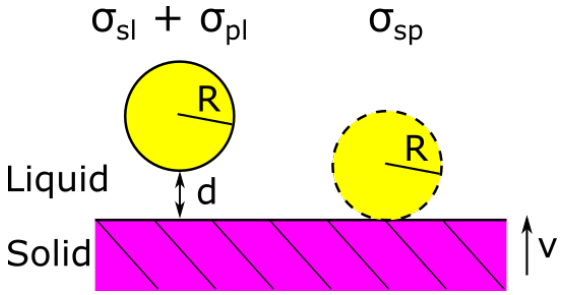

Figure 6.1 *Particles (yellow) in a liquid with a solidification front(purple) approaching at velocity v. Before contact (left particle), the surface energy is a sum of the solid-liquid and liquid-particle surface energies. As a particle makes contact (right particle), the surface energy in the contact region is given by the solid-particle energy.*

Consider a particle approaching the solid-liquid interface, as shown in Fig. 6.1. There is a viscous drag force on the particle which is attractive (towards the interface) as the particle tries to move away from the interface, given by

$$F_{\text{viscous}} = \frac{6\pi\eta v R^2}{d} \ , \tag{6.1}$$

for a spherical particle at a flat interface [171], where η is the liquid viscosity, v the velocity of the solidification front, R the radius of the particle and d the distance between the particle and the front.

This is opposed by a disjoining force, related to the interfacial free energy (in units of [N/m]) between each of the interfaces. Before contact is made, the surface energy in the contact region is a sum of the particle-liquid surface energy, σ_{pl}, and the solidification front-liquid surface energy, σ_{sl}. Upon contact, the surface energy is given by σ_{ps}, the surface energy between the solid interface and the particle. A particle will only be engulfed if the difference in free energies, $\Delta\sigma_0$, is less than zero, *i.e.*

$$\Delta\sigma_0 = \sigma_{\mathrm{ps}} - (\sigma_{\mathrm{sl}} + \sigma_{\mathrm{pl}}) < 0 \ . \tag{6.2}$$

The corresponding surface force, F_{surface}, is therefore repulsive and is given by

$$F_{\mathrm{surface}} = 2\pi R \Delta\sigma_0 \left(\frac{a_0}{d}\right)^n \ . \tag{6.3}$$

The $(\frac{a_0}{d})^n$ term is used to account for a thin film of fluid between the particle and the solid boundary, where a_0 is the average intermolecular distance in the film and n a constant whose value is taken to be in the range 1-5 [172].

Equating the surface and viscous forces leads to an expression for the critical velocity, v_{c}, required for a particle to be engulfed:

$$v_{\mathrm{c}} = \frac{\Delta\sigma_0 d}{3\eta R} \left(\frac{a_0}{d}\right)^n \ . \tag{6.4}$$

Although the values for $\Delta\sigma_0$ and n are difficult to obtain/estimate for the systems used in this thesis, it can be seen that the critical velocity is inversely proportional to the particle radius, meaning larger particles are engulfed at a lower front velocity.

6.2.2 Force balance with a wetting layer

The theory presented in Section 6.2.1 considers only a thin film between particle and interface through the term $(\frac{a_0}{d})^n$ which is difficult to estimate correctly due to the factor n. However, there may in reality be a complete wetting layer between the particle and solid front. To account for this, we follow the derivation of Worster and Wettlaufer. Only the main details of this derivation are included, a more in-depth derivation can be found in References 173 and 174.

As a particle approaches a solidification front, interfacial premelting causes the interface to locally deviate from planar, as shown in Fig. 6.2(a). Two forces are present in this situation, the van der Waals repulsion directed away from

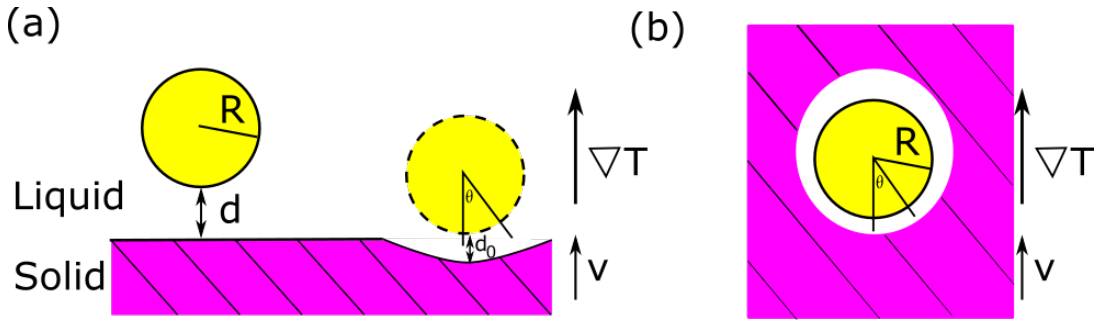

Figure 6.2 *(a)Particles (yellow) in a liquid with a solidification front(purple) approaching at velocity v. The interface deviates from planar as the particle approaches. (b) Particle is engulfed in solid and surrounded by a premelted layer of liquid.*

the interface and the the viscous force directed towards the interface. Above the critical velocity, the viscous force dominates and the particle is engulfed by the interface while below the critical velocity the van der Waals force dominates and the particle is rejected. The particle does not come into direct contact with the frozen continuous phase in either case because there is a thermomolecular pressure which is a result of the preferential wetting of the particle by the liquid continuous phase rather than the solid. Thus when a particle is engulfed, it is surrounded by a premelted layer, as shown in Fig. 6.2(b).

Engulfed particle

Assuming a spherical particle of radius R, the thermomolecular pressure, due to van der Waals forces, is given by the equation

$$P_T = -\frac{A}{6\pi d^3} \ , \tag{6.5}$$

where A is the Hamaker constant and d the thickness of the premelted film.

The equilibrium film thickness, d, is given by

$$d = \lambda \left(\frac{T_m - T}{T_m} \right)^{-\frac{1}{3}} \ , \tag{6.6}$$

which for a sphere encased in a solid, can be expressed as

$$d = \lambda T_m^{-\frac{1}{3}} (T_m - T_0 + \nabla T R \; cos \; \theta)^{-\frac{1}{3}} \; , \tag{6.7}$$

where θ is the polar angle measured as shown in Fig 6.2(b), T_m the melting temperature of the continuous phase, T_0 the temperature at the centre of the sphere and $\lambda^3 = A/(6\pi\rho_s L_m)$ with ρ_s the density of the solid and L_m the latent heat of melting.

By substituting Equation 6.7 into Equation 6.5 and integrating over the surface of the particle, the disjoining force can be obtained. This is given by

$$F_T = \frac{4\pi R^3}{3} \frac{\rho_s L_m}{T_m} \; \nabla T. \tag{6.8}$$

Using lubrication theory, the viscous/lubrication force on the sphere is given by

$$F_\eta = -\frac{4\pi R^3}{3} \frac{6\eta R v}{\lambda^3} \left(\frac{T_m - T_0}{T_m} \right) \; , \tag{6.9}$$

where η is the fluid viscosity and v the velocity of the moving front.

Rejected particle

When above the critical velocity, the interface near a particle will be distorted from planar and will curve and this will affect the forces acting locally. There is a characteristic lengthscale, l, which is the film thickness between the front of the particle ($\theta = 0$) and the solid interface when the temperature at that point is equal to T_m and this is given by the expression

$$l^4 = \frac{\lambda^3 T_m}{\nabla T} \; . \tag{6.10}$$

Both the thermomolecular and viscous forces are dominated by the region close to $\theta = 0$ and this leads to an approximate expression for the film thickness

$$d \approx d_0 + \frac{\frac{1}{2} R \theta^2}{1 + \frac{3l^4}{d_0^4}} \text{ for } \theta << 1 \; , \tag{6.11}$$

where d_0 is the minimum film thickness at $\theta = 0$. Using this approximation and integrating P_T under these new conditions gives the thermomolecular force as

$$F_T = \lambda^3 L_m \rho_s \frac{\pi R}{d_0^2} \left(1 + \frac{3l^4}{d_0^4}\right) \ . \tag{6.12}$$

The viscous force is expressed as

$$F_\eta = -\frac{6\pi\eta R^2 v}{d_0} \left(1 + \frac{3l^4}{d_0^4}\right) \ , \tag{6.13}$$

The net force on the particle is zero, meaning the sum of these two forces must also be zero. From there, an equation for the front velocity can be obtained

$$v = \frac{\lambda^3 L_m \rho_s}{6\eta R d_0} \frac{1}{\left(1 + \frac{3l^4}{d_0^4}\right)} \ . \tag{6.14}$$

Differentiating with respect to d_0 and setting equal to zero gives the minimum film thickness before engulfment as $d_0 = \sqrt{3}l$ and thus the critical velocity

$$v_c = \frac{\lambda^{\frac{9}{4}} L_m \rho_s}{8\sqrt{3}\eta} \frac{1}{R} \frac{\nabla T^{\frac{1}{4}}}{T_m^{\frac{1}{4}}} \ . \tag{6.15}$$

As with the first theory presented, it can be seen that the critical velocity is inversely proportional to the particle radius, meaning larger particles are engulfed at a lower front velocity, and proportional to the temperature gradient, meaning the larger the temperature gradient, the higher the critical velocity.

Neither theory takes into account the effect of the solute (Nile red) as although this has the potential to affect droplet dynamics at the interface [153], it is unclear how to include this effect into either model.

Both theories show that the behaviour of the emulsion can be controlled by altering the velocity of the moving front and that it may be possible to control the emulsion structure in this way. This would mean that working at velocities below the critical velocity could cause all the droplets to move ahead of the front, being forced together towards the wall of the sample chamber and destroying the emulsion structure. In contrast working at velocities far above the critical velocity could lead to the droplets being engulfed which could reduce the damage to the emulsion structure. In addition, controlling the droplet size would equally

alter the critical velocity and this could also be used as a control parameter for limiting structural damage by creating larger droplets which then require a lower critical velocity for engulfment.

6.3 Materials and Methods

6.3.1 Emulsion preparation

PMMA-stabilised water-in-hexadecane emulsions were prepared as described in Chapter 3 but due to equipment contraints, emulsions were prepared by hand-shaking rather than by vortex mixing. This caused there to be some excess particles left at the bottom of the vial because the shaking was not as vigorous by hand as with the vortex mixer. Emulsions were diluted as described in Chapter 5 and although some of the excess particles were present in the dilute emulsion, they did not appear to affect the sample behaviour once in the temperature stage as the amount of excess particles in the vicinity of any given droplet was low.

6.3.2 Sample preparation

The temperature stage used in these experiments requires a small Hele-Shaw cell to be used, a schematic of which is shown in Fig. 6.3. The sample is contained in an approximately 100 μm thick layer between two glass slides (Menzel-Gläser, 24 $\times$ 60mm #1) spaced with double-sided tape of thickness 100 μm. As the hexadecane wets the tape, causing it to detatch and the sample to leak, a layer of grease (Apiezon) was added along the inner edge of the tape to act as a barrier, ensuring the tape and hexadecane do not come into contact. At one end of the cell, a plastic holder is included to allow the sample to be attached to the stage. The sample cell is filled using an Eppendorf pipette tip and the sample is drawn into the cell via capillary forces until the cell is full. The end of the pipette tip is cut off to enlarge the end and ensure the emulsion is not damaged when drawn into the pipette. This method typically led to a small air bubble becoming trapped at the sealed end of the sample by the emulsion during filling which was not easily removed, but the sample was typically imaged far from the bubble so effects of the bubble were not observed. The cell is then sealed at the open end using nail polish.

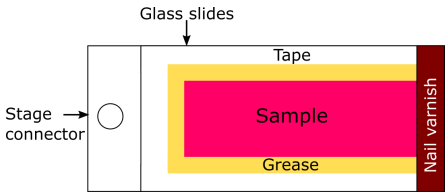

Figure 6.3 *Schematic of the sample cell used for experiments as viewed from above. The plastic attachment at the left hand end allows the sample to be attached to the stage.*

6.3.3 Temperature stage

A custom-built temperature stage is used here, attached to a Leica SP8 confocal and is shown in Fig. 6.4. The sample is placed onto the temperature stage attached to the confocal microscope and held in place with a magnetic frame. The sample is imaged from above using a $20\times/0.7$ NA objective. The temperature stage is composed of two peltiers, one warm and one cold, with a temperature gradient between them controlled by the temperatures of the peltiers. The temperatures are tuned such that the freezing temperature of the sample occurs in the viewing region of the sample. The sample is pulled along the temperature gradient using a computer-controlled piezoelectric stage and as the sample moves toward the cold peltier, the solidification front moves with the same velocity in the opposite direction, thus the solidification front remains in the field of view of the objective.

Once the sample begins to freeze, the solidification front is initially non-planar, but given time to equilibrate, a planar front should be achieved. In this case, the front should be completely flat, with no crystals growing out of the front, allowing the study of the interaction between droplets and a planar solidification front.

6.4 Results

Here the results of dilute emulsions undergoing freeze-thaw cycles in the cryoconfocal setup are discussed. Eight separate samples were subjected to freeze-thaw cycles in total, with multiple droplets imaged per cycle and various

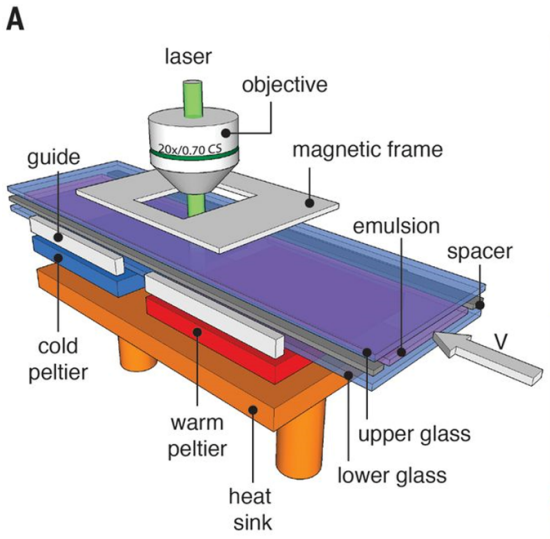

Figure 6.4 *Temperature stage for translational sample freezing. The emulsion sample is filled, as shown, between two (sealed) glass slides and moved between the warm and cold peltiers. The peltier temperatures are set such that the sample is at its melting temperature in the region below the objective. Image used with permission from Reference 153*

temperature gradients and sample velocities tested. These results concentrate primarily on the freezing phase of a freeze-thaw cycle as it is difficult to track the same droplets through a complete cycle due to the movement of the sample. Thus the deformation and recovery of specific droplets is difficult to observe and only general behaviour can be observed.

6.4.1 Droplet trapping

Figure 6.5 shows an example of a droplet progressively trapped over time. Droplets appear black surrounded by a yellow ring from the particle fluorescence. Liquid oil is magenta and frozen oil is black. It should be noted that the solidification front does not appear planar in any of the images. This is a result of the solid-liquid interface structure and the experimental conditions and is discussed in more detail in Appendix A.

In Figure 6.5 (a) the droplet labelled '1' is viewed just before it begins to interact with the hexadecane crystals, then in (b)-(f) the droplet is progressively trapped

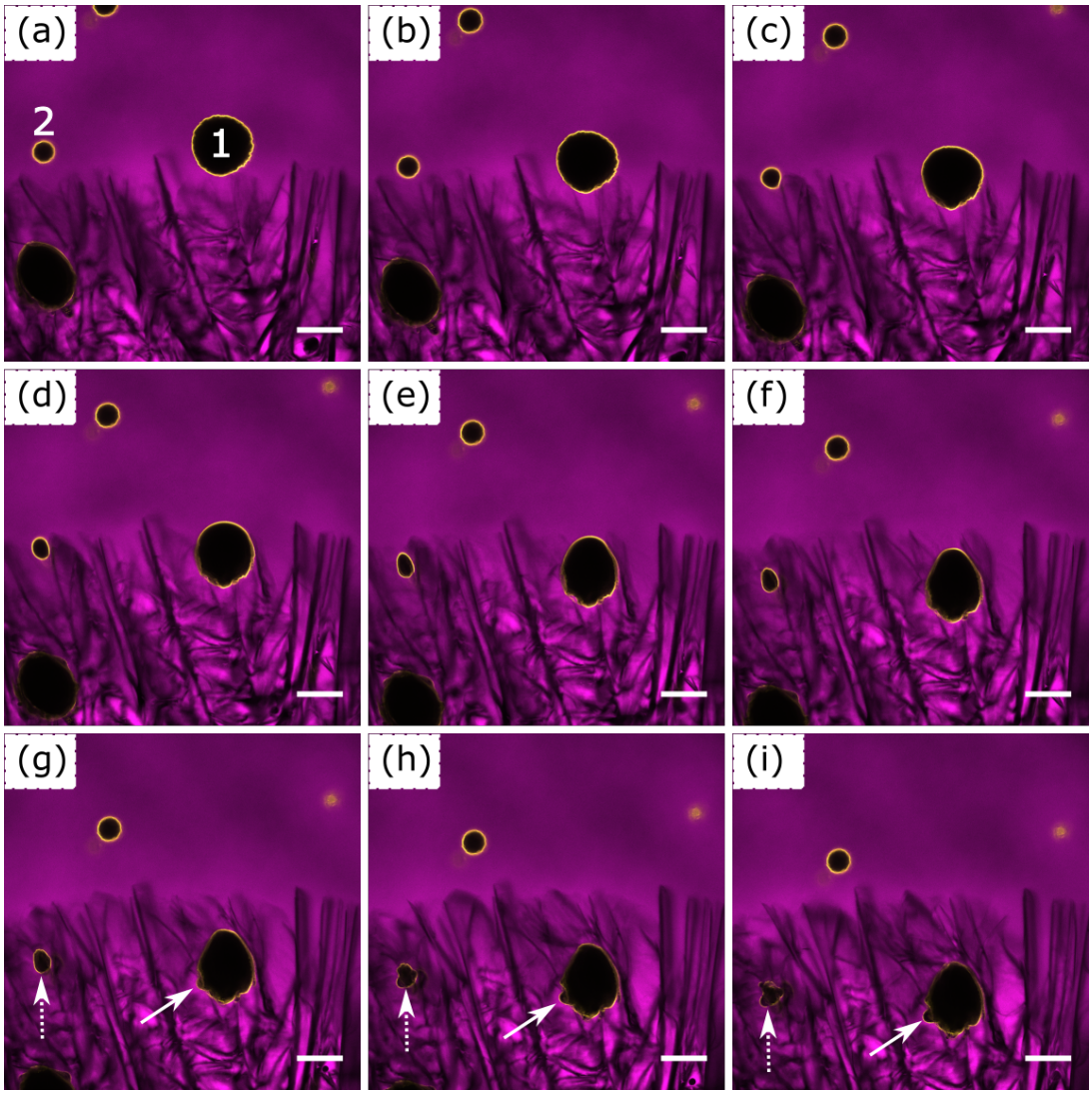

Figure 6.5 *Particle(yellow)-stabilised droplets in liquid oil (magenta) approaching and interacting with a hexadecane solidification front. The droplets are first stretched a small amount as they are engulfed by the front, then due to the gaps in the crystalline hexadecane, there is further droplet deformation (white arrows). Images are spaced 6.8s apart. Front velocity 5 µm/s, temperature gradient 15 °C/mm (Peltiers set to 32 °C and 2 °C). Scale bars: 100* µm

and slightly stretched in the direction of the front velocity. In panels (g)-(i) the droplet is encased in the crystalline hexadecane, but as the crystals are not a solid block and instead contain gaps, there is some further deformation of the droplet as the front moves (see solid white arrows). The same behaviour can be seen for droplet 2 which stretches in panels (b)-(f) and then further deforms in panels (g)-(i) (see dashed white arrows).

Figure 6.6 shows two alternative droplet behaviours. Note that droplet 1 has an incomplete particle layer, seen in the lack of fluorescence in the particle(yellow) channel around the edge of the droplet. This droplet is pushed by the front and is not trapped. There is also rotation either of the droplet itself or of the particles on the droplet surface, seen by the change in particle signal around the edge of the droplet between panels (a) and (d). In panels (c)-(f) droplet 2 is partially trapped by the hexadecane crystals, and the trapped region is stretched and deformed while the rest of the droplet remains free. In panel (g) the trapped region begins to widen and as the solidification front continues to move, the droplet is progressively stretched and trapped until the whole droplet is trapped, seen in panel (l).

6.4.2 Droplet trapping in 4d

By using the confocal microscope in 'resonant mode', 4D data could be taken, *i.e.* (x,y,z,t) as opposed to (x,y,t). This allowed larger portions of the droplet interaction with the freezing front to be observed, rather than just one plane. Due to equipment constraints, these results are taken from a single sample, thus all the droplet images presented here are taken from separate time frames within the same freeze-thaw measurement.

Figure 6.7 shows a time series of images of a droplet interacting with the solidification front. The upper half of the droplet is completely visible (images shown with gravity pointing upwards) but the oil fluorescence is omitted for clarity. In panel (a), the droplet has been partially trapped by the oil crystals, but the rest of the droplet is free. As the solidification front moves, the droplet is increasingly stretched in the trapped region, seen in panels (b)-(c). As a result of this, the particle shell on the droplet begins to break up and gaps appear, seen in panels (d)-(g) by the black gaps in the yellow shell. In panels (h)-(i), a portion of the droplet is detached and remains trapped in the solid hexadecane (disappearing from the field of view), while the rest of the droplet has become

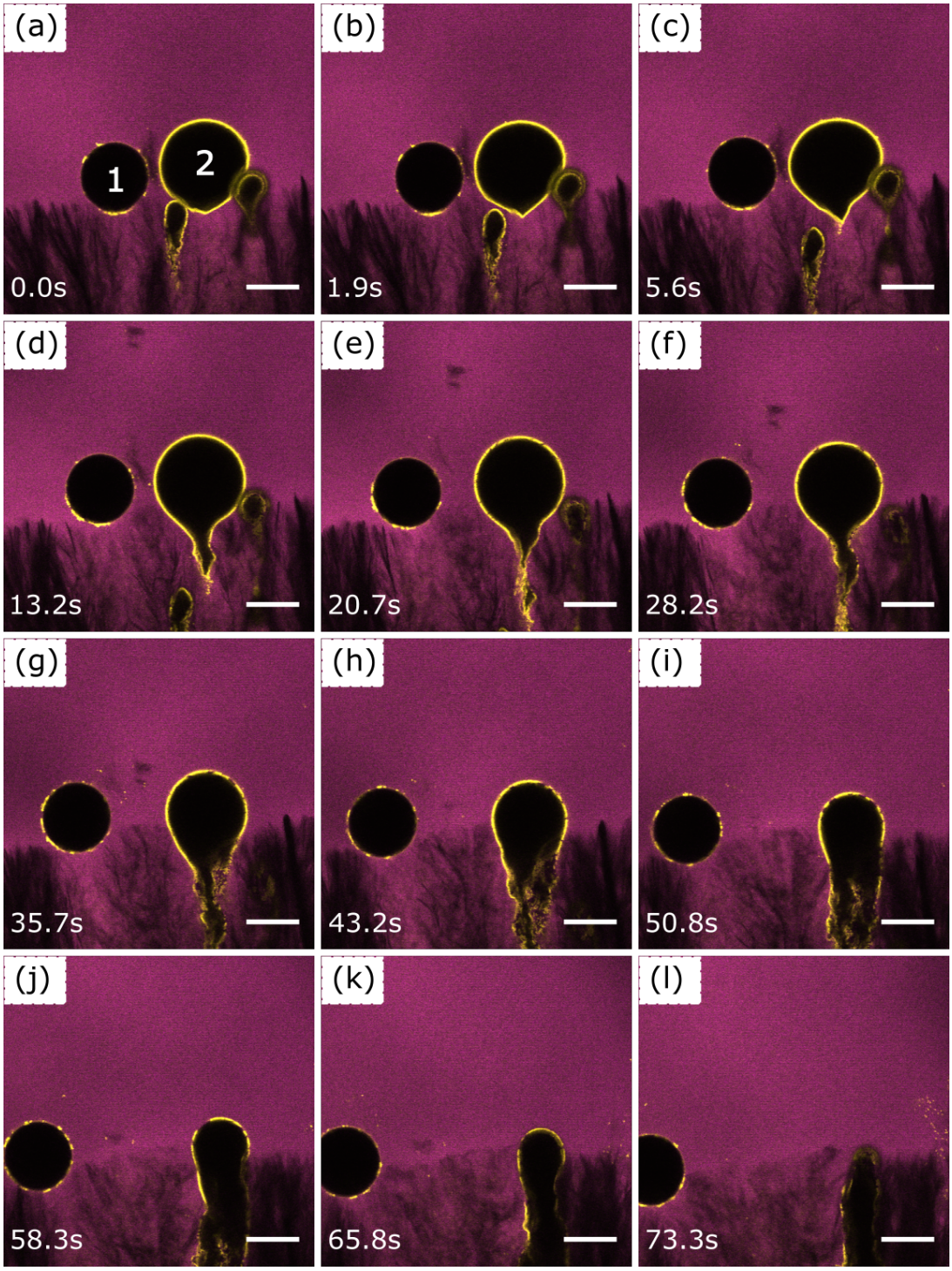

Figure 6.6 *Second example of particle(yellow)-stabilised droplets in liquid oil (magenta) approaching and interacting with a hexadecane solidification front. Droplet number 1 is only partially coated by particles and moves ahead of the front rather than being trapped. Droplet number 2 is progressively trapped by the front and deformed during the process. Images taken at times as shown, where t=0 is taken as the time the first image was taken. Front velocity 5 $\mu m/s$, temperature gradient 15 $^\circ C/mm$ (Peltiers set to 32 $^\circ C$ and 28 $^\circ C$). Scale bars: 50 μm*

completely free to move. The droplet now contains a slightly lower volume and is stabilised by a lower surface coverage of particles but it remains stable, at least for the length of time the droplet remained untrapped. This process has been observed to occur multiple times with the same droplet, each time leaving the droplet with a lower coverage of particles and a smaller droplet volume.

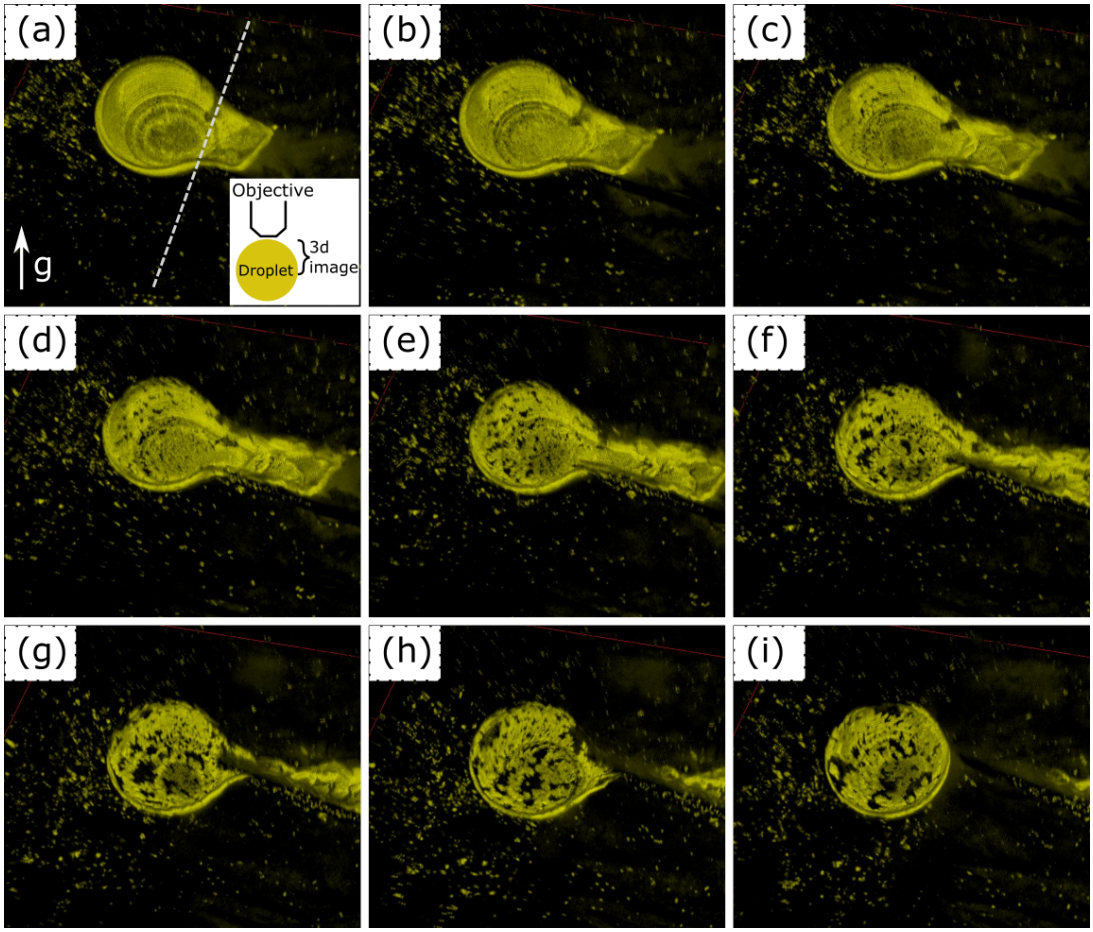

Figure 6.7 *Droplet interacting with solidification front in 3d over time. The 3d image is reconstructed from an xyzt stack of the particle channel fluorescence using the '3D Viewer' plugin in ImageJ. The upper half of the droplet is shown, with gravity acting in the direction shown by the arrow in panel (a). (a) Dashed line shows location of the solidification front. Inset: schematic of the objective position relative to the droplet and the portion of droplet imaged. Images spaced 2.0 s apart. Droplet size* $\sim$ *75* μm.

6.4.3 Droplet release from a thawing front

Although it was not possible to track droplets through the whole freeze-thaw cycle, it was possible to observe the behaviour of some droplets as the sample thawed and the droplets were released from the crystal matrix.

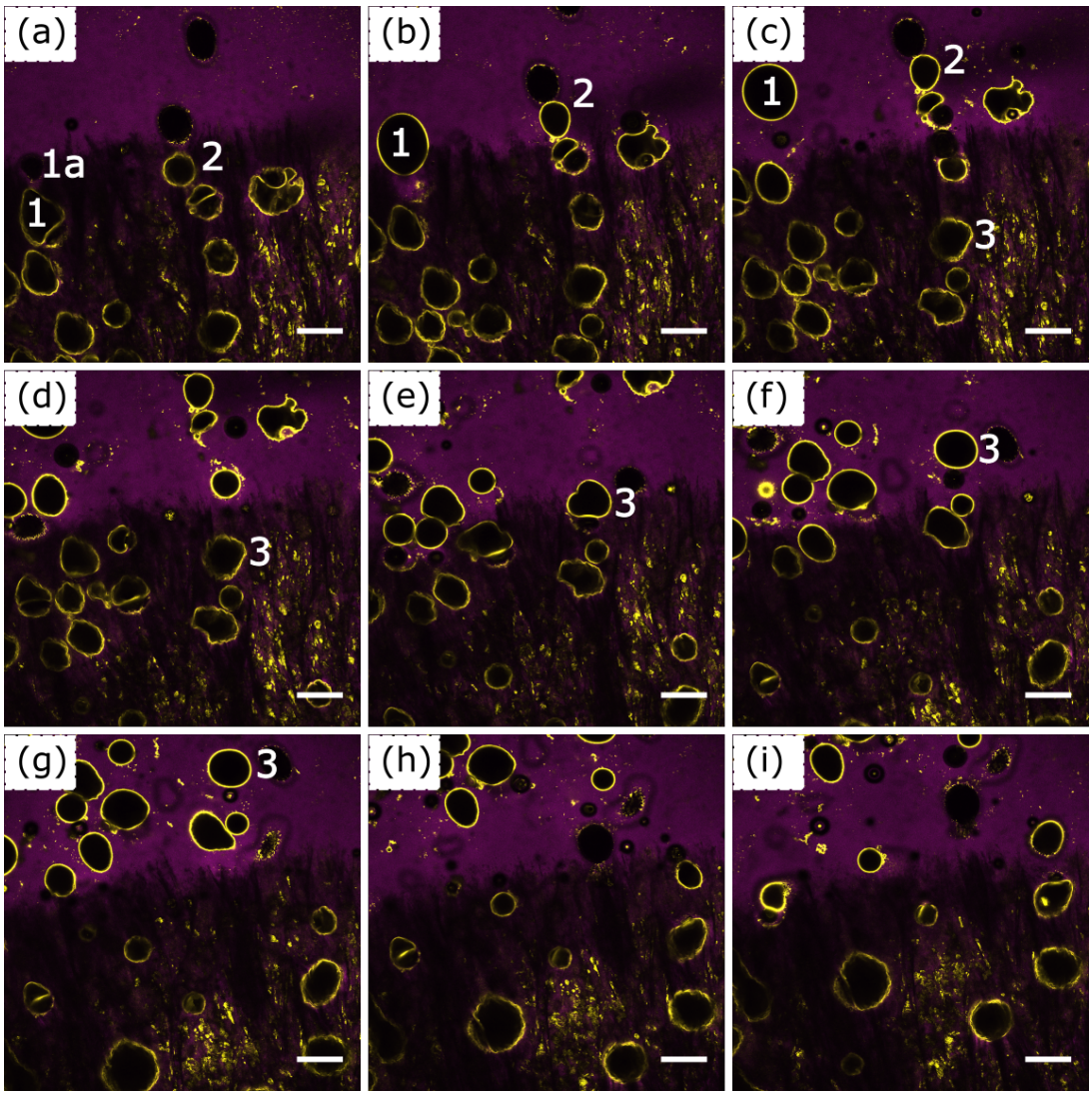

Figure 6.8 *Droplets released from the solid hexadecane as it thaws. Droplets 1-3 lose their wrinkles as they are released and return to ovals or even close to spherical as for droplet 1. Droplet 1 also undergoes coalescence with droplet 1a which has a low surface coverage of particles. Images are spaced 5.1 s apart. Scale bars: 100 µm*

Figure 6.8 shows an emulsion sample as the hexadecane thaws. The droplets are released from the hexadecane and return towards spherical from the deformed

shapes they take while trapped (see droplets numbered 2-3 for specific examples). As these droplets are close together, some droplet coalescence also occurs, demonstrated by droplets 1 and 1a in panel (a) which are coalesced by panel (b). In this case, droplet 1a has very few particles on its surface which may be a result of similar behaviour to that observed in Fig. 6.7 where particles have been removed from the interface, thus this may have made it easier for droplet 1 to end close to spherical; the increased volume without the increase in particles achieved with two fully-coated droplets prevented an excess of particles on the interface, thus allowing the droplet to return to equilibrium. In the sample imaged, the droplets observed during thaw were quite close together rather than far apart as would be expected for a dilute emulsion. This is due to either poor shaking of the stock vial before filling the sample cell, or the droplets being pushed together during filling or freezing.

6.5 Discussion

As described in Section 6.1, there are different ways a droplet can be trapped by the solidification front. Our results most commonly show droplets either being engulfed immediately, or being pushed for a while, then progressively trapped. The droplet behaviour depends both on the shape of the freezing front and on the velocity at which the sample moves. The behaviour observed here can be compared both to the single particle-stabilised droplet behaviour presented in Chapter 5 (same droplets, different freezing mechanism) and to the behaviour of surfactant-stabilised emulsions undergoing directional freezing (different droplets, same freezing mechanism).

Within these results, some of the behaviour observed agrees with the results from Chapter 5. In both cases, droplets are deformed by their interaction with oil crystals and the shape is at least partly controlled by the direction of crystal growth. The 3d images of droplets in Fig. 6.7 confirm that droplet deformation causes gaps to appear in the particle layer as bare patches can be seen on the interface even before the droplet is split. This shows that there is free space for the particles to unjam and move on the interface and if particles are not removed from the interface, this would also allow for the particles rejamming at a lower packing fraction during the thawing process. However, here droplets are partially trapped and then released which was not observed in the other setup. Previously, the crystallisation came from multiple directions, thus the droplet

was generally surrounded by crystals before any part of the droplet could split off and be released whereas here, there is always free fluid for the split-off droplet to move into.

During thawing, some different behaviour is observed here compared to Chapter 5. Some of the droplets, such as number 3 in Fig. 6.8, return to spherical after thawing which was not generally observed previously. The reason for this may be that particles have been removed from the interface during freezing, as shown in Fig. 6.7, and as such the lower surface coverage of particles means that the particles do not jam on the droplet surface before the droplet becomes spherical. This is also noticeable in the complete coalescence of some droplets, such as 1 and 1a in Fig. 6.8 (a), which could not occur if the droplets were fully coated with particles as the surface area decreases during coalescence for a fixed volume. In previous single droplet experiments both of these options were inaccessible as firstly the higher dilution of the sample meant that no droplets were close enough to even partially coalesce and secondly as the droplets were trapped by crystals growing from multiple directions. This prevented droplets moving and stretching far enough to be split and thus prevented the reduction in surface coverage of particles on the droplet.

The droplet behaviour here also differs from that observed by Deville *et. al.* in their experiments with surfactant-stabilised droplets in the same temperature stage [153]. No droplet deformation was observed, but instead the droplets were engulfed by the solidification front. It is possible that the shape of the solidification front played a role in this. In the work by Deville *et. al.*, the front was planar whereas here we observe a non-planar front in which many crystal 'needles' were present. This may have changed the interaction between the crystal and the droplets.

The results here also suggest that the presence of the particles is a major contributing factor. In Fig. 6.6, the droplet labelled '1' is not trapped and it has a low surface coverage of particles, while the droplet labelled '2' has a high surface coverage of particles and is trapped completely by the growing front. This cannot be attributed purely to droplet size, as the same figure shows droplets both larger and smaller than number 1 being trapped, thus suggesting that the droplet trapping here is primarily due to the particles on the interface.

6.5.1 Force balance for particle-stabilised droplets

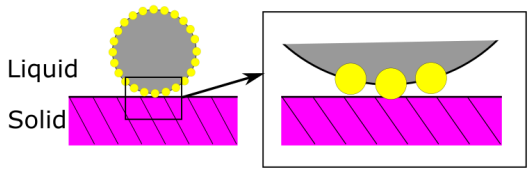

Figure 6.9 *Particle(yellow)-stabilised water(grey) droplet in a liquid with a solidification front(purple) approaching at velocity v. Upon contact between the droplet and the front, a stabilising particle may first be engulfed before the remainder of the droplet.*

Considering again the force balance required to calculate the critical engulfment velocity discussed in Section 6.2.1, this is a balance between viscous drag and a disjoining force. In those equations, the assumption of a solid particle was made, whereas here we use solid-stabilised liquid droplets. In this case, although the drag force applies to the whole droplet, the relevant disjoining force could be considered as that between the stabilising particle and the interface, rather than the whole droplet. This is shown schematically in Fig. 6.9. In order for a droplet to be engulfed by the solidification front, the particles on the interface must first be at least partially engulfed. The viscous and surface forces can then be rewritten as

$$F_{\text{viscous}} = \frac{6\pi\eta v R_{\text{d}}^2}{d} \ , \tag{6.16}$$

where R_{d} is the radius of the whole droplet and

$$F_{\text{surface}} = 2\pi r_{\text{P}} \Delta\sigma_0 \left(\frac{a_0}{d}\right)^n \ , \tag{6.17}$$

where r_{P} is the radius of an interfacial particle. Again using force balance to determine an expression for the engulfment velocity gives

$$v_{\text{c}} = \frac{\Delta\sigma_0 d}{3\eta} \left(\frac{a_0}{d}\right)^n \left(\frac{r_{\text{P}}}{R_{\text{d}}^2}\right) \ . \tag{6.18}$$

Now this expression for velocity contains a dependence not just on the droplet size, but also on the size of the stabilising particles such that larger stabilising particles will increase the critical velocity required for engulfment. In the case of a poorly stabilised droplet, it may be that there are no particles in the droplet-front contact region. Then the solidification front does not interact with a particle, but

rather the droplet as a whole, effectively setting $r_{\mathrm{P}} \sim R_{\mathrm{d}}$. For 50 μm droplets stabilised by 1 μm particles, this then increases the critical engulfment velocity by a factor of 50. This could mean that the front velocity is high enough to trap the droplet when it first traps the stabilising particle, but not high enough to trap the bare droplet.

It should be noted that this explanation assumes the only factor in Equation (6.18) which changes between a bare and a coated droplet is the effective size of r_{p}. In fact it is possible that, although the values of a_0, d and η will remain the same, the value of $\Delta\sigma_0$ may change. This could then either enhance or diminish the effect of going from a particle-stabilised droplet to a bare one. The value $\Delta\sigma_0$ depends on the front-'object' and the fluid -'object' surface energies which will change between the 'object' being a PMMA particle and a water droplet. Values for these energies are difficult to obtain and as such may have to be determined experimentally in order to determine whether or not $\Delta\sigma_0$ has an effect. Experiments with completely bare droplets at a range of velocities would also then be interesting as thus far only surfactant-stabilised droplets have been studied outside of the work in this thesis and in that case the surfactants also play a role in the droplet behaviour [153].

Consideration of the wetting layer

In considering the theory in which a wetting layer is included (Section 6.2.2), it is more difficult to translate the results from a solid particle, or bare droplet, to a particle-stabilised droplet in the manner described for the simpler theory. It is possible that such a wetting layer exists, as has been observed by Dedovets et al for surfactant-stabilised emulsions [153], but it is not easy to observe in the results presented here due to the non-planar solidification front. Even if that assumption were to be made here, it is no longer obvious that the same direct substitution of particle radius for droplet radius can be made in the expression for thermomolecular/disjoining force (Equation 6.12). The derivation of the disjoining force requires integration over the surface of the particle, but in the case of a particle-stabilised droplet, a portion of the particle is attached to the droplet rather than being completely surrounded by unfrozen continuous phase. This means that the integration is not straightforward and thus it is not clear that the direct substitution is valid. Further research would be required to settle this, for example by a observing the behaviour of the critical velocity as a function of

particle and droplet radius and comparing to the critical velocities obtained from theory.

6.6 Conclusions and future work

In this chapter, the interaction of particle-stabilised droplets with a solidifcation front via directional freezing has been explored. Results show that when freezing droplets, the droplet is first trapped by the front, then is either completely engulfed, or the droplet is split as it pulls away from the front, leaving an untrapped, partially coated droplet and a smaller trapped droplet/mass of particles. The results suggest that the primary interaction between the front and the droplets is between the growing crystals and the stabilising particles. As in previous chapters, these results show that control over the crystallisation and the crystal-particle interaction is key in determining the behaviour of the droplets during freezing.

Further experiments are required to tune the experimental procedure in order to fully understand the effects of temperature gradient and front velocity on the sample structure. In future work, it would be valuable to fully explore the effects of temperature gradient and front velocity in order to establish the configuration least damaging to the droplets. It would also be interesting to test a particle-stabilised oil-in-water emulsion. Given previous experiments, it would be expected that in this case, the water-continuous phase could yield a planar front rather than the range of front shapes observed for hexadecane-continuous emulsions. Finally, this setup has the capability of imaging samples at the particle-level and as such freezing experiments could be carried out at a higher resolution, allowing more in-depth study of the interaction between the particles and the solidification front which could in turn provide further insight into the mechanism by which the droplets are trapped.

Chapter 7

Freeze-thaw stability of Pickering emulsions

7.1 Introduction

Freezing is an important process both in industry and by consumers, as has been previously discussed. Equally, Pickering stabilisation is industrially relevant and has advantages over surfactants such as enhanced stability and reduced allergenic risk [41, 62, 63]. Having observed the interaction between individual droplets and a freezing continuous phase, it is now useful to understand how the dynamics change when the system is not only individual droplets, but droplets close enough to interact with one another.

In commercial products, droplets are more commonly found in more densely packed emulsions than alone, *i.e.* as emulsions. The stability of emulsions undergoing freeze-thaw cycles has been discussed in Chapter 2 and has been shown to vary depending on the experimental conditions and emulsion materials. In the case of surfactant-stabilised emulsions, the emulsions have been shown both to be stable to freeze-thaw cycling and to be broken up during cycling depending on factors such as the order the components freeze [75, 114]. In the case of particle-stabilised emulsions the picture is less clear and again, factors such as the freezing rate and freezer temperature have been shown to affect the emulsion stability [5].

In this chapter, confocal microscopy is used to probe the behaviour of model

particle-stabilised emulsions undergoing non-uniform or uniform cooling. A model three-component system is used in order to distinguish the structural effects of the freezing process from any effects due to stabilisers, cryoprotectants or additional components in either the dispersed or continuous phase. The emulsion behaviours from the two cooling configurations are compared and the final emulsion structures are studied. The effect of droplet size and cooling rate on emulsions undergoing uniform freezing is explored. In addition, the behaviour of particle-stabilised emulsions is compared to that of surfactant-stabilised emulsions and conclusions are drawn on the role of the particles in the emulsion behaviour.

7.2 Materials and Methods

In some experiments, the order in which the components were expected to freeze was reversed by changing the oil used in the continuous phase. Water-in-hexadecane emulsions are used for experiments in which the continuous phase freezes first, while water-in-dodecane emulsions are used for experiments in which the droplet phase freezes first. The temperature stage used is described in Chapter 3, and the details of the setup for these experiments are given below. Methods for making particle-stabilised water-in-hexadecane emulsions are given in Chapter 3.

7.2.1 Surfactant-stabilised emulsions

Surfactant-stabilised water-in-oil emulsions were made as follows. Span 80 (S6760, Sigma-Aldrich) was used as received and 0.046g added to 2.31 g of fluorescently labelled hexadecane and then subjected to 60s vortex mixing. Deionized water (2.56 g) was added and the sample was emulsified through 60 s vortex mixing. The emulsion contained 1 wt-% of Span-80 and this yielded emulsion droplets with diameters in the range 1 to 35 μm, as determined by confocal microscopy.

7.2.2 Water-in-dodecane emusions

In order to make water-in-dodecane emulsions, 0.1 g of dry PMMA particles (NBD dyed, see Chapter 3 for details) were added to 2.3 g n-dodecane (>99%, Sigma-Aldrich) and the dispersion was then placed in the ultrasonic bath for 15

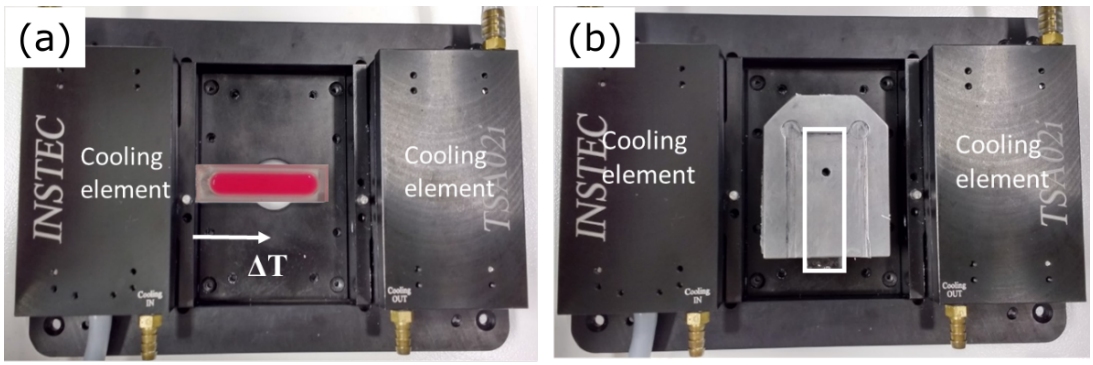

Figure 7.1 *(a)Sample positioning in the temperature stage for non-uniform freezing. The left end of the cell is in contact with the cooling element of the temperature stage, while further along the sample sits around 0.5mm above the viewing window. (b) sample positioning for uniform freezing. The sample cell, denoted by the white rectangle, is placed inside a metal casing and rotated 90° relative to the non-uniform setup .*

minutes, followed by 15s vortex mixing. This was repeated 3 times to ensure particles were well dispersed in the oil. A mass of 2.1g of deionized water was then added to the dispersion and the samples were emulsified via 60s of vortex mixing and 5 minutes of standing time, repeated 3 times to ensure all the water was emulsified.

7.2.3 Freezing emulsions

Water-in-hexadecane emulsions were studied undergoing freeze-thaw cycles in two different conditions - uniform and non-uniform freezing - using the Instec temperature stage described in Chapter 3. The two stage configurations are included again in Fig. 7.1 for clarity. A range of cooling rates between 0.5 and 8 °C/min were used for samples with droplet sizes in the range 25 - 100 μm. The 50 μm (predicted size) droplets were measured at least once for each of the selected cooling rates in both stage configurations. All droplet sizes were measured at a cooling rate of 8 °C/min at least once per stage configuration. In addition, a selection of other cooling rate/droplet size/stage configuration combinations were also tested but for clarity are not presented in this thesis. A fresh emulsion sample was pipetted from the stock emulsion into a clean sample cell for each measurement to ensure that no sample was affected by any other freeze-thaw cycles prior to the measurement of interest.

Water-in-dodecane emulsions could not be frozen in the Instec temperature

stage as the sample had to be cooled below 5°C, the lower limit of the Instec temperature stage capability. Thus a liquid nitrogen cooled stage (Linkam LTS350 with TMS93 controller) was used as this can reach temperatures down to −196°C. The stage was not compatible with the confocal microscope and thus was used with a Nikon Eclipse e800 optical microscope which is described below. The temperature of the stage and the cooling rate were adjusted via the controller.

Samples were prepared in the same sample cells as for the water-in-hexadecane emulsions. The temperature was cycled between 20 °C and -20 °C at selected rates between 2 and 6 °C/min. The lower temperature is below the freezing point of both water and dodecane, which freezes around -9.6 ° [26, 175].

7.2.4 Long-term stability experiments

Emulsion samples were made using the same procedure as before, but instead of being made in vials, were made in rectangular plastic cuvettes (4ml, Fisherbrand). Six cuvettes were filled almost to the top, with a small air gap at the top and were then placed in a refrigerator at around 8°C so that the oil froze, but the water remained liquid. Samples were imaged monthly for the first 6 months, then at 12 months. A power cut of unknown duration then brought the experiment to a halt, as it was expected that the samples could have melted during the power outtage, affecting the structure. Samples were imaged in a pre-cooled temperature stage such that to our knowledge, samples did not thaw during the 12 months.

7.2.5 Optical microscopy

Water-in-dodecane emulsions were imaged using a Nikon Eclipse E800 upright microscope with either a 10×/0.3 NA objective lens or a 20×/0.45 NA lens. Samples were imaged from above in fluorescence reflection mode. A mercury lamp with a band pass filter was used to excite the fluorescence from the NBD in the particles used. A QImaging Micropublisher camera was used with either Micrometrics SE Premium or QImaging software to detect the emitted fluorescence and capture images which were exported as tiff files. Images were analysed using ImageJ. Scale bars for these images were determined using an image of a measurement grating with known spacing.

7.2.6 Multiphoton microscopy

Due to the requirements of the multiphoton micorscopy setup, different sample cells were required to allow imaging using a water immersion objective. This required a sample with a thin glass coverslip as the base, rather than the thicker base of the standard sample cell. Alternative sample cells were made by cutting off the bottom of an 8ml glass vial and substituting it for a 22 mm $\times$ 22 mm microscope coverslip (Menzel-Gläser #1). The difference in sample cell also requires a different configuration in the temperature stage for sample freezing. In the non-uniform case, samples were placed half-on, half-off the glass window so that during freezing the sample sits near the point of highest temperature gradient. In the uniform case, the samples were too large to be placed inside the metal casing. The best alternative for these samples was to place them in the corner of the stage next to a cooling element but as far as possible from the viewing window and the stronger temperature gradient. After freeze-thaw cycling, the samples were removed from the stage and transferred into an insulated box containing ice to transport them from the confocal laboratory to the multiphoton laboratory in which they were imaged.

The microscope used for multiphoton imaging was a custom-built LaVision TriM scope II platform with a large Luigs und Neumann inverted stage. The glass coverslip of the sample cuvette was optically coupled to a water-immersion 25$\times$ Nikon NA1.1 W lens (MRD 77220).

As with standard confocal microscopy, two lasers were used to excite the two fluorescent dyes in the emulsions. DiIC18 was excited by a pulsed Titanium::Sapphire laser (Chameleon Ultra II, Coherent) tuned to 900 nm. Nile Red was excited by a Coherent/APE OPO laser tuned to 1100 nm. A 740 nm LP dichroic filter was used to separate excitation from the emitted light in the direct detection port of the microscope. The non-descanned, emitted light was separated by a 560 nm long-pass beam splitter and then filtered by an ET525/70 bandpass filter for DiIC18 and an ET610 long-pass filter for Nile Red. The filtered light was collected by two Hamamatsu GaAsP detectors (H7422-40-LV 5M).

7.2.7 Sample characterisation

Particle-stabilised droplets were sized as follows: image stacks were loaded into ImageJ and the particle fluorescence channel duplicated. The clearest image of the emulsion prior to the sample freezing was extracted and then the image thresholded appropriately. As the fluorescent signal from the particles has higher signal-to-noise than the one from the oil, a 'Hough transform' was applied to the image from the particle channel and the parameters varied until all the droplets were accounted for except those on the edges. This measured droplet sizes in increments of 1.25 μm. In some cases, a small number of droplets were missed and a small number of interstices included, but not enough to significantly affect the average droplet size measured.

Surfactant-stabilised droplets were sized similarly, though a 'smooth' function was applied twice before thresholding. 'Analyze particles' was used to extract the droplet sizes, because it is a faster method than the Hough transform.

The size of the droplets was taken to be the Sauter or surface-volume mean, $< R >$, to account for the polydispersity in the samples. The Sauter mean is calculated using the equation [35]

$$< R >= \frac{\sum_{i=1}^{N} R_i^3}{\sum_{i=1}^{N} R_i^2} \tag{7.1}$$

and polydispersity, PD, by

$$\mathrm{PD} = \frac{1}{R_{\mathrm{med}}} \frac{\sum_{i=1}^{N} R_i^2 \mid R_i - R_{\mathrm{med}} \mid}{\sum_{i=1}^{N} R_i^2} \tag{7.2}$$

where R_{med} is the median droplet radius. For the samples used in these experiments, the Sauter mean droplet diameter of emulsion batches ranged between 40.4 μm (polydispersity 40%) and 92 μm (polydispersity 33%).

7.3 Results and Discussion

7.3.1 Non-uniform freezing

First the non-uniform freezing of emulsions was studied using the setup shown in Fig. 7.1(b). Freezing begins at the end of the sample nearest to the cooling element and images are recorded at the viewing window. Fig. 7.2 shows a time series of images of an emulsion undergoing non-uniform freezing. Particle-coated water droplets are initially spherical and are dispersed throughout the oil. Some droplets are in contact with neighbours, but they are free to move. After the end of the sample nearest the cooling element drops below the oil freezing temperature, dark streaks appear in the oil, indicated by the arrow in Fig. 7.2(b), which grow over time. This indicates that the oil is beginning to freeze, as discussed in Chapter 4. Water droplets move away from the crystals and move closer together and in Fig. 7.2(j-l) droplets deform and pack into a foam-like structure [35, 176–178] as the droplets are trapped in the limited space between the oil crystals.

Crystals form first in the cooler part of the sample and grow into the warmer, still liquid, regions of the sample. Some droplets are pierced by growing oil crystals, causing shape distortion and in a few cases droplets split into multiple particle-coated droplets, as seen in the white square in Fig. 7.2(e)-(i).

In other cases, droplets are simply pushed around by the growing oil crystals. As crystals grow, locally the liquid regions become smaller, confining the droplets into increasingly smaller areas. This results in droplets being forced closer together, excluding much of the remaining liquid oil from between them in the process.

As the direction of crystal growth is not completely controlled, crystals do not all grow in exactly the same direction, although broadly speaking they move from the cold end of the sample to the warmer end. This means that some crystals grow in towards each other, restricting the access of some droplets to the remaining liquid regions. This is particularly relevant to droplets near the glass cuvette base. As coalescence of neighbouring droplets is unfavourable due to the particle barrier on the surfaces of both droplets, the most compact structure they can attain is the foam-like structure. Due to the nature of the temperature stage setup, it is not possible to reach high enough magnifications to observe these structures at a particle level and so it is unclear whether the droplets in these

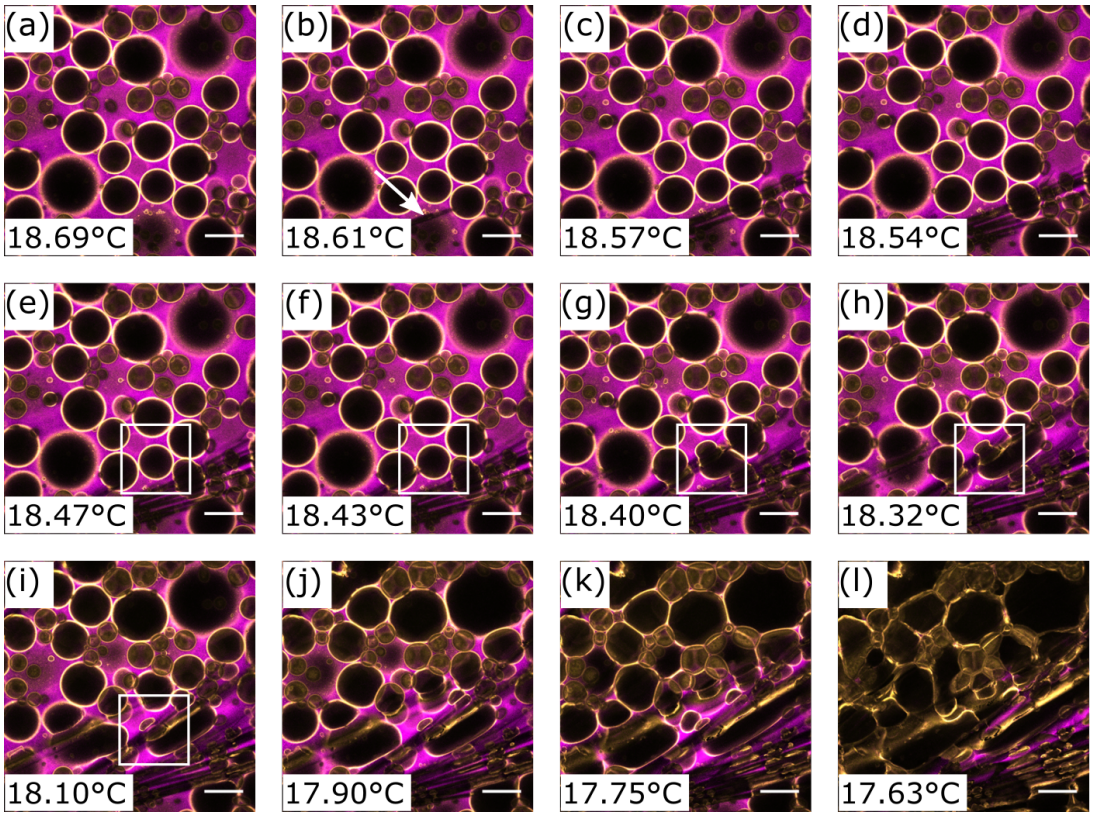

Figure 7.2 *Confocal micrographs of a particle(yellow)-stabilized water(black)-in-oil(magenta) emulsion taken during an 8 °C/min non-uniform freeze. Temperatures shown are those determined close to the field of view (see Chapter 4 for method). Images are taken (a-h) 3.1 s and (h-l) 15.7 s apart. Note that the fluorescent signal from the oil is lost as it crystallizes. Oil crystals begin to form in (b), denoted by the white arrow, and droplets are squeezed together into foam-like structures as shown in (j-l). The white rectangle highlights droplet splitting. Scale bars: 100 µm.*

foam-like structures are separated by two layers of particles, one for each droplet, or by a single, shared barrier with particles attached to both interfaces, known as bridging [179].

The foam-like regions observed are most commonly found in the region of the sample over the glass viewing window. As shown in Chapter 4, this is the region of the sample with the largest temperature difference to the cold region, meaning this is the area in which the oil will be liquid for the longest. This is therefore the area to which it is easiest for the droplets to migrate as the oil crystallises from the sample ends. In addition, the foam structures form at the bottom surface of the cuvette. This could suggest that the foam-like regions form due to pressure from crystals higher up in the sample preventing droplets from moving upwards. It could also be due to the emulsion having a higher density than the oil phase meaning that droplets already have a tendency to sediment towards the bottom glass. These structures remain after the emulsion thaws, indicating that it is locked in by the jamming of the particles at the interface.

The size of the foam-like region varies depending on the locations of oil crystal nucleation and growth. In the temperature stage used for these experiments, crystal nucleation is not directly controlled, it is only controlled indirectly via the applied temperature gradient and the cleanliness of both sample and sample cell from impurities. Therefore the size of the foam-like regions also cannot be directly controlled.

Having studied these samples mainly in 2 dimensions, it would be useful to understand whether the structures observed are purely surface effects which do not persist in bulk, or whether there is change to the sample structure in the z-direction. Here, we have no direct measure of the temperature profile in the z-direction due to the small sample height relative to the temperature probe size, but as the strongest temperature gradient is applied along the length of the samples, it can be assumed that the difference is not larger than the difference along the length of the sample. The crystallisation is still expected to vary throughout the bulk, thus the structure of the sample may also vary. In order to probe this further, two photon excitation microscopy is used to image deeper into the sample in the z-direction. Fig. 7.3 shows x-z and y-z micrographs of a non-uniform sample. Although the sample was treated slightly differently here due to experimental constraints (see Chapter 3 for details), the foam-like region present in the x-y plane (central image) can be seen to persist in the z-direction for at least two layers, showing that although this may be an effect caused by the

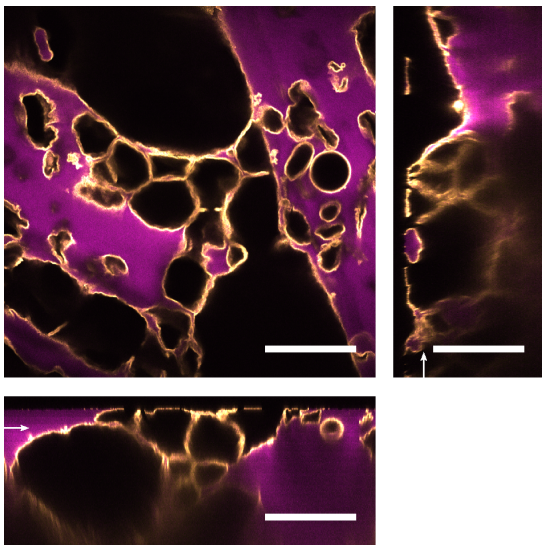

Figure 7.3 *3D structure of water-in-oil(magenta) emulsion stabilized by PMMA particle(yellow) after undergoing a single 4 °C/min non-uniform freeze-thaw cycle: xy (square), xz and yz-slices are shown with the xy slice taken at the height shown by the white arrow. Scale bars: 100 µm.*

surface, the sample is affected at a greater depth than one layer of droplets.

Variation of sample structure

As can already be observed in Figs. 7.2 and 7.3, and indeed as could be expected, non-uniform cooling of a sample results in a non-uniform sample structure after thawing. The variation is not only present across multiple samples, but also within an individual sample. By imaging an emulsion sample along its length after a freeze-thaw cycle, the different structures which form can be observed. This is shown in Fig. 7.4, where the approximate location at which samples were imaged is marked on a schematic of the emulsion sample cell. In addition to the foam-like structure discussed earlier, a mix of partially coalesced droplets and single droplets are present, some of which appear buckled or wrinkled. The reason for this range of structures is again the lack of control over crystal nucleation and growth. As cooling is not uniform, crystal growth is also not uniform, and therefore droplets interact differently with crystals depending on their location in the sample, leading to non-uniform structures. This makes the progression of structure difficult to predict in this experimental setup.

In many household and industrial applications, non-uniform cooling is likely to

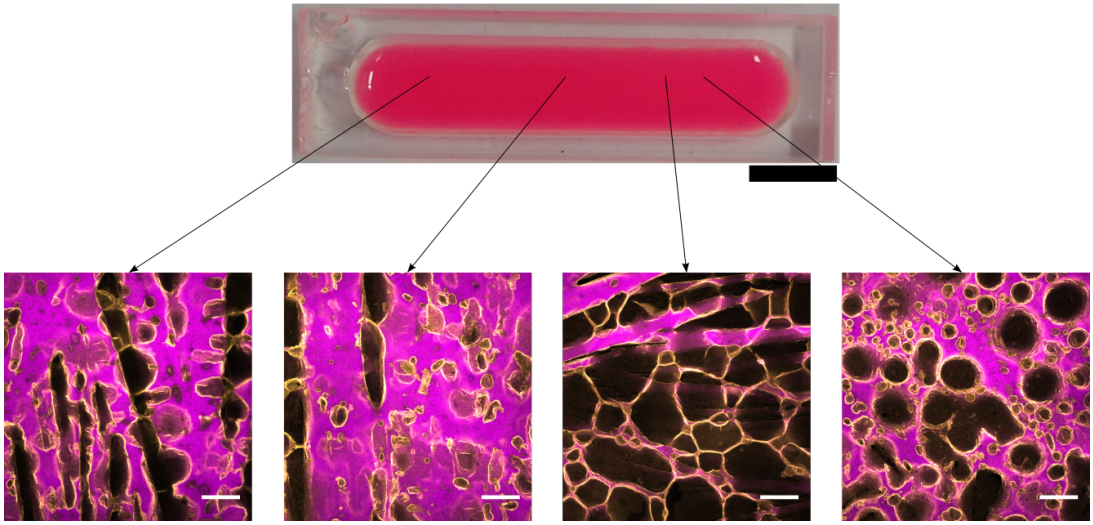

Figure 7.4 *Series of confocal micrographs taken along the length of a water-in-oil(magenta) emulsion stabilized by PMMA particles(yellow) that was first cooled under non-uniform conditions and then thawed by heating at the same rate; initial droplet size was 92 μm and cooling rate was 8 °C/min. Different regions of the sample display different structures due to the non-uniform cooling. Arrows show the approximate position at which the images were taken. Scale bars: 10mm on sample cell image and 100 μm on emulsion images.*

be the process which occurs. For example, placing food products in a household fridge or freezer will subject them to non-uniform cooling as the temperature inside will vary from one point to another [180]. This is especially true when other products are present which affect the air circulation and thus temperature distribution [181]. However, it is challenging to understand the freezing process and to observe trends in any of the other experimentally controllable parameters such as droplet size when the crystal growth is unpredictable, as here in the non-uniform case. Therefore, uniform cooling is employed so that the effects of crystal growth are more limited and/or reproducible and thus other trends can be more clearly studied.

7.3.2 Uniform freezing

Before considering the effects of any other parameters, it must be shown that 'uniform' cooling leads more uniform crystal growth and sample structure. Uniform freezing is carried out using the setup shown in Fig. 7.1 (b). By removing the temperature gradient, the oil in the sample all freezes at the same time, or within a very short time frame. Fig. 7.5 shows images of an emulsion

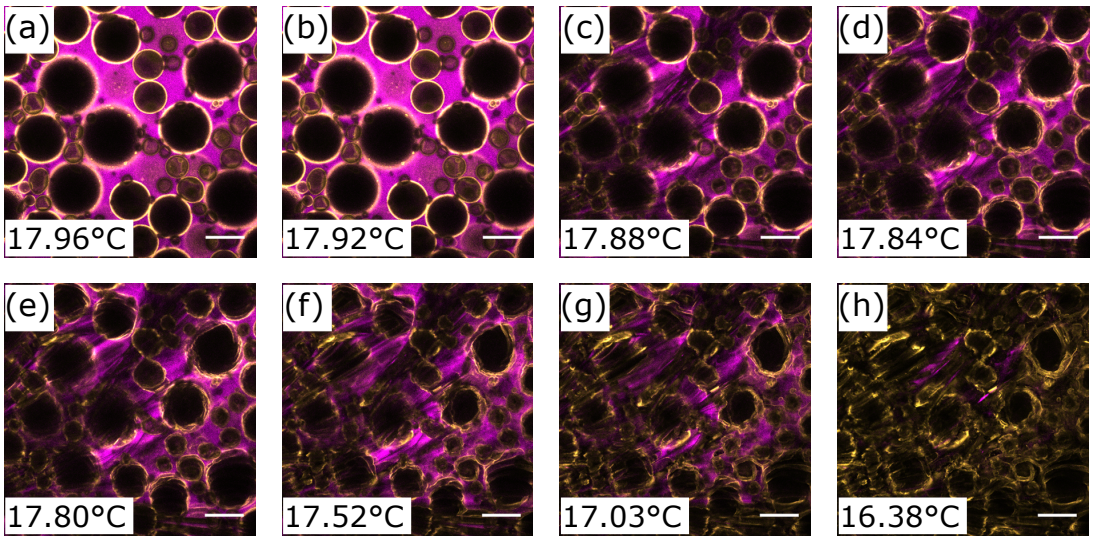

Figure 7.5 *Confocal images of a water-in-oil(magenta) emulsion stabilized by PMMA particles(yellow) taken during uniform freezing at 8 °C/min; each image is labelled with the corresponding sample temperature calculated as described in Chapter 4. Images are taken (a-e) 3.1 s and (e-h) 15.7 s apart. As the oil crystallises, it fills the field of view within a short space of time in comparison to non-uniform freezing (Figure 7.2). Scale bars: 100 µm.*

undergoing uniform freezing. As for the non-uniform case, the sample initially contains spherical water droplets dispersed through the oil and free to move. As the temperature decreases, the oil begins to freeze and crystals form. This is seen again by the decrease in fluorescent intensity of the oil and its streaky appearance. These streaks first appear in Fig. 7.5(c) and then spread across the sample. The droplets here do not get pushed together but remain close to their original position, crumpling in the process, as seen in the yellow particle signal.

In contrast to the non-uniform case, the crystals appear across the whole field of view (640 μm $\times$ 640 μm) within a couple of frames. This is a result of the much-reduced temperature gradient. The temperature difference across large areas of the sample is now low enough that crystallisation can occur in larger regions of the sample at the same time, rather than the more gradual freezing from the ends inwards seen in the non-uniform case. As crystals form over regions much larger than a droplet radius at the same time, droplets become surrounded by solid crystal and are therefore trapped. As the crystal grows, the liquid region decreases locally, confining the droplet into progressively smaller volumes until the oil is completely crystallised. The droplet shape is then determined by the shape of the cavity in the surrounding crystals and as the water is still liquid, the droplets are free to deform and provide limited resistance against that deformation. Upon

thaw, droplets remain crumpled and are stable for at least three days.

The particle shell on these droplets provides us the reason for the droplet behaviour. Given that a sphere has the optimal surface area to volume ratio, any deformation of a sphere will therefore increase the droplet surface area for a fixed volume. As the particles are irreversibly adsorbed to the interface, when the surface area increases, the packing fraction of the particles decreases, allowing them to move on the interface. As the particles are now unjammed, when the oil thaws the particles can rearrange until they jam again. As in the single droplet case in Chapter 5, the particles may rejam at a lower packing fraction, preventing the droplets from returning to spherical.

Imaging further into the sample gives us another reason that the crumpled droplets may be stable. Using multiphoton microscopy again, x-z and y-z images can be taken, as shown in Fig. 7.6. Here not only are the droplets non-spherical in the x-y plane, but partial coalescence can be observed in the z-direction. Some droplets are dumbell-shaped as a result of partial coalescence. Complete coalescence is prevented by the particles at the interface. The total surface area of two single droplets is larger than a single droplet with the same volume as $A/V \propto 1/D$, thus the droplets will coalesce until the particles are jammed at the interface and then coalescence will cease.

As non-uniform cooling produced non-uniform emulsion structure, uniform cooling would be expected to produce a more uniform structure, particularly given the observations of the crystal growth. Fig. 7.7 shows images of an emulsion after undergoing a single uniform freeze-thaw cycle. The same kind of structures can be seen in each image; crumpled droplets - some individual and others partially coalesced with neighbours, connected by narrow channels. There is little qualitative difference between the images from each point, unlike in the non-uniform case (see Fig. 7.4).

7.3.3 Uniform freezing - the effects of droplet size and cooling rate

Having now shown that uniform cooling of samples leads to uniform sample structures, other parameters such as droplet size and cooling rate can now be considered, specifically their effects on emulsion morphology.

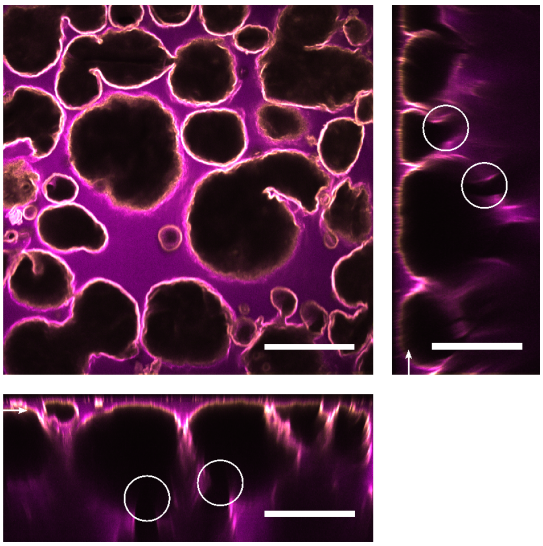

Figure 7.6 *3D structure of water-in-oil(magenta) emulsions stabilized by PMMA particle(yellow) after undergoing a single uniform freeze-thaw cycle: xy (square), xz and yz-slices are shown with the xy slice taken at the height shown by the white arrow; cooling rate during freezing stage: 4 °C/min. White circles denote locations where droplets have partially coalesced. Scale bars: 100 μm.*

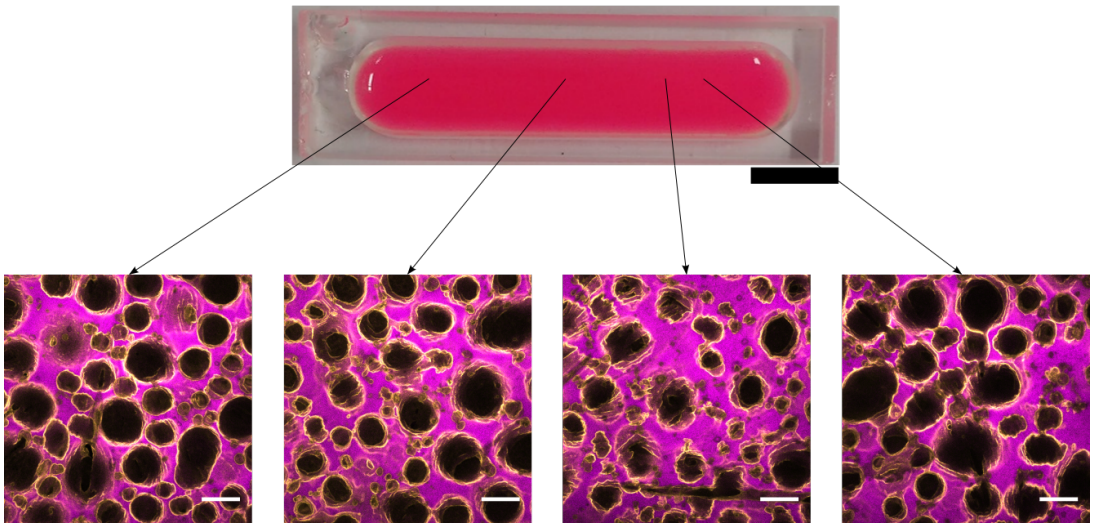

Figure 7.7 *Series of confocal micrographs taken along the length of a water-in-oil(magenta) emulsion stabilized by PMMA particles(yellow) that was first cooled under uniform conditions and then thawed by heating at the same rate; initial droplet diameter was 92 μm and cooling rate was 8 °C/min. Arrows show the approximate locations at which each image was recorded. In each image, a mixture of individual and partially coalesced droplets can be seen. Scale bars: 10 mm on sample cell image, 100 μm on confocal images.*

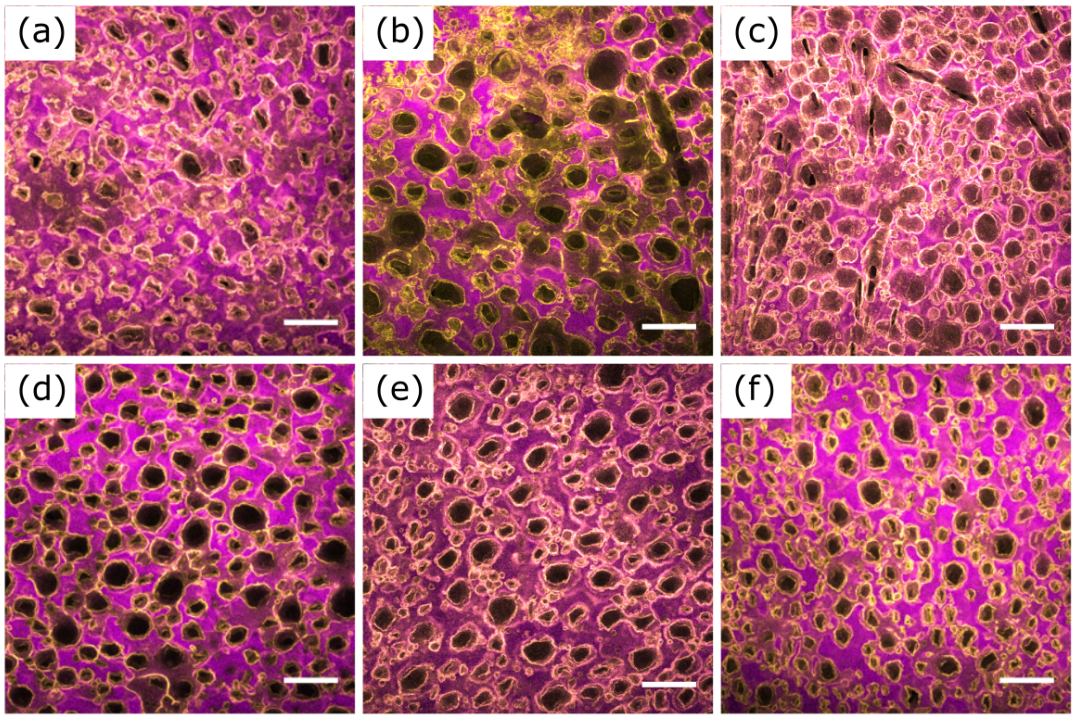

Figure 7.8 *Final thawed emulsion structure for similar 47 μm droplet emulsions after first having been frozen at rates of (a) 0.5 °C/min, (b) 1 °C/min, (c) 2 °C/min, (d) 4 °C/min, (e) 6 °C/min and (f) 8 °C/min; the behaviour of the samples is the same irrespective of the cooling rate. Scale bars: 100 μm.*

Cooling rate

The first parameter to consider is the cooling rate, controlled simply by the temperature stage. Fig. 7.8 shows emulsions with initial droplet diameters of 47 μm after a single freeze-thaw cycle at increasing temperature ramp rates. In each case, crumpled droplets and some partial coalescence can be observed but there is no clear effect of changing the cooling rate.

As the samples are cooled uniformly, the oil freezes on lengthscales larger than a droplet diameter in a short space of time, meaning that the final structure of the sample is determined from the point of crystallisation onwards, independent of the time taken to reach crystallisation. This means that changing the cooling rate, with the range of rates used here, has little effect on the final sample structure because the main effect that changing the cooling rate has is to change how long the sample takes before it starts crystallising.

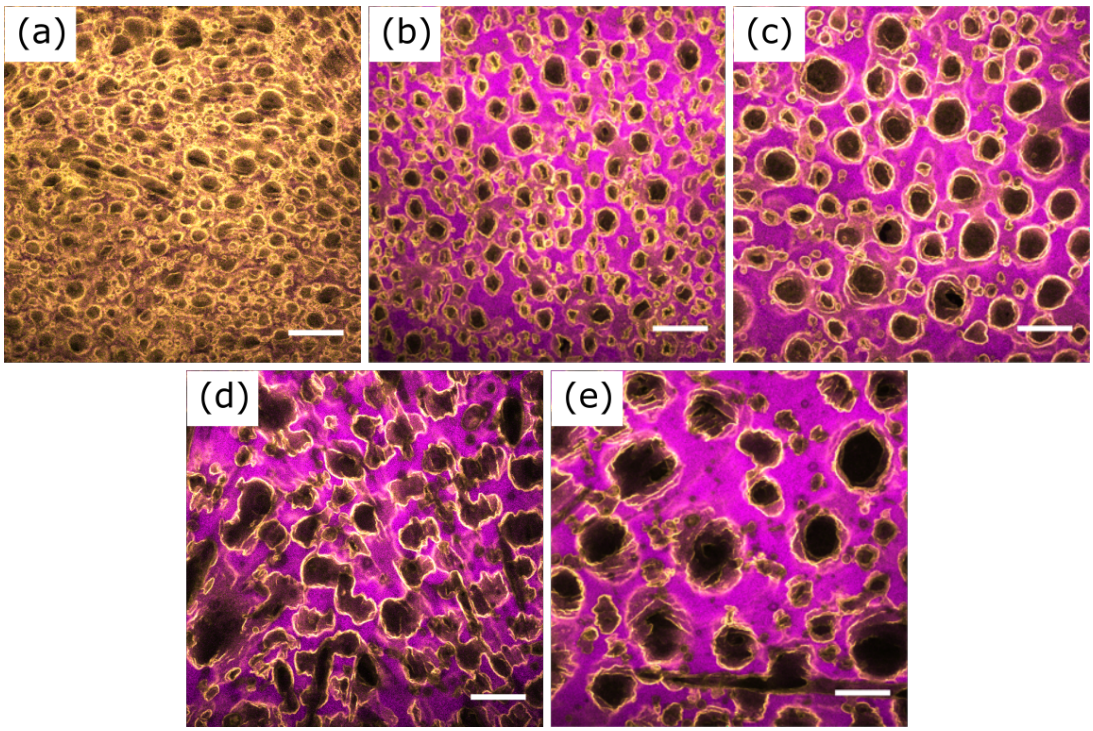

Figure 7.9 *Final thawed emulsion structure for water-in-oil(magenta) emulsions stabilized by PMMA particles (yellow) after undergoing an 8 °C/min uniform freeze-thaw cycle. Initial droplet sizes were (a) 40 μm, (b) 47 μm, (c) 69 μm, (d) 79 μm and (e) 98 μm. In each case crumpled droplets can be observed and the samples have the same structure aside from the differing droplet size. Scale bars 100 μm.*

Droplet size

After considering cooling rate, the effect of changing droplet size, controlled by the mass of particles added to the system, can be observed. Fixing the cooling rate at 8 °C/min, the droplet diameter is varied between 40 - 92 μm. The resulting emulsion morphologies after a single freeze-thaw cycle are shown in Fig. 7.9. Aside from the droplet size, the structure is qualitatively the same in each sample and there is no clear evolution of structure as the droplet size increases.

To explain these results, pressure balance must be considered. The pressure exerted on the droplet by the crystals drives the deformation and this is opposed by pressure from the droplets themselves. For the droplets, consider the Laplace pressure, P_{L}, which is defined as

$$P_{\mathrm{L}} = \frac{4\gamma}{D} \tag{7.3}$$

for a spherical droplet, where D is the droplet diameter and γ the interfacial tension. For droplets used here, D ranges from 40-92 μm and with surface tension of order 50 mN m^{-1} [24, 25], thus $P_{\mathrm{L}} \sim 2.2 - 5$kPa. It is difficult to estimate the pressure exerted by the oil crystals on the droplets, but given than the deformation of the droplets is mostly unchanged with increasing droplet size, we can say that the crystal pressure must be much larger than the Laplace pressures. This agrees with experiments carried out by Connell and Tombs who measured pressures of order 20kPa exerted by growing ice crystals on an object [182].

7.3.4 Surfactant-stabilized emulsions

Having studied the behaviour of particle-stabilised emulsions, it is useful to elucidate the role that the stabilising particles play in the emulsion behaviour during freeze-thaw cycling. To do this, an emulsion with no stabilising particles can be subjected to the same freeze-thaw cycles and the behaviour of both emulsion types compared during the cycle alongside comparing the final morphologies. By treating both surfactant and particle-stabilised emulsions in the same manner, any differences in behaviour or morphology are expected to be a result of the particles on the interface. As a water-in-hexadecane emulsion with no stabilisers is not stable for long enough to carry out experiments, surfactant-stabilised emulsions can be used. As explained in Chapter 3, surfactants stabilise emulsions by reducing interfacial tension, and thus do not have the same mechanical, rigid barrier-like properties as a particle shell on a droplet. Emulsions made with Span 80 as the stabiliser are comprised of droplets of diameters in the range 1 - 35 μm. Although these are smaller than those in the particle-stabilised emulsions used in this thesis, we have shown in Section 7.3.3 that droplet size does not affect the final structure of emulsions subjected to uniform freeze-thaw cycles, thus the behaviours of the two can be compared.

Fig. 7.10 shows a surfactant-stabilised water-in-hexadecane emulsion prior to freezing, frozen and post thaw. Only the oil is fluorescently labelled in these samples, thus any fluorescent signal observed comes from liquid hexadecane. This means that the image of the frozen sample is taken from the transmission channel due to the low intensity of the oil fluorescent signal in frozen state. Prior to freezing, the droplets are spherical and free to move in the oil, being separate from other droplets. Once frozen, the droplets appear crumpled in a similar

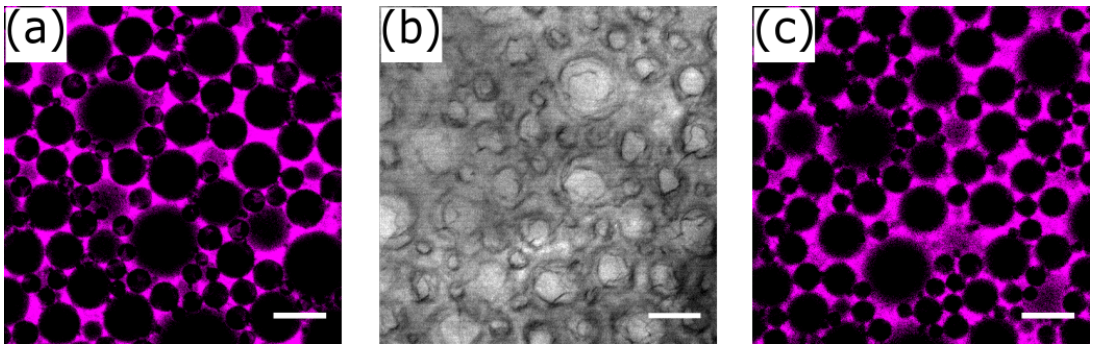

Figure 7.10 *Confocal images of a surfactant (Span 80, 0.9 %wt) stabilised water-in-oil(magenta) emulsion undergoing uniform cooling at 4 °C/min. (a) Initial emulsion in fluorescence channel and (b) frozen emulsion as imaged in transmission channel (see text for details); the droplets have crumpled in a manner qualitatively similar to particle-stabilized emulsions. (c) Thawed emulsion in fluorescence channel; the droplets have recovered their spherical shape. Scale bars: 25 μm.*

manner to the particle-stabilised droplets, but on thawing the droplets recover their original spherical shape. The average droplet size is similar to the droplet before freezing, being 5.7(4) μm pre-freeze and 5.1(3) μm post thaw. The slight difference between these two is attributed to small droplet movements relative to the focal plane during freeze-thaw cycling.

Comparing Fig. 7.10 (c) with Fig. 7.9, the substantial difference in structure between the surfactant-stabilised and particle-stabilised emulsions after a freeze-thaw cycle becomes clear. Pickering emulsions can be irreversibly damaged by the process, while surfactant-stabilised emulsions recover by themselves. This is a direct result of the irreversible adsorption of the particles to the interface versus the ability of surfactants to adsorb and desorb from interfaces at much shorter timescales [16]. When a surfactant-stabilised droplet is deformed, the surfactant does not jam on the interface but moves freely between the interface and the bulk, allowing the droplet to relax back to a sphere after a deformation. In addition, complete coalescence is achievable for surfactant-stabilised droplets, whereas it is not for particle-stabilised droplets, meaning that any surfactant droplets which do begin to coalesce will equilibrate again as a larger, spherical droplet in a manner not possible for particle-stabilised droplets.

Consider a droplet stabilized by particles that are closely packed at its surface ($\varphi_{2D} \approx 0.907$ for monodisperse discs [183]). When deformed (*e.g.* upon freezing), the droplet surface area increases (the spherical shape has the minimal surface-

to-volume ratio), potentially leading to unjamming of some interfacial particles. If the constraints on droplet shape are removed (*e.g.* upon thawing), the droplet may begin to relax, but the interfacial particles may re-jam at a lower surface fraction, e.g. random close packing $\varphi \approx 0.89$ or random loose packing $\varphi \approx 0.84$ [183], meaning the droplet cannot relax completely to a spherical shape. This effect is enhanced by partial coalescence, which leads to a reduction in interfacial area A per unit volume V. As, $A/V \propto L$ with L the typical size of the (partially coalesced) droplet, increasing L during partial coalescence leads to a smaller available surface area for fixed volume.

7.3.5 Long term frozen stability

So far, frozen emulsion stability has been considered only over short periods of time, typically 20-25 minutes. In reality, freezing is commonly used for product storage and products are required to be stable over timescales of order days-months. Although emulsions are damaged at the point of crystallisation, it is still unclear whether the emulsions then remain stable once the damage is done, or whether further degradation of the structure occurs.

Although it is not possible to see deeper than one droplet layer into the sample due to the crystallisation, it would be expected that any significant changes in the bulk would have some effect on the surface behaviour. As we previously observed structures beginning at the surface and persisting into the bulk (see Figs. 7.3 and 7.6), similar behaviour would be expected here also. Thus any changes observed in the surface structure could indicate changes in bulk structure. Figure 7.11 shows images taken from one emulsion at the same position (except the initial pre-freeze image) over several months. In panel (a) we see that the emulsion is again initially comprised of spherical droplets in contact with but not attached to neighbours. After one month in the fridge, the foam-like regions and individual, narrow oil crystals characteristic of non-uniform freezing can be seen (see panel (b)) and panels (c)-(e) show that the emulsion is unchanged over the period of 12 months. The crystals appear in the same position and configuration, while the foam-like structure also appears the same, with the 'cells' of the foam retaining their shape. Slight differences in image intensity are due to small differences in the focal plane of the image.

These results suggest that the damage to the emulsion structure occurs at the freezing and melting points in the cycle and once a morphology has been 'locked

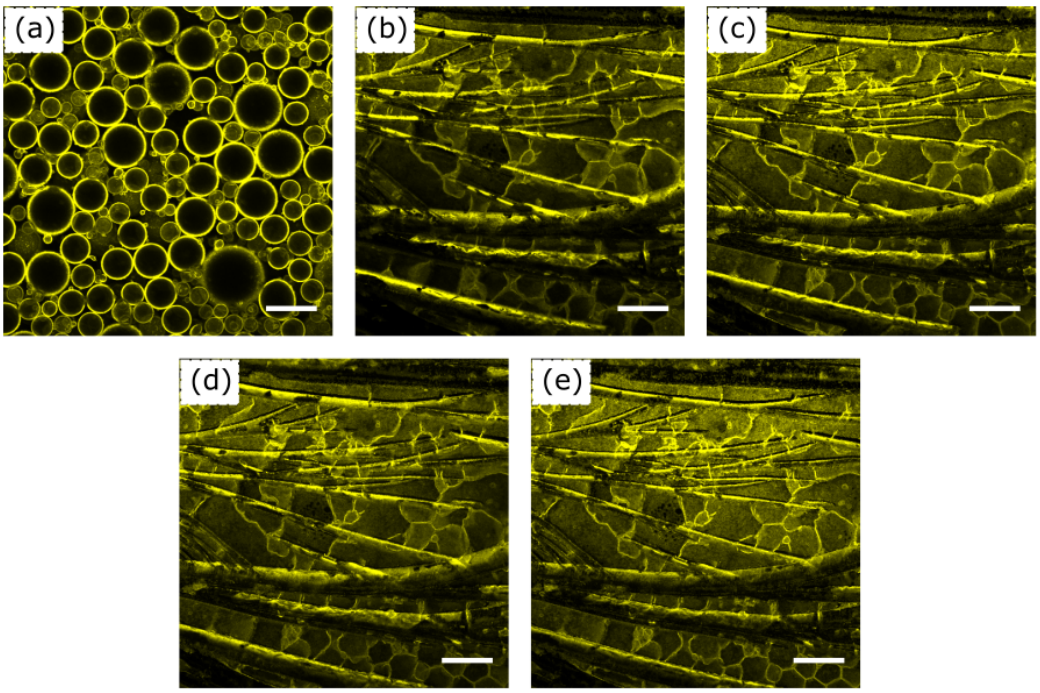

Figure 7.11 *Confocal images of a frozen particle(yellow)-stabilised emulsion over a year. (a) initial emulsion, (b) after 1 month, (c) after 3 months, (d) after 7 months and (e) after 12 months. Fluorescent dye was only present in the particles, but the crystals are still clear by their shape. Scale bars: 100 µm.*

in' during the freezing process, that structure remains as long as the emulsion remains frozen. From a stability perspective, this is advantageous because it suggests that further damage is not done while the sample is frozen. This would also then mean that were control over the freezing process to be achieved such that emulsions were minimally damaged during freezing, this would be maintained at least until thawing if not beyond.

However, this may well be dependent on the components used in the emulsion rather than a general principle, but this is currently unclear. For example, ice cream has been shown to change structurally in the freezer over long periods of time as a result of recrystallisation. This is affected by factors such as the presence of stabilisers or sweeteners and the product storage temperature/temperature fluctuations [184, 185], factors which do not necessarily apply to the model system used here.

7.3.6 Water-in-dodecane emulsions

In the water-hexadecane emulsions, the water has a lower freezing temperature than the oil, thus the water remains liquid while the oil freezes. However, in other systems, food-grade systems included, the order in which the components freeze is reversed such that the droplets freeze ahead of the oil [5, 57] It has been shown in surfactant-stabilised that this can have consequences for the emulsion stability, in some cases actually promoting coalescence between semi-crystalline droplets and undercooled, liquid ones [71]. This behaviour could be altered by the presence of stabilising particles which, if not removed from the interface, could provide a barrier against coalescence [5].

Preliminary studies on particle-stabilised water-in-dodecane emulsions were therefore carried out. Dodecane has a freezing temperature of -9.5 °C, and so freezes below the bulk freezing temperature of water. In this case, when the continuous oil phase begins to freeze, the droplets may already be frozen and thus the interaction between the two will change as the droplets are no longer easily deformable as in the water-hexadecane case. Again, these emulsions are stabilised by PMMA particles, so they will also play a role in the emulsion behaviour.

Due to the requirement for low temperatures, samples were frozen using the liquid-nitrogen-pumped Linkam stage and images are taken using an optical microscope in reflection mode. This means that the samples were imaged from

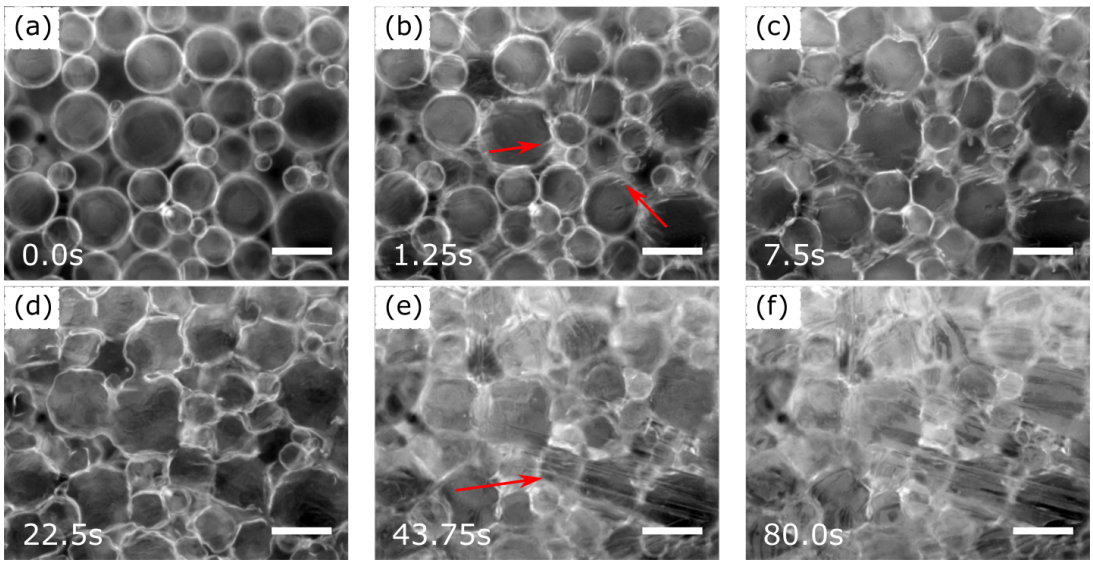

Figure 7.12 *PMMA stabilised water-in-dodecane emulsion freezing at a rate of 2 °C/min. Bright rings around the droplets indicate the presence of (fluorescent) PMMA particles. Images are taken at significant points during the cycle, indicated by the timestamps, where t=0 is one frame before crystals appear. (a)Initial emulsion before freezing. (b) Oil around the droplets begins to crystallise, shown by the red arrows. (c)-(d) Droplets are pushed together and some coalescence is observed between neighbouring droplets. (e) Larger crystals grow, as indicated by the red arrow, as the oil in the bulk freezes. (f) Frozen sample. Scale bars: 100 µm*

above and thus here the top surfaces of the samples were imaged rather than the bottom surface imaged when using confocal microscopy.

Figure 7.12 shows images of a water-in-dodecane emulsion cooling at a rate of 2 °C/min. First, small crystals form near the droplets and curve around the droplets, as indicated by the red arrows in panel (b). Then some of the droplets are pushed together and in panel (d) they can be seen to have coalesced. Finally larger crystals grow either as the bulk of the oil freezes or the top surface of the sample freezes, as seen in panels (e)-(f).

Figure 7.13 shows images of the emulsion as it melts, being heated at the same rate as during cooling. As the sample thaws, the oil crystals melt and bubbles appear in the droplet phase, indicated by the red arrows in panel (b). The droplets are still deformed at this point, but in panel (c) the droplets display some recovery as the droplet surfaces become more smooth. However, the droplets do not become completely spherical, and those which partially coalesced during the freezing phase remain so after thawing.

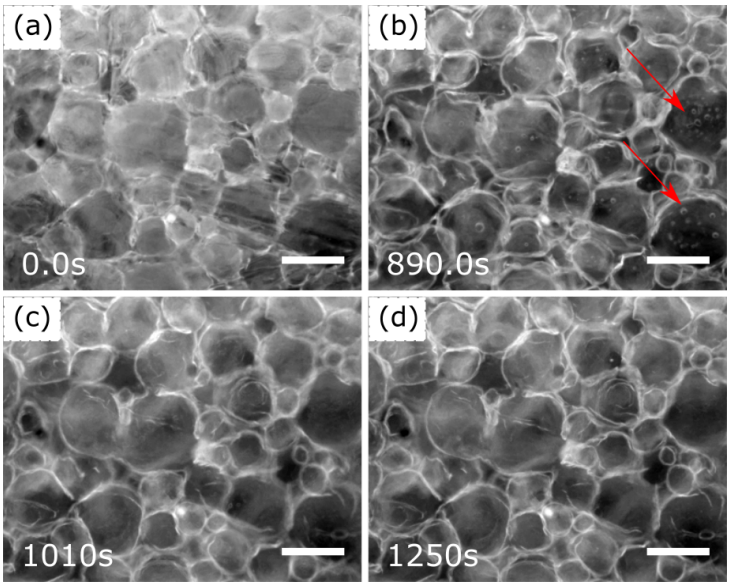

Figure 7.13 *PMMA stabilised water-in-dodecane emulsion thawing at a rate of 2 °C/min. Images are taken at significant points during the cycle, indicated by the timestamps, where t=0 is the start of the thawing process. (a) Frozen emulsion, (b)-(d) Images of the emulsion during thawing. The droplets begin to relax towards spherical, but are prevented due to partial coalescence with neighbouring droplets. The red arrows in (b) indicate the presence of air bubbles inside the droplets.*

The droplet behaviour observed during the freezing phase is similar to the behaviour observed in the water-in-hexadecane emulsions discussed earlier. In both cases, droplets are pushed together and some partial coalescence is observed. Here, the top surface of the sample is being imaged rather than the bottom surface as imaged during confocal microscopy but the sample structure appears similar. This suggests that the samples are frozen non-uniformly here as in the uniform case pushing of droplets together was not observed, although there may also be surface effects which apply here as we image the top layer of droplets.

The partial coalescence observed is an indication that the water droplets were still liquid when the oil began to freeze. Partial coalescence requires an interaction between neighbouring droplets. During freeze-thaw cycling of emulsions in which the droplets are frozen, coalescence has been shown to occur either upon collision with liquid/semisolid droplets during freezing, or between neighbouring solid droplets as they melt [71, 75]. Thus it can be assumed that the droplets here are liquid at the time the oil freezes. The reason for this is the lower freezing temperature of the water droplets compared to the equilibrium melting temperature of water [75, 186]. This is due to the droplets crystallising primarily via homogeneous nucleation where the crystal growth rate increases with the degree of undercooling, as discussed in Chapter 2.

It is possible that the water droplets do freeze later in the cycle. This is difficult to observe during freezing, but the appearance of air bubbles during thawing in Fig. 7.13(b) suggests the droplets may have frozen. As gas is more soluble in water than in ice, air molecules can be rejected by growing ice, producing bubbles in the water [187]. It is possible that these air bubbles could not escape the droplet during freezing and thus are only released upon thaw, once the system was fluid. Given that the structure observed in Fig. 7.12(d), where the droplets are definitely liquid, and Fig. 7.13(d), where the droplets are again liquid, is essentially unchanged, this indicates that even if the droplets did freeze, this had very little impact on the sample structure. This is the behaviour that would be expected given that the droplets would be freezing while encased in a solid continuous phase and while particles are present on the droplet surface, leaving little flexibility for the droplets to alter their shape.

7.3.7 Application

From an applications perspective, the advantages of particle stabilisation over surfactant stabilisation have already been discussed, particularly with regard to product shelf life and stability as well as aiding in transportation. However, the results presented here indicate that freezing particle-stabilised emulsions can cause severe, irreversible damage to the emulsion microstructure, particularly for non-uniform freezing and in cases where the droplet phase remains liquid while the continuous phase freezes. In light of these results, although Pickering emulsion may lead to enhanced product stability, the presence of interfacial particles may become detrimental in circumstances where freezing is required as the particles help to lock in the structural damage caused by droplet-crystal interactions. It has been suggested that the damage may be reduced if the droplet phase freezes first, but this may not always suit the product design.

7.4 Conclusions and future work

We have used confocal microscopy to investigate the structure of water-in-oil Pickering emulsions undergoing freeze-thaw cycles. We have investigated the behaviour of samples undergoing both uniform and non-uniform freezing, as well as considering the effects of altering the droplet size and cooling rate.

Non-uniform freezing of emulsions produces non-uniform post-thaw samples which display several different structures, notably foam-like regions resulting from droplets being pushed together by growing oil crystals. During uniform freezing, larger areas of the sample crystallise at the same time, meaning droplets are unable to move. Instead, they crumple as they are forced into non-spherical cavities within the frozen oil. We attribute this behaviour to irreversible particle adsorption: interfacial particles unjam when the droplet is deformed (freezing) and rejam when the restrictions on droplet shape are removed (thawing). However, they may rejam at a lower surface fraction, leading to a non-spherical droplet shape after freeze-thaw cycling. Long-term stability experiments show that structural damage occurs primarily during the freezing phase as little structural change was observed in samples kept frozen for 12 months.

We show that both cooling rate and droplet size have no significant effect on the final emulsion microstructure. The latter also means we can compare our

results to similar experiments employing surfactant-stabilized emulsions that have a relatively small droplet size. We show that these surfactant-stabilized emulsions survive freeze-thaw cycles relatively unscathed. We argue that these results are relevant in the context of food products: Pickering stabilization can be used to enhance their shelf life, but it can also result in irreversible changes to the microstructure if those products are subjected to freeze-thaw cycling during processing or use.

In future work, it would be interesting to further study the inverted water-dodecane system with a better imaging setup such that we could see clearly how the freezing water affects the particle layer and how that then is affected by the freezing of the continuous phase. As water expands on freezing, it could be expected to damage the particle shell, thus on thaw, further damage could be done to the emulsion structure. Equally, an oil-in-water emulsion where the oil freezes first could be a route to reducing droplet damage during freezing of the continuous phase, provided they are not damaged by the freezing of the internal phase.

Chapter 8

Formation of particle-stabilized bicontinuous emulsions by freeze-thaw cycling

8.1 Introduction

Bicontinuous structures are those in which the two phases are continuous and inter-penetrating [188, 189]. Of particular interest here are bicontinuous, interfacially jammed emulsion gels (bijels), bicontinuous structures formed from two immiscible liquids whose interface is stabilised by the jamming of colloidal particles (see Fig. 8.1) [190]. Bijels were predicted by simulations in 2005 [191] and realised experimentally in 2007 [192]. These materials have a large surface area and have the potential to be used in applications such as fuel transport in electrochemical cells [193], tissue engineering [194], microfluidic devices [192], templates for porous materials [195] and electrolytes [196]. In addition, the fabrication of bijels with food-grade components is also being explored for use as edible bijels [197].

Typically, bijels are produced via spinodal decomposition of two partially-miscible fluids. The process is arrested by the jamming of neutrally-wetting particles at the liquid-liquid interface [192]. As with particle-stabilised emulsions, the attachment energy of these particles is several orders of magnitude larger than $k_{\mathrm{B}}T$, thus once the particles reach the interface, they remain there [197]. The channel width of

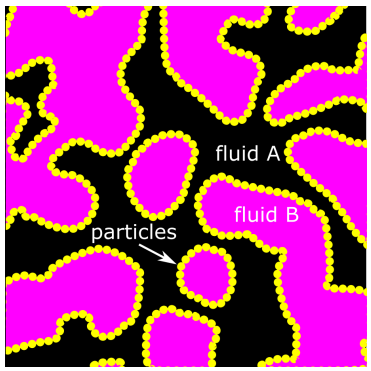

Figure 8.1 *Schematic of a bijel composed of two fluid phases, coloured magenta and black, with the interface stabilised by particles (yellow). The particles are neutrally wetting, thus have a contact angle of 90° Based on a figure from [198].*

a bijel is controlled by the volume fraction and size of particles, therefore the channel width, and thus interfacial area, of the bijel are tunable via the choice and amount of particles used.

There are drawbacks to this bijel fabrication process. This method requires careful experimental control in tuning the contact angle of the particles to 90° as non-neutrally-wetting particles can affect the bijel structure or prevent bijel formation, instead producing a particle-stabilised emulsion such as those discussed in Chapter 7 [195, 198]. In addition, the requirement for partially-miscible liquids which demix at experimentally accessible temperatures limits the fluid combinations available for bijel production [199, 200].

Some alternative methods for bijel production have been developed which have broadened the range of useable bijel materials and have the potential for scale-up. One example of this is solvent transfer-induced phase separation (STRIPS) [201]. Here two immiscible liquids become miscible in the presence of a third solvent, producing a ternary mixture. The third solvent is then extracted, causing the immiscible liquids to phase separate and producing a bicontinuous structure which is stabilised by solid particles. Another alternative method is bijel formation via direct mixing in which immiscible liquids can be used and a two-step mixing process with a combination of both solid particles and surfactants is employed to produce the bicontinuous structure [202]. In both of these cases, there is a requirement for the addition of surfactants and STRIPS still requires phase separation via spinodal decomposition, meaning again the two liquids must be carefully chosen.

In this chapter preliminary results on the production of bicontinuous structures via freeze-thaw cycling of emulsions are presented. In this way, neither neutrally wetting particles nor partially miscible liquids are required as continuous phase freezing is used to cause partial coalescence of droplets, leading to bicontinuous structure formation. In addition, this technique is suited to conveyor-belt style heating and cooling which is relevant for industrial processes such as those discussed in Chapter 6.

8.2 Materials and methods

Emulsions were prepared as described in Chapter 3 and characterised as described in Chapter 7. Samples were subjected to uniform freeze-thaw cycles at 4 °C/min as described in Chapter 7.

8.2.1 Region growing

To determine the number and size of connected regions in an image stack, the oil fluorescence channel from the confocal image stack was extracted and the slices with good signal-to-noise ratio duplicated. The 'Find connected regions' plugin was then used with the relevant minimum threshold value depending on the intensity histogram of the image. A minimum region volume of 5 points was used in order to eliminate background noise from the counting process. The number of regions and associated number of pixels per region was then exported into a spreadsheet. The number of pixels per region was then expressed as a fraction of the total number of pixels in the image to give an indication of the relative sizes of the regions. This calculation also gives the number of oil regions within the field of view. To determine the number of water regions in the selected volume, the image stack was 'inverted' such that the bright oil pixels became dark and the dark water pixels became bright and the process was then repeated.

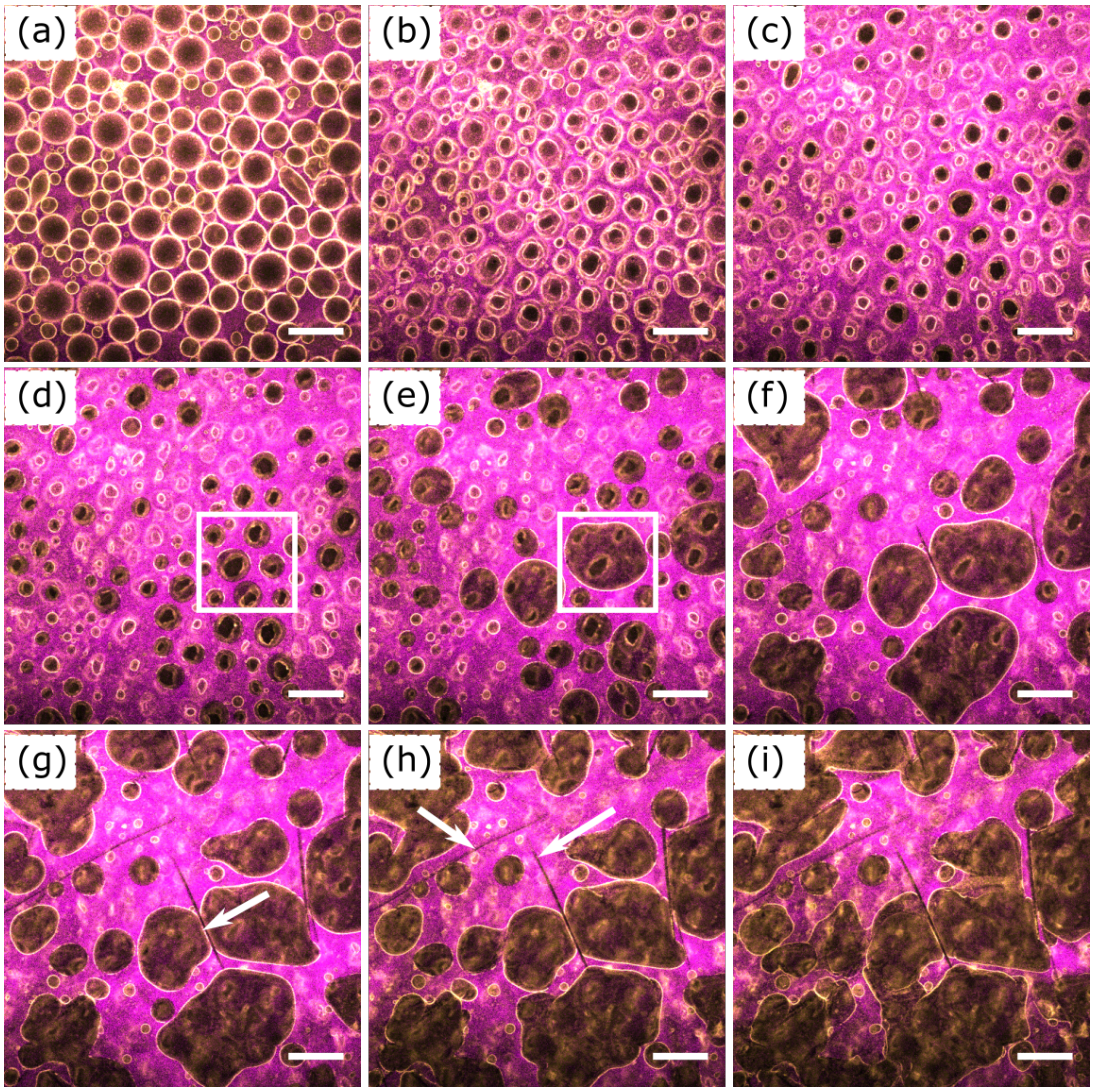

Figure 8.2 *Confocal images of a 47.1 µm droplet emulsion freezing under uniform conditions at 4 °C/min. Images are spaced 12.48 s apart. (a)-(c) emulsion droplets crumple during freezing as observed in other uniformly frozen samples. (d)-(i) some droplets appear to expand and partially coalesce such as those in the white box in (d)-(e). Crystallisation is not clearly observed via fluorescence, but the edges of crystals can be seen growing in panels (g)-(h) shown by the white arrows. Scale bars: 100 µm.*

8.3 Results and discussion

8.3.1 Freeze-thaw cycling

An emulsion sample, with an average droplet diameter of 47.1 μm (Sauter mean), was subjected to a freeze-thaw cycle at a cooling rate of 4 °C/min. Figure 8.2 shows a time series of images taken during sample cooling. As the sample starts to freeze (panels (b)-(c)), the droplets begin to crumple in the same manner as observed for uniform cooling previously (see Chapter 7 Fig. 7.5). However, instead of becoming trapped in crystalline oil while in a crumpled state, the apparent growth of droplets can be observed via the particle signal (yellow), leading to partial coalescence of multiple droplets, as seen in panels (d)-(i). This produces larger water domains as the oil becomes completely frozen.

Despite the fact that this is uniform cooling, the oil does not appear to crystallise across the field of view within 1-2 frames, as has been previously observed. In addition, crystal formation here cannot be directly observed via the loss of oil fluorescent signal until later in the freeze cycle. Even then only sharp, dark lines can be seen, shown by arrows in Fig 8.2(i)-(j), rather than complete crystal outlines.

Fig. 8.3 shows that as the sample thaws, there is further movement of the partially coalesced droplets and in panels (d)-(e) water 'channels' narrow in places (cyan dashed box) and pinch-off in other places (white box) . This takes the sample from water and oil-rich 'patches' to structures which look more like water channels.

Figure 8.4 shows the post-thaw structure of two separate samples after undergoing freeze-thaw cycles under the same experimental conditions. Both cases display bicontinuous structures with separate water and oil channels rather than individual water droplets in a continuous oil phase. These are similar to the structures observed during bijel formation via spinodal decomposition [192, 198].

8.3.2 Region growing

It should be noted that although these experiments were carried out in the uniform freezing setup, sample uniformity was not achieved here and the bicontinuous structures were present only in selected areas of the sample. Using

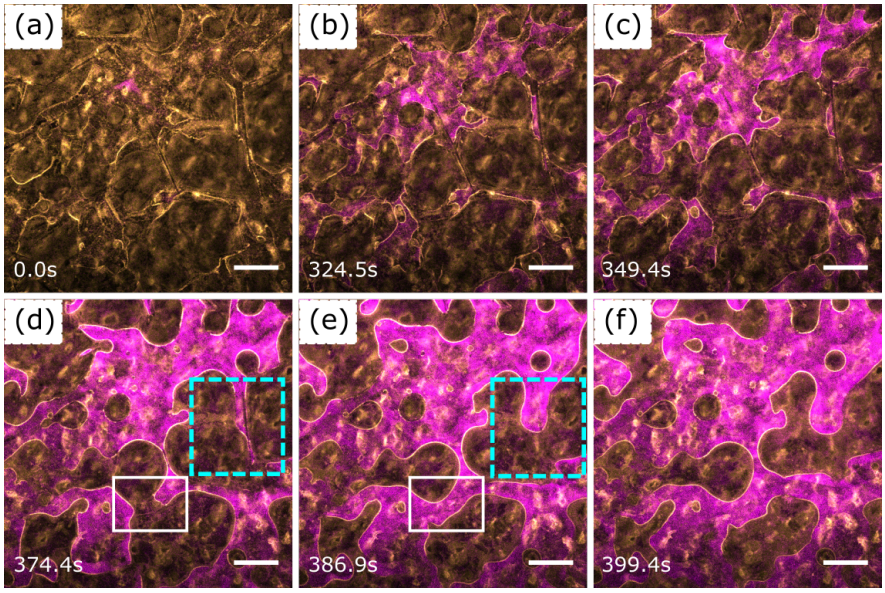

Figure 8.3 *Confocal images of the emulsion thawing at 4 °C/min. As the emulsion thaws, some of the partially coalesced droplets break up via pinch-off at the necks between them (see white box in (d)-(e)), some channels narrow but don't break (see cyan dashed box in (d)-(e)) while others remain connected. Images taken at selected time points with t=0 the time the thaw cycle begins. Scale bar: 100 µm.*

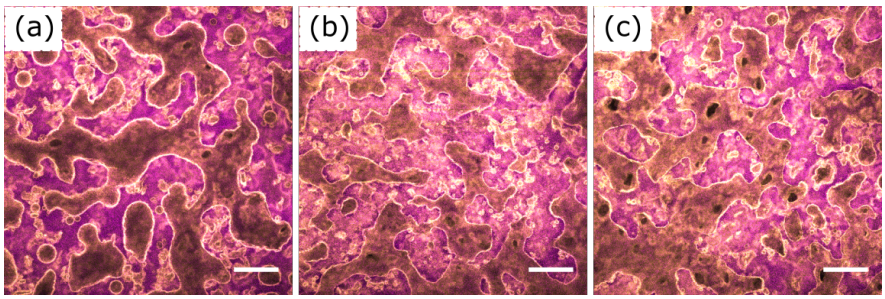

Figure 8.4 *Confocal images showing bicontinuous structure in emulsion samples after a single 4 °C/min freeze-thaw cycle. The brighter magenta regions are oil domains, while the darker or more yellow regions are water and the interface is stabilised by particles (yellow). (a)-(b) Images of the sample shown in Fig. 8.3. (c) Image of a second sample taken from the same stock emulsion but thermally cycled in a separate experiment. Scale bars: 100 µm.*

confocal microscopy it is also difficult to see how far this bicontinuity penetrates into the sample. However, using region growing can give a quantitative indication of the difference between the initial emulsion and the final structure.

Using a pre-freeze 4-image z-stack (depth of 12 μm) of the emulsion, assuming the smallest measurable droplet to be 10 μm in diameter based on visual observations, the number of droplets calculated via region growing was found to be 168. The total fraction of the image containing droplets was determined to be 27%, although this will be lower than the true value as, due to thresholding issues, many of the pixels towards the outer edges of each droplet were not counted in the droplet volume. The original image and the regions detected are shown in Fig. 8.5(a) and (b) respectively. In (b), water regions are shown in colour, oil regions in black. There was one primary oil region detected, accounting for a volume fraction of 44% of the total. Only one other region of significance was found and this accounted for $< 1\%$ of the total volume. Thus it can be said that, as expected, prior to freezing, the oil is continuous while the water is found in individual droplets.

The same analysis was then applied to a 5-image post-thaw z-stack (depth of 15.1 μm). The original image and the regions detected are shown in Fig. 8.5(c)-(d). Again in (d), water regions are shown in colour, oil regions in black. In this case, two significant oil regions were found, one with a fraction of 52% of the total volume and one at 2% of the total volume. Given that the oil is primarily found in one connected region, it can again be said that the oil is continuous, as in the initial emulsion. Upon measuring the number of water regions, 11 regions were found with volumes larger than a 10 μm droplet and of those, each contained $<$ 2% of the total volume except one which contained 33 % of the total volume. This is vastly different to the initial emulsion as instead of many water regions (droplets) there is now one primary water region through the volume. From this it can be concluded that, given the measured volumes of water and oil are similar before and after freeze-thaw cycling, the structure is now bicontinuous.

Although this analysis is only carried out over a limited sample depth due to poor image resolution deeper into the sample, it does confirm that there is some bi-continuity not just in the x-y plane, but also in the z-direction after a freeze-thaw cycle.

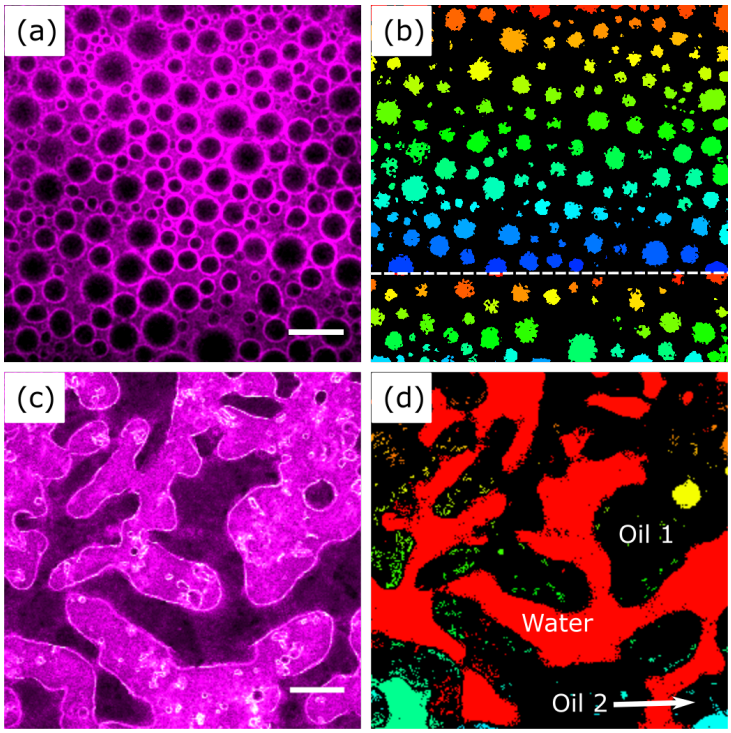

Figure 8.5 *(a) Confocal image of an emulsion oil(magenta) fluorescence channel before freeze-thaw cycling. (b) Water regions found from image (a) where the different colours represent different (unconnected) regions. The dashed white line represents the position at which the original image was split for analysis due to contrast/brightness differences between the two regions. (c) Confocal image of the final thawed emulsion structure. (d) Water regions found from image (c). Colours indicate connected regions with the red region containing most of the water in the image. Scale bars: 100 μm.*

8.3.3 Discussion

The appearance of (at least partial) bicontinuity in these samples is unlike the behaviour observed in Chapter 7 and therefore some explanation is required as to the mechanism by which these structures form. The first difference observed in this experiment compared to others is the difference in oil crystallisation. The slower loss of fluorescence in crystal formation observed here indicates that the crystals forming are likely to be more plate-like than needle-like. The plate-like nature of the crystal growth could mean that rather than individual droplets being trapped in a 'cage' of oil crystal, the droplets are squeezed between the crystal plate and the bottom of the glass cuvette, hence the appearance of droplet 'expansion' in the x-y plane may in fact be a result of compression in the z-direction, as has been observed by Maurice *et. al.* during centrifugal compression of particle-stabilised emulsions [35] and by Ferri *et. al.* during scanning force microscopy [203]. In the process, any liquid oil is also squeezed out from between the droplets and they are forced into close contact.

As the droplets deform, the interfacial area increases, thus the particle layer on the droplet will unjam, potentially leaving regions of bare interface on the droplet. If droplets close together are squeezed and come into contact with one another, there is now no mechanical barrier to (partial) coalescence, and this behaviour is observed during the freeze cycle, see Fig. 8.2(e)-(i).

As the oil thaws, the pressure exerted on the droplets by the crystals is relieved, allowing the partially coalesced droplets to relax. As discussed in Chapter 7, complete coalescence cannot occur unless the surface coverage of particles is low enough. The droplets will relax towards spherical until the particles jam, at which point the coalescence will be arrested. The pinch-off observed may be a result either of the decreasing interfacial area [191] or of fluid flow in the sample, such as that observed in simulations in Chapter 4, forcing different parts of a water channel in different directions. The behaviour here is different to the emulsion freezing experiments discussed in Chapter 7 in which the sample structure was observed to undergo only minor changes upon thaw. In this case, the structure has not been locked in during freezing, indicating that the particles were not jammed on the interface until later in time, allowing more rearrangement of the sample structure.

This process is shown schematically in Fig. 8.6. Initially, droplets are close

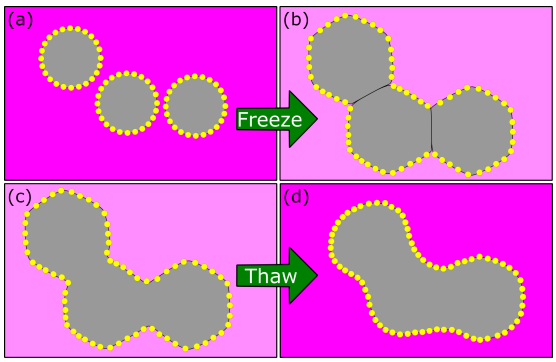

Figure 8.6 *Schematic of suggested bijel formation mechanism. Particles are shown in blue and droplet outlines in black. (a) Three droplets in close proximity before sample freezes. (b) As the oil surrounding the droplets begins to freeze, the droplets expand in the x-y plane, thus increasing the surface area and decreasing particle coverage. This results in droplets being squeezed together, while particles move out of the contact region. (c) The thin film between the droplets is ruptured in the absence of particles and the droplets partially coalesce. (d) As the sample thaws, the droplets begin to relax until the particles rejam on the interface and further relaxation is halted.*

together, but not in contact, as shown in panel (a). As the continuous phase freezes, the droplets are squeezed from above by the oil crystals, causing them to expand and come into contact. The particles on the interface migrate away from the contact region, leaving only bare interface and a thin film between the droplets, shown in panel (b). This thin film ruptures and the droplets partially coalesce, but the continuous phase freezes shortly thereafter, thus their configuration does not change, shown in panel (c). Finally as the oil thaws, the now-coalesced droplets begin to relax and do so until the particles are again jammed at the interface, shown in panel (d). Although only 3 droplets are shown in the schematic, this process occurs with many more droplets in similar contact, forming a particle-stabilised water channel. The configuration of the droplet-droplet contact is also important here, as droplets in certain configurations will not form channels, but instead would form larger, anisotropic water droplets rather than channels.

We have previously made bijel structures with a different batch of particles using a similar route, however further repeatability has been a major issue. Repeating these results with emulsion samples prepared at a later date did not produce any bicontinuity, even with similar average droplet sizes and under the same freeze-thaw conditions to the emulsion used here. The reasons for this are currently

unknown as it is unclear which parameters are the most important to control in order to achieve bicontinuity. Given that bicontinous structures have only been observed at one particular droplet size and cooling rate, it could be expected that both of these parameters are important, but other important factors have not yet been determined. As such, bijel formation via freeze-thaw cycling does seem to be a promising technique, though the parameters determining the outcome are as yet unclear. Given that simulations of bijel formation have previously been carried out [191, 204], and that simulation of the temperature profile through a sample cell is achievable (see Chapter 4), it is possible that simulations could be used to explore potentially relevant parameters.

8.4 Conclusions and future work

In this chapter, we have shown the potential of using freeze-thaw cycling as a route to producing bicontinuous structures. Both freezing and thawing steps are required to produce bicontinuity as the sample structure is not fixed after the freezing stage alone, but evolves further as the sample thaws, suggesting that the particles are not jammed at the interface until after thawing. This technique is currently in the early stages of development and the relevant control parameters for reproducibly achieving bicontinuous structures have not yet been elucidated.

In further work it would be important to determine the key parameters to tune in order to produce bicontinous structures, whether this be initial droplet size and concentration, cooling rate or a combination of them as is the most likely case given that so far bijels have only been observed in one particular combination. It would also be useful to understand more clearly how the bijel forms so that it could be extended to larger areas of a sample. Were it to be refined and repeatable, this has the potential to be an easier route than the spinodal decomposition for producing bijels, and it could also allow the use of liquid-liquid combinations not currently achievable. Finally, as experiments have proved challenging, the use of computer simulation could be valuable here in order to reveal some of the key parameters.

Chapter 9

Conclusions and outlook

In this thesis, a model water-in-oil Pickering emulsion has been used to study the stability of Pickering emulsions to freeze-thaw cycles of the continuous phase. Both individual and collective droplet effects have been studied under uniform and non-uniform cooling, as well as freezing via a solidification front.

In Chapter 4, simulations of the thermal behaviour of the oil throughout samples cooled uniformly and non-uniformly are presented. These results also provide insight into the fluid flow profile in the experimental setups used in other parts of the thesis. Following on from that, the temperature profile of the oil was studied experimentally along with the crystal growth mechanisms in the oil. Combined, the simulations and experiments show that the uniformity of the temperature and the presence of a temperature gradient through a sample can vastly affect both the fluid flow and the crystal growth within the oil. Scaling up the sample size in both experiment and simulation would show how sample size affects the strength of the temperature gradient and more easily allow comparison to consumer or industrial-scale product sizes. In addition, exploring a wider range of cooling rates, including flash freezing, could give more insight into the optimal way to freeze with limited sample damage.

In Chapter 5, a dilute emulsion is used to explore the behaviour of non-interacting, single particle-stabilised droplets in a freezing continuous phase. Here the droplets interact only with the oil crystals growing around them and not any other droplets. In each case, the droplet shape changes during freezing as it is trapped by growing oil crystals, with the shape controlled by the angle at which the crystals meet the droplet. As droplets are deformed during freeze, the surface

area increases, allowing particles on the interface to unjam. During thaw, the droplets are released from the oil crystals but do not return to a smooth sphere as the particles jam at a lower packing fraction than initially, allowing a larger surface area to be covered when relaxation is arrested. These shape changes have been characterised by a 'non-smooth-circular' number which takes into account both the overall shape of the droplet and the wrinkled nature of the surface. Calculation of this number before and after freeze-thaw cycling shows that on average droplets become less smooth-circular as a result of the cycle.

Following on from the single droplet experiments in Chapter 5, it became clear that a controlled solidifcation front where crystal growth was unidirectional would be a useful method of studying droplet-crystal interaction. It could give a higher level of control over the crystal-droplet interaction and also allowed separate control over the temperature gradient and crystal growth velocity. This is the focus of Chapter 6. As a droplet is trapped by the freezing front, initially only part of the droplet is trapped, while the free portion of the droplet is stretched ahead of the front. Depending on the temperature gradient and front velocity, droplets were either held and progressively trapped, or split with part of the droplet being trapped and the rest a completely free droplet with a lower surface coverage of particles. This shows the importance of the interaction between the crystals and the stabilising particles as experiments carried out on surfactant-stabilised droplets did not display this behaviour [153]. Further work at a higher resolution would aid in this understanding as it would show the behaviour of droplets at the particle level rather than droplet level only.

In Chapter 7 the collective behaviour of emulsion droplets during freeze-thaw cycling was studied. Undiluted emulsions were subjected to freeze-thaw cycling of the continuous phase, and the resultant behaviour of the emulsions depended on the freezing conditions. In particular, whether the freezing is uniform or non-uniform has a large impact on the final emulsion structure. Non-uniform cooling leads to non-uniformity in the sample structure and also produces regions of foam-like structure. This is due to oil crystals growing into liquid regions of the sample and pushing droplets together into the remaining unfrozen regions. Uniform cooling produces uniform structures with wrinkled droplets, some of which are partially coalesced. This behaviour is independent of droplet size and cooling rate. Here the oil surrounding each droplet freezes rapidly, meaning the droplets are unable to move but deform to fit in the crystalline cage around them. In both cases, the unjamming and rejamming of particles at the interface

throughout the process is responsible for the droplet behaviour as this is not observed in surfactant stabilised emulsions treated in the same manner.

Finally in Chapter 8 the use of freeze-thaw cycling to produce bicontinous structures is explored. Experiments carried out on emulsions under uniform cooling have shown that it is possible to produce regions of bicontinuity via freeze-thaw cycling. This was achieved at only one specific cooling rate and droplet size, but was repeated. The structure forms as droplets are pushed close together and compressed from above such that there are regions of bare interface on the droplets' surfaces. When bare interface from two droplets come into contact, the droplets partially coalesce and when multiple droplets are connected in this manner, water channels are formed. The control parameters for this process have not yet been elucidated and so further work is required to determine the correct protocol to obtain bicontinuous structures repeatably. This would have industrial relevance and also avoid some of the problems with traditional bijel formation.

As a whole, this thesis has explored microscopic aspects of the freeze-thaw stability of Pickering emulsions, in particular the role the interfacial particles play in determining the droplet/emulsion behaviour and structure. Two main themes have emerged from the results: firstly, the effect of particles on the interaction between droplets and growing crystals and secondly, the behaviour of the particles on the droplet interface itself. The presence of particles can lead to permanent damage of emulsion structure, in particular of droplet shape, as the presence of particles prevents droplets from relaxing to spherical after distortion. Particles also alter the way droplets are trapped or engulfed by growing crystals as they present anchors by which the droplet is trapped into the crystal, enhancing the droplet distortion as it is trapped. Particle jamming on the interface, in particular the ability of particles to unjam upon interface expansion and later rejam at a different packing fraction, is one of the biggest factors in the ultimate shape of the droplets as similar behaviour was not observed on droplets where particles were depleted or replaced with surfactants.

The industrial applications of both Pickering stabilisation and freeze-thaw cycling are clear, but the combination of the two must be treated with care in order to ensure that the advantages of Pickering stabilisation do not in fact become a hindrance in the stabilisation of undesirable microstructures produced when freeze-thaw cycling is used.

Appendix A

Freezing front formation

This appendix contains an explanation for the structure of the solidification front observed in Chapter 6. In Section 6.3 of that chapter, we suggested that the solidification front should be planar as this had been achieved in previous experiments within the Deville group [153] using the same experimental setup, however this was not observed in our experiments. Here we give some possible reasons for the difference in the solidification front structure.

Experimental observations of the solidification front

It is clear that compared to the freezing in Chapter 5, the interaction between crystal and droplet is more unidirectional. There are no large crystal spears to pierce and widen in droplets, instead there is a front of crystals which reach the droplet in unison. There is a defined direction of crystallisation, rather than oil crystals approaching droplets from several directions simultaneously. However, the interface is not observed to be planar, but displays two crystal types which appear either alone or combined, as shown in Figure A.1. In some cases, as shown in panel (a), the front was made up of broad, cellular or faceted crystals producing an uneven front edge with a few gaps in between the crystals. In other cases, as shown in panel (b), the crystals were dendritic, made up of many smaller more spiked crystals containing many small gaps in between the crystal spikes. It is also possible to obtain fronts where there are both faceted crystals and dendritic crystals, shown in panel (c). Typically higher velocities produced the dendritic fronts and lower velocities the faceted fronts.

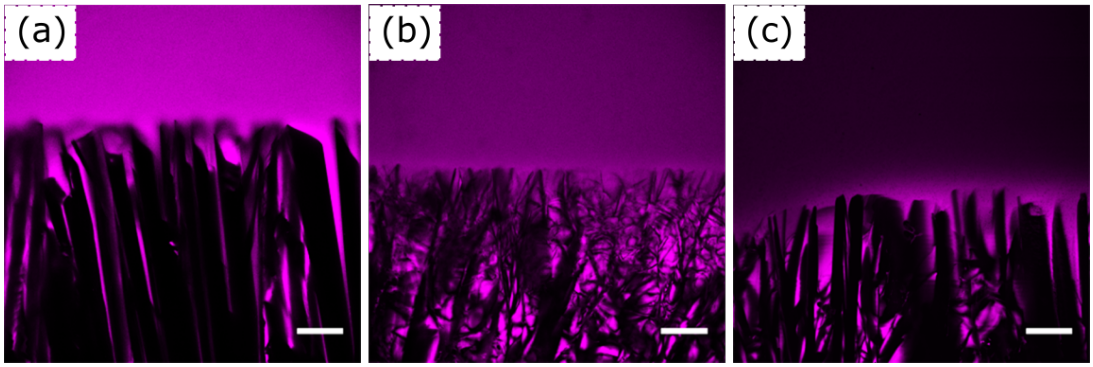

Figure A.1 *Confocal images of the different freezing front structures observed during experiments. Liquid oil is magenta, while frozen oil is black. (a) Cellular, (b) Dendritic and (c) a combination of (a) and (b). Note that in (c) the image contrast is poor and as such liquid oil ahead of the front also appears dark.*

Interface structure

One reason for the difference in structures observed here may be the difference in sample composition. In experiments by Dedovets *et. al.*, non-planar fronts were observed at selected velocities, but only close to the solid-liquid interface [153]. However, those experiments were carried out with a water-continuous emulsion, whereas here a hexadecane-continuous emulsion is used. Although it is possible that this behaviour is due to experimental conditions, such as the grease in the sample cell providing a rough surface for crystal nucleation, literature on solidification fronts provides us with an alternative explanation.

Solid interfaces growing from a melt can be described simply as atomically smooth (faceted) or atomically rough (non-faceted) [205]. An atomically smooth interface is very dependent on the experimental conditions and thus will easily depart from planar. Atomically rough interfaces more easily allow the addition of atoms of varying crystal orientations, thus are more stable and more easily remain planar. Further details can be found in Reference 205.

These two interfaces can be distinguished using the 'interfacial α-factor' defined by Jackson in 1959 as [206]

$$\alpha = (\frac{L}{RT_{\mathrm{E}}})\xi \ , \tag{A.1}$$

where L is the difference between internal energies of the two phases (here the

latent heat of fusion), R the gas constant, T_{E} the equilibrium temperature of the two phases (here the melting temperature) and ξ a constant factor accounting for the underlying crystal structure and the crystal orientation at the interface, taking a value between $\frac{1}{4}$ and 1 [205, 207]. The $(\frac{L}{RT_{\mathrm{E}}})$ term is the dimensionless entropy of melting. For non-faceted growth, $\alpha < 1$ and for faceted growth typically, $\alpha > 2$ [205].

For water $\alpha < 1$ and thus water is atomically rough, making it suitable for directional freezing because it easily grows with a planar interface . For hexadecane, taking $L = 235.6\mathrm{J/g} = 53.36$ kJ/mol [26, 122] and $T_{\mathrm{E}} = 291$ K with $R = 8.314$ J/mol K gives an entropy of melting of 22.1. Given the limits on ξ, this leads to a value of $\alpha > 1$, showing that hexadecane is likely to develop a faceted interface. This means that the shape of the interface will depend strongly on the experimental conditions.

Constitutional supercooling

As discussed in Chapter 2, supercooling of a fluid is commonly required before crystal nucleation can occur. At a solid-liquid interface, this may be enhanced by the rejection of solutes from the frozen fluid leading to a depression of the freezing point ahead of the front. This is known as 'constitutional supercooling' [208]. Any fluctuations at the interface can then lead to the growth of crystals out of the plane and into the supercooled region, causing further solidification. This has been shown to produce both dendritic and faceted crystal growth depending on factors such as solute concentration and front velocity [208, 209]

In the system used in our experiments, the only solute used in the oil is the Nile red fluorescent dye, but given the reduced fluorescence upon the oil freezing, it is possible that there is an increased concentration of the solute ahead of the front. It is therefore possible that the front behaviour observed in experiments is a result of this effect, especially given that the nature of the hexadecane crystallisation makes the interface strongly dependent on the experimental conditions.

It has also been suggested that the presence of colloidal particles could affect this instability [210, 211] and given the presence of the particle-stabilised droplets in our experiments, it is possible they could have a similar effect. However, it is also possible that this effect is small in comparison to effects caused by solute concentration [212].

Appendix B

Interfacial rheology of particle-coated liquid-liquid interfaces

As discussed in Chapter 2, interfacial rheology is a useful technique for probing the viscous and elastic properties of an interface under shear. The behaviour of a flat interface can be directly linked to the behaviour of particles on the surface of an emulsion droplet [51] and thus probing flat interface behaviour can give indications as to the stability of particle-stabilised emulsions.

Our aim in carrying out interfacial rheology was to observe the behaviour of a flat, particle-laden, water-oil interface containing the same components as those used in our emulsions, *i.e.*water, hexadecane and PMMA particles. This could then provide insight into the behaviour of the droplets during freezing as the interaction between an oil crystal and a droplet could be considered at least in some cases as a shear deformation of the droplet interface.

For reasons which will be discussed in this chapter, mainly the dominance of the instrument response over the interface behaviour, the results of these experiments yielded little information about the behaviour of the particle-laden interface. Instead, much of the observed behaviour is attributed to the nature of the experimental setup, thus the results cannot be related directly to the rest of the research presented in this thesis. However, these results do provide more technical information which may be valuable to those wishing to carry out similar

experiments with this system. Hence the details of the experimental setup and the results are included here.

B.1 Materials and methods

B.1.1 Materials

Water and hexadecane were treated as described in Chapter 3 but no fluorescent dye was added to the oil. The particles used were NBD-dyed PMMA particles described in Chapter 3 stored dried rather than in hexadecane. To spread particles at the water-oil interface, a dispersion of particles was required, thus a mass of 0.021g of dried particles was added to 1.65g of hexane. The dispersion was placed in the sonic bath for a minimum of 30 minutes to break up any aggregates.

B.1.2 Experimental setup

A stress-controlled rheometer (DHR-2, TA Instruments) was used with the related software (TRIOS) for all the rheology experiments. A double-wall ring (DWR) geometry (TA Instruments, part no. 545950.001) was used, a schematic of which is shown in Fig. B.1(a). The platinum-iridium ring sits at the liquid-liquid interface, both applying the stress directly to the interface and measuring the response of the interface to that applied stress. A Teflon trough is used to contain the sample and this trough is designed with a step on both inner walls to pin the interface. This leads to a flat interface with no meniscus effects as the interface pins both to this step and to the edge of the DWR. The trough used in these experiments also has a glass window in the base to allow for sample imaging.

In order to observe the particle behaviour at the interface and to understand how the configuration of particles on the interface corresponds to the rheological response, a custom-built imaging module was used. A schematic is shown in Figure B.1(c). It is used with a $10\times/0.3$ NA objective, a variable wavelength light source (CoolLED precisExcite), USB-camera(Allied Vision Technologies) and connected to RheoImager software designed in house to allow image capture and storage. The module is aligned with the glass window in the sample trough

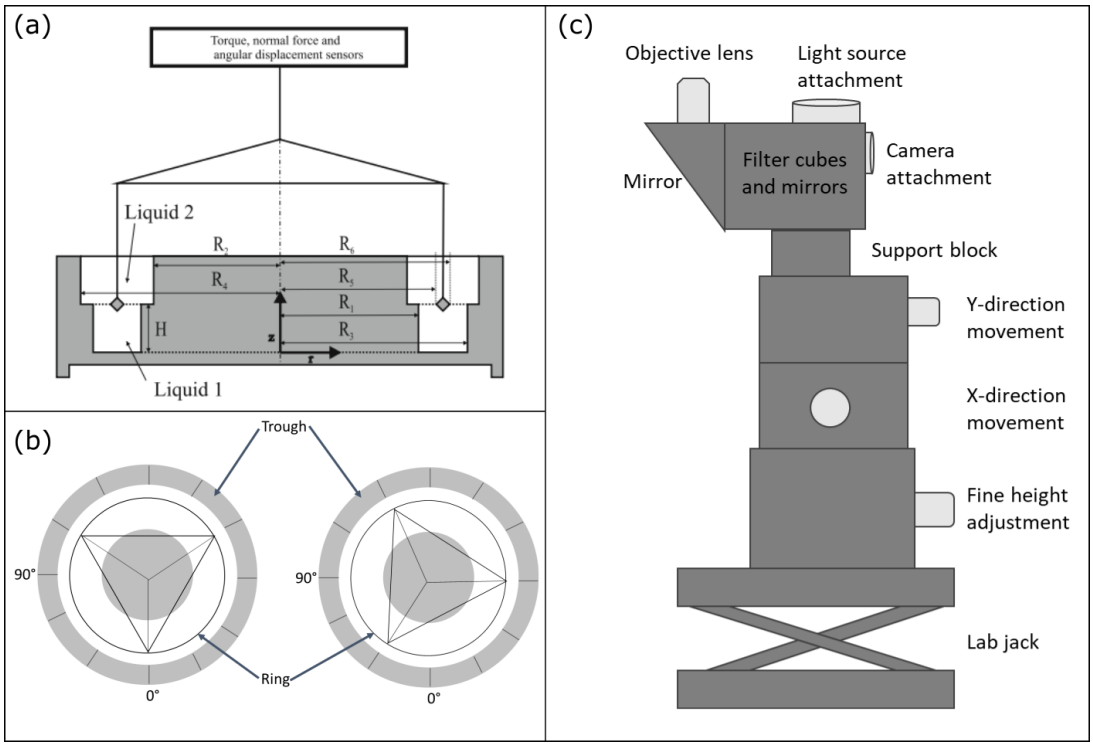

Figure B.1 *(a) Schematic of the double wall ring geometry. Image used with permission from Reference 213. (b) Schematic of the double wall ring as viewed from above with the ring supports at two different angular positions, i.e. the ring is rotated 30 ° clockwise between the two overhead schematics. (c) Schematic of the imaging module used for observing the behaviour of particles at the water-oil interface.*

and appropriate light wavelengths and filter cubes are used to excite and detect the fluorescence from the particles.

B.1.3 Sample preparation

A volume of 7 ml of water was loaded into the trough using a pipette and then excess water was removed until the water was pinned to the step in the trough (at a volume of around 4.5 ml). The DWR is lowered to the interface until it is pinned. Then 10 ml of hexadecane was added using a pipette and a second pipette was then used to spread 1 ml of particle dispersion evenly over the surface of the oil. The sample was left for at least 30 minutes in order to allow the particles to reach the interface and the hexane to evaporate. The surface coverage could be ascertained using the imaging module so if coverage appeared low, the sample was left for a further 30 minutes to allow more time for particles to reach the interface.

B.1.4 Creep-recovery experiments

The relevant calibrations set by the software were carried out prior to any experiments to correct for intertia, friction and the rotational profile of the system. High precision rotational mapping was also carried out. After adding the water phase, a flow peak hold test (constant applied stress for a fixed duration) was run at a fixed stress value of 2×10^{-4} Pa m with the ring at a bare water-air interface. This allowed the measurement of ring velocity vs angular displacement and was used to check the ring was correctly attached and not distorted. Any distortions in the ring shape would lead to periodic variations in the ring velocity.

Creep-recovery experiments were then carried out by a two step process: First, a Step(transient) creep experiment, in which a fixed stress is instantaneously applied to the sample, is run for a duration of 180 s and then a Step(transient) creep experiment is run at zero applied stress for 180 s (recovery). The applied stress was increased from 0.01 mPa m up to the yield stress of the interface (typically around 0.07 mPa m) increasing in intervals of 0.01 mPa m. During each run, the values of applied torque and ring displacement were recorded and thus the strain on the interface could be calculated by multiplying the displacement by the strain constant calculated by the software to have a value of 9.39276 1/rad.

B.2 Results and discussion

B.2.1 Creep-recovery rheology

Figure B.2(a) shows a typical set of strain response curves for creep-recovery experiments at increasing values of applied stress. Except for the highest stress and the first of the lowest stress curves, the curves are all similar in shape with oscillations during both creep and recovery being damped out over time. Increasing the applied stress results in an increase in the magnitude of these oscillations until at the highest applied stress the interface yields, thus the DWR rotates continuously and no recovery is observed.

The oscillatory behaviour is indicative of elasticity in the system and is known as 'creep ringing,' a phenomenon which results from the coupling of the inertia of the instrument to the elasticity of the sample [51, 214]. This effect is also observed at a bare water-oil interface, as shown in Fig. B.2(b), where the oscillations are the same order of magnitude as those at the particle-coated interface. This is surprising as the water-oil interface is not expected show show any shear elasticity. This point will be discussed later.

Van Hooghten *et. al.* have shown that the combined effect of the compliance of the ring and the subphase drag can be accounted for by subtracting the measured modulus (ratio of stress to strain) of the bare interface from that of the particle-coated interface [51]. The modulus is calculated by finding the gradient of the stress-strain curve using a least-squares fit and the strain values used were taken to be the average equilibrium value of the creep curve after oscillations have damped out. In these experiments the modulus of the bare interface was determined to be 0.069(1) mPa m while the modulus of the particle-coated interface was determined to be 0.0494(5) mPa m, *i.e.* the bare modulus is higher than that particle-coated interface. This therefore does not allow us to correct the particle-coated interface data as to do so would lead to a negative interfacial modulus. It also suggests that there may be other effects present here which dominate the measured strain values over any response from the interface.

The presence of other effects is supported by the different measured response to the first experiment at the lowest applied stress compared to subsequent runs at the same applied stress, as can be seen in Fig. B.2(a) where the first (green) curve measured at 0.01 mPa m does not overlap the blue and black curves for

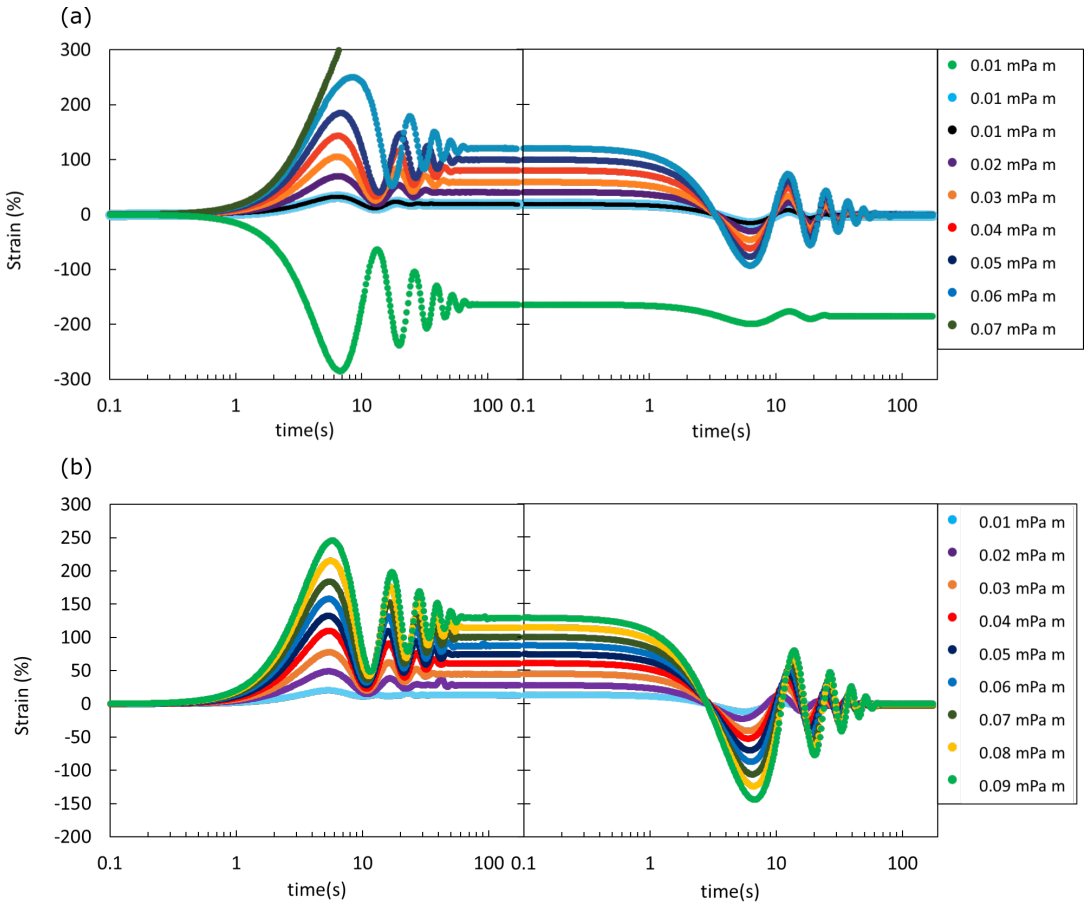

Figure B.2 *(a) Strain response to creep-recovery experiments on a PMMA-coated water-hecadecane interface for increasing values of applied stress. Black curve has a smaller marker size to provide visibility of the blue curve which is closely overlaps. (b) Strain response to creep-recovery experiments at a bare water-oil interface.*

the same stress. Similar behaviour was observed at the bare interface but has not been included here. Similar behaviour has been observed with a particle-laden interface in a Langmuir trough [51], but here the effect is also present at a bare interface. These results suggest that there may be some response of the rheometer itself which is affecting the results. It is possible that the ring might have a preferred resting position/orientation in the rheometer to which it preferentially returns after a stress is applied and released. This could show up as elasticity in the interface and would appear recoverable if the ring begins a cycle at that preferred position. It would also explain the differing behaviour on the first run: during the first run, the ring begins at a 'non-preferred' orientation and therefore during the run rotates towards the preferred orientation. After this, the ring returns to that same orientation at the end of each experiment (denoted by the 'recovery' to zero strain) and thus in subsequent runs always begins at the same preferred orientation.

In order to test this, flow (peak hold) measurements were carried out both at a bare water-hexadecane interface and freely in air with a shear rate of zero. This meant that during the experiment, the ring simply rotated freely. The displacement of the ring was recorded as a function of time until the ring velocity was too small to be recorded. The rheometer trough was marked at 30 ° intervals for reference as shown schematically in Fig. B.1(b). For the first run the ring was set at the position shown on the left in Fig. B.1(b) and held in position using the 'padlock' button on the rheometer. After the run is finished, the start position of the ring was manually rotated 30 ° clockwise and the experiment repeated at successive 30 ° intervals until the starting orientation had rotated a full 360 °.

The results of the experiment are shown in Fig. B.3 for experiments at a water-oil interface (panel (a)) and in air (panel (b)). As the starting angle increases relative to the initial reference position, the displacement vs time curves change in shape. There appear to be three 'preferred' positions to which the ring comes to rest. At which the ring comes to rest appears to depend on which is closest to the ring start position. Similar results were obtained for a second ring of the same type which was tested by the same experiments.

This could provide an explanation for the recovery from large strains observed in creep recovery measurements: When a stress is applied (creep), the ring moves away from the 'preferred' positions and so when the stress is removed (recovery), the ring will return to one of those positions. The particle-coated interface is weak and so this effect dominates over any response coming from the particles at

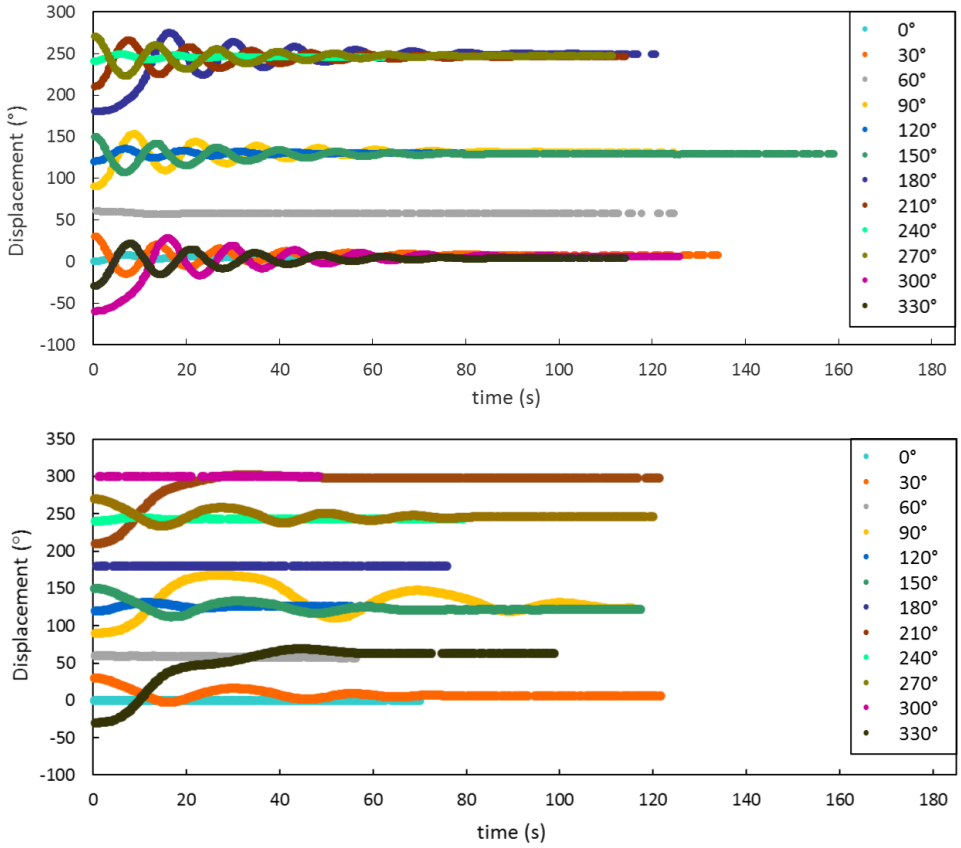

Figure B.3 *Displacement vs time curves for flow peak hold experiments with zero applied stress (a) at a water-hexadecane interface and (b) in air. The ring start position is rotated 30 ° clockwise between runs. (a) The ring appears to have three preferred positions at 0 °, 120 ° and 240 ° to which it returns except when starting at 60 °. (b) The ring has the same three preferred positions, but it also has 3 intermediate positions at 60 °, 180 ° and 300 ° where the ring shows very little movement the half-way points between the preferred positions observed in the water-oil interface experiment. In the runs at 210 ° and 330 °, the ring appears to have too much torque to settle at the closest preferred position and rotates past it to the next intermediate position.*

the interface.

The cause of this problem is currently unknown. The first suggested cause is that the ring itself causes the problem. This is backed up by the fact that that the three-fold preference observed aligns with with the three vertical supports connecting the ring to the shaft piece. The second suggestion is that the problem relates to the air bearing in the rheometer as oscillations in geometry displacement at zero stress have been observed by other users of the rheometer with different geometries. This has serious consequences for carrying out creep-recovery measurements as it leads to variation in the observed strain-time curves depending on the starting position of the ring, thus masking any behaviour resulting from the particles at the interface.

As experiments on similar systems with an alternative rheometer and a different ring have been carried out with more success by van Hooghten *et. al.* [51], this could suggest that using a different model of rheometer may go some way to solving the problems observed here. It is also possible that an alternative geometry, such as a bicone, may be more effective, however this also has a larger effects of drag and a higher moment of inertia, thus may not be as sensitive as the DWR for a weak interface [215]. Further research on these two themes could therefore be beneficial both for understanding the behaviour of the experimental setup and determining the response of the particle-coated interface to applied stress.

B.3 Conclusion

Interfacial rheology experiments of a particle-coated water-oil interface showed 'creep ringing' as a result of the coupling between the elasticity of the interface and the inertia of the sample. Results also showed that there is a strong effect of the instrument behaviour on the measured results and it was not clear how to correct for this. Further experiments on a bare interface suggest that the rheometer geometry has preferred orientations to which it will return when no stress is applied. They showed that the effect of particles at the interface was much weaker than the response of the rheometer and thus any effects of the particles were obscured.

Overall, it can be seen that in order to use interfacial rheology as a probe of the

interfacial properties of a weak interface, the choice of instrument and geometry may be crucial in determining whether any information about the sample can be extracted from the experiments.

Bibliography

[1] K. L. Dickinson, U. K. Wiegand, and J. H. J. Thijssen. Soft meets hard – how does freeze-thaw cycling affect the microstructure of particle-stabilised emulsions? *arXiv*, 2019.

[2] M. Doi. *Soft Matter Physics*. Oxford University Press, 2013.

[3] L. S. Hirst. *Fundamentals of Soft Matter Science*. CRC Press, 2012.

[4] G. Chen and G. He. Separation of water and oil from water-in-oil emulsion by freeze/thaw method. *Separation and Purification Technology*, 31(1): 83 – 89, 2003.

[5] A. Marefati, M. Rayner, A. Timgren, and P. Dejmek. Freezing and freeze-drying of pickering emulsions stabilized by starch granules. *Colloids and Surfaces, A: Physicochemical and Engineering Aspects*, 436: 512 – 520, 2013.

[6] M. Rayner. Current status on novel ways for stabilizing food dispersions by oleosins, particles and microgels. *Current Opinion in Food Science*, 3: 94 – 109, 2015.

[7] X.-F. Zhu, N. Zhang, W.-F. Lin, and C.-H. Tang. Freeze-thaw stability of pickering emulsions stabilized by soy and whey protein particles. *Food Hydrocolloids*, 69: 173 – 184, 2017.

[8] F. Leal-Calderon, J. Bibette, and V. Schmitt. *Emulsion Science*. Springer New York, 2007.

[9] M. E. Leunissen, A. van Blaaderen, A. D. Hollingsworth, M. T. Sullivan, and P. M. Chaikin. Electrostatics at the oil–water interface, stability, and order in emulsions and colloids. *Proc. Natl. Acad. Sci. U. S. A.*, 104: 2585–2590, 2007.

[10] R. J. G. Lopetinsky, J. H. Masliyah, and X. Zhenghe. Solids-stabilized emulsions:a review. In B. Binks and T. Horozov, editors, *Colloidal Particles at Liquid Interfaces*, pages 186–224. Cambridge University Press, Cambridge, 2006.

[11] L. L. Schramm. Interfacial energetics. In L. L. Schramm, editor, *Emulsions, Foams, Suspensions, and Aerosols*, pages 85–146. Wiley-Blackwell, 2014.

[12] H. Butt, K. Graf, and M. Kappl. *Liquid Surfaces*, pages 4–25. Wiley-Blackwell, 2004.

[13] J. Sjöblom, editor. *Emulsions and Emulsion Stability*, chapter An Experimental and Theoretical Aproach to the Dynamic Behavior of Emulsions. CRC Press, second edition, 2005.

[14] J.-C. Baret, F. Kleinschmidt, A. El Harrak, and A. D. Griffiths. Kinetic aspects of emulsion stabilization by surfactants: A microfluidic analysis. *Langmuir*, 25(11): 6088–6093, 2009.

[15] B. P. Binks, editor. *Modern Aspects of Emulsion Science*. The Royal Society of Chemistry, 1998.

[16] B. P. Binks. Particles as surfactants – similarities and differences. *Current Opinion in Colloid and Interface Science*, 7(12): 21 – 41, 2002.

[17] S. U. Pickering. Cxcvi.-emulsions. *Journal of the Chemical Society, Transactions*, 91: 2001–2021, 1907.

[18] W. Ramsden. Separation of solids in the surface-layers of solutions and 'suspensions' (observations on surface-membranes, bubbles, emulsions, and mechanical coagulation). – preliminary account. *Proceedings of the Royal Society*, 72: 156–164, 1903.

[19] C. C. Berton-Carabin and K. Schroën. Pickering emulsions for food applications: Background, trends, and challenges. *Annual Review of Food Science and Technology*, 6(1): 263–297, 2015.

[20] Y. Chevalier and M.-A. Bolzinger. Emulsions stabilized with solid nanoparticles: Pickering emulsions. *Colloids and Surfaces, A: Physicochemical and Engineering Aspects*, 439(0): 23 – 34, 2013.

[21] J. Wu and G.-H. Ma. Recent studies of pickering emulsions: Particles make the difference. *Small*, 12(34): 4633–4648, 2016.

[22] P. Finkle, H. D. Draper, and J. H. Hildebrand. The theory of emulsification 1. *Journal of the American Chemical Society*, 45(12): 2780–2788, 1923.

[23] R. Aveyard, B. P. Binks, and J. H. Clint. Emulsions stabilised solely by colloidal particles. *Advances in Colloid and Interface Science*, 100: 503 – 546, 2003.

[24] R. Aveyard and D. A. Haydon. Thermodynamic properties of aliphatic hydrocarbon/water interfaces. *Transactions of the Faraday Society*, 61: 2255–2261, 1965.

[25] A. Goebel and K. Lunkenheimer. Interfacial tension of the water/n-alkane interface. *Langmuir*, 13(2): 369–372, 1997.

[26] W. M. Haynes, editor. *Handbook of Chemistry and Physics*, page 2652. CRC Press, 97th edition, 2016.

[27] B. P. Binks and S. O. Lumsdon. Pickering emulsions stabilized by monodisperse latex particles: effects of particle size. *Langmuir*, 17(15): 4540–4547, 2001.

[28] B. P. Binks and S. O. Lumsdon. Stability of oil-in-water emulsions stabilised by silica particles. *Physical Chemistry Chemical Physics*, 1: 3007–3016, 1999.

[29] N. Ashby and B. Binks. Pickering emulsions stabilised by Laponite clay particles. *Physical Chemistry Chemical Physics*, 2(24): 5640–5646, 2000.

[30] A. Timgren, M. Rayner, M. Sjöö, and P. Dejmek. Starch particles for food based pickering emulsions. *Procedia Food Science*, 1: 95 – 103, 2011.

[31] D. Rousseau. Fat crystals and emulsions stability - a review. *Food Research International*, 33: 3–14, 2000.

[32] D. Rousseau. Trends in structuring edible emulsions with pickering fat crystals. *Current Opinion in Colloid and Interface Science*, 19(4), 2013.

[33] B. Madivala, S. Vandebril, J. Fransaer, and J. Vermant. Exploiting particle shape in solid stabilized emulsions. *Soft Matter*, 5: 1717–1727, 2009.

[34] J. W. J. de Folter, E. M. Hutter, S. I. R. Castillo, K. E. Klop, A. P. Philipse, and W. K. Kegel. Particle shape anisotropy in pickering emulsions: Cubes and peanuts. *Langmuir*, 30(4): 955–964, 2014.

[35] L. Maurice, R. A. Maguire, A. B. Schofield, M. E. Cates, P. S. Clegg, and J. H. J. Thijssen. Squeezing particle-stabilized emulsions into biliquid foams - equation of state. *Soft Matter*, 9: 7757–7765, 2013.

[36] S. Arditty, C. P. Whitby, B. P. Binks, V. Schmitt, and F. Leal-Calderon. Some general features of limited coalescence in solid-stabilized emulsions. *European Physical Journal E: Soft Matter*, 11(3): 273–281, 2003.

[37] R. Wiley. Limited coalescence of oil droplets in coarse oil-in-water emulsions. *Journal of Colloid Science*, 9(5): 427 – 437, 1954.

[38] M. Destribats, S. Gineste, E. Laurichesse, H. Tanner, F. Leal-Calderon, V. Héroguez, and V. Schmitt. Pickering emulsions: What are the main parameters determining the emulsion type and interfacial properties? *Langmuir*, 30(31): 9313–9326, 2014.

[39] E. Vignati, R. Piazza, and T. P. Lockhart. Pickering emulsions: interfacial tension, colloidal layer morphology, and trapped-particle motion. *Langmuir*, 19(17): 6650–6656, 2003.

[40] S. Tarimala and L. L. Dai. Structure of microparticles in solid-stabilized emulsions. *Langmuir*, 20(9): 3492–3494, 2004.

[41] D. E. Tambe and M. M. Sharma. Factors controlling the stability of colloid-stabilized emulsions: I. an experimental investigation. *Journal of Colloid and Interface Science*, 157(1): 244 – 253, 1993.

[42] A. B. Pawar, M. Caggioni, R. Ergun, R. W. Hartel, and P. T. Spicer. Arrested coalescence in pickering emulsions. *Soft Matter*, 7(17): 7710–7716, 2011.

[43] S. Tcholakova, N. D. Denkov, and A. Lips. Comparison of solid particles, globular proteins and surfactants as emulsifiers. *Phys. Chem. Chem. Phys.*, 10: 1608–1627, 2008.

[44] C. P. Whitby, H. K. Anwar, and J. Hughes. Destabilising pickering emulsions by drop flocculation and adhesion. *Journal of Colloid and Interface Science*, 465: 158 – 164, 2016.

[45] J. W. O. Salari, J. van Heck, and B. Klumperman. Steric stabilization of pickering emulsions for the efficient synthesis of polymeric microcapsules. *Langmuir*, 26(18): 14929–14936, 2010.

[46] J. H. J. Thijssen and J. Vermant. Interfacial rheology of model particles at liquid interfaces and its relation to (bicontinuous) pickering emulsions. *Journal of Physics: Condensed Matter*, 30(2): 023002, 2017.

[47] O. S. Deshmukh, D. van den Ende, M. C. Stuart, F. Mugele, and M. H. Duits. Hard and soft colloids at fluid interfaces: Adsorption, interactions, assembly & rheology. *Advances in Colloid and Interface Science*, 222: 215 – 227, 2015.

[48] M. Hermes and P. S. Clegg. Yielding and flow of concentrated pickering emulsions. *Soft Matter*, 9: 7568–7575, 2013.

[49] S. Frijters, F. Gunther, and J. Harting. Effects of nanoparticles and surfactant on droplets in shear flow. *Soft Matter*, 8(24): 6542–6556, 2012.

[50] M. Cui, T. Emrick, and T. P. Russell. Stabilizing liquid drops in nonequilibrium shapes by the interfacial jamming of nanoparticles. *Science*, 342(6157): 460–463, 2013.

[51] R. van Hooghten, V. E. Blair, A. Vananroye, A. B. Schofield, J. Vermant, and J. H. J. Thijssen. Interfacial rheology of sterically stabilized colloids at liquid interfaces and its effect on the stability of pickering emulsions. *Langmuir*, 33(17): 4107–4118, 2017.

[52] A. Maestro, E. Santini, D. Zabiegaj, S. Llamas, F. Ravera, L. Liggieri, F. Ortega, R. G. Rubio, and E. Guzman. Particle and Particle-Surfactant Mixtures at Fluid Interfaces: Assembly, Morphology, and Rheological Description. *Advances in Condensed Matter Physics*, 2015.

[53] R. F. Lee. Agents which promote and stabilize water-in-oil emulsions. *Spill Science and Technology Bulletin*, 5(2): 117 – 126, 1999.

[54] V. Rajaković and D. Skala. Separation of water-in-oil emulsions by freeze/thaw method and microwave radiation. *Separation and Purification Technology*, 49(2): 192 – 196, 2006.

[55] J. Zhang, J. Li, R. W. Thring, X. Hu, and X. Song. Oil recovery from refinery oily sludge via ultrasound and freeze/thaw. *Journal of Hazardous materials*, 203204(0): 195 – 203, 2012.

[56] Langevin, D., Poteau, S., Hénaut, I., and Argillier, J. F. Crude oil emulsion properties and their application to heavy oil transportation. *Oil & Gas Science and Technology - Rev. IFP*, 59(5): 511–521, 2004.

[57] B. M. Degner, C. Chung, V. Schlegel, R. Hutkins, and D. J. McClements. Factors influencing the freeze-thaw stability of emulsion-based foods. *Comprehensive Reviews in Food Science and Food Safety*, 13(2): 98–113, 2014.

[58] E. Dickinson. Interfacial particles in food emulsions and foams. In B. Binks and T. Horozov, editors, *Colloidal Particles at Liquid Interfaces*, pages 298–327. Cambridge University Press, Cambridge, 2006.

[59] J. E. Norton and I. T. Norton. Designer colloids-towards healthy everyday foods? *Soft Matter*, 6: 3735–3742, 2010.

[60] D. Wadhera and E. D. Capaldi-Phillips. A review of visual cues associated with food on food acceptance and consumption. *Eating Behaviors*, 15(1): 132 – 143, 2014.

[61] P. Wongkongkatep, K. Manopwisedjaroen, P. Tiposoth, S. Archakunakorn, T. Pongtharangkul, M. Suphantharika, K. Honda, I. Hamachi, and J. Wongkongkatep. Bacteria interface pickering emulsions stabilized by self-assembled bacteria-chitosan network. *Langmuir*, 28(13): 5729–5736, 2012.

[62] S. Melle, M. Lask, and G. G. Fuller. Pickering emulsions with controllable stability. *Langmuir*, 21(6): 2158–2162, 2005.

[63] T. N. Hunter, R. J. Pugh, G. V. Franks, and G. J. Jameson. The role of particles in stabilising foams and emulsions. *Advances in Colloid and Interface Science*, 137: 57 – 81, 2008.

[64] B. Li and D. Sun. Novel methods for rapid freezing and thawing of foods - a review. *Journal of Food Engineering*, 54(3): 175 – 182, 2002.

[65] A. Hottot, S. Vessot, and J. Andrieu. Freeze drying of pharmaceuticals in vials: Influence of freezing protocol and sample configuration on ice morphology and freeze-dried cake texture. *Chemical Engineering and Processing: Process Intensification*, 46(7): 666 – 674, 2007.

[66] E. J. Chamberlain. Overconsolidation effects of ground freezing. *Engineering Geology*, 18(1): 97 – 110, 1981.

[67] C. Linke and S. Drusch. Pickering emulsions in foods - opportunities and limitations. *Critical Reviews in Food Science and Nutrition*, 58(12): 1971–1985, 2018.

[68] A. Pawlik, D. Kurukji, I. Norton, and F. Spyropoulos. Food-grade pickering emulsions stabilised with solid lipid particles. *Food & Function*, 7: 2712–2721, 2016.

[69] R. George. Freezing proceseses used in the food industry. *Trends Food Sci. Technol.*, 4: 134 – 138, 1993.

[70] R. W. Hartel. Crystallization in foods. In A. S. Myerson, editor, *Handbook of Industrial Crystallization*, pages 287 – 304. Butterworth-Heinemann, Woburn, second edition, 2002.

[71] G. L. Cramp, A. M. Docking, S. Ghosh, and J. N. Coupland. On the stability of oil-in-water emulsions to freezing. *Food Hydrocolloids*, 18(6): 899–905, 2004.

[72] R. W. Hartel. Ice crystallization during the manufacture of ice cream. *Trends in Food Science & Technology*, 7(10): 315 – 321, 1996.

[73] S. Ghosh and J. Coupland. Factors affecting the freezethaw stability of emulsions. *Food Hydrocolloids*, 22: 105–111, 2008.

[74] E. Magnusson, C. Rosén, and L. Nilsson. Freezethaw stability of mayonnaise type oil-in-water emulsions. *Food Hydrocolloids*, 25(4): 707 – 715, 2011.

[75] C. Lin, G. He, C. Dong, H. Liu, G. Xiao, and Y. Liu. Effect of oil phase transition on freeze/thaw-induced demulsification of water-in-oil emulsions. *Langmuir*, 24(10): 5291–5298, 2008.

[76] M. Rayner, D. Marku, M. Eriksson, M. Sjöö, P. Dejmek, and M. Wahlgren. Biomass-based particles for the formulation of pickering type emulsions in food and topical applications. *Colloids and Surfaces, A: Physicochemical and Engineering Aspects*, 458(0): 48 – 62, 2014. Formula VII: How Does Your Formulation Work?

[77] P. Thanasukarn, R. Pongsawatmanit, and D. McClements. Influence of emulsifier type on freeze-thaw stability of hydrogenated palm oil-in-water emulsions. *Food Hydrocolloids*, 18(6): 1033 – 1043, 2004.

[78] P. Thanasukarn, R. Pongsawatmanit, and D. J. McClements. Utilization of layer-by-layer interfacial deposition technique to improve freezethaw stability of oil-in-water emulsions. *Food Research International*, 39(6): 721 – 729, 2006.

[79] T. Aoki, E. A. Decker, and D. McClements. Influence of environmental stresses on stability of o/w emulsions containing droplets stabilized by multilayered membranes produced by a layer-by-layer electrostatic deposition technique. *Food Hydrocolloids*, 19(2): 209 – 220, 2005.

[80] S. Ariyaprakai and K. Tananuwong. Freeze-thaw stability of edible oil-in-water emulsions stabilized by sucrose esters and Tweens. *Journal of Food Engineering*, 152: 57–64, 2015.

[81] P. Spicer and R. Hartel. Crystal comets: Dewetting during emulsion droplet crystallization. *Australian Journal of Chemistry*, 58(9): 655–659, 2005.

[82] F. Donsì, Y. Wang, and Q. Huang. Freezethaw stability of lecithin and modified starch-based nanoemulsions. *Food Hydrocolloids*, 25(5): 1327 – 1336, 2011.

[83] Y.-B. Chen, X.-F. Zhu, T.-X. Liu, W.-F. Lin, C.-H. Tang, and R. Liu. Improving freeze-thaw stability of soy nanoparticle-stabilized emulsions through increasing particle size and surface hydrophobicity. *Food Hydrocolloids*, 87: 404 – 412, 2019.

[84] B. Zeeb, H. Salminen, L. Fischer, and J. Weiss. Impact of heat and laccase on the ph and freeze-thaw stability of oil-in-water emulsions stabilized by adsorbed biopolymer nanoparticles. *Food Biophysics*, 9(2): 125–137, Jun 2014.

[85] A. Marefati, M. Sjöö, A. Timgren, P. Dejmek, and M. Rayner. Fabrication of encapsulated oil powders from starch granule stabilized w/o/w pickering emulsions by freeze-drying. *Food Hydrocolloids*, 51: 261 – 271, 2015.

[86] Z. Hu, H. S. Marway, H. Kasem, R. Pelton, and E. D. Cranston. Dried and redispersible cellulose nanocrystal pickering emulsions. *ACS Macro Letters*, 5(2): 185–189, 2016.

[87] R. A. L. Jones. *Soft Condensed Matter*. OUP Oxford, 2002.

[88] D. Erdemir, A. Y. Lee, and A. S. Myerson. Nucleation of crystals from solution: Classical and two-step models. *Accounts of Chemical Research*, 42(5): 621–629, 2009.

[89] R. P. Sear. Nucleation: theory and applications to protein solutions and colloidal suspensions. *Journal of Physics: Condensed Matter*, 19(3): 033101, 2007.

[90] D. W. Oxtoby. Homogeneous nucleation: theory and experiment. *Journal of Physics: Condensed Matter*, 4(38): 7627, 1992.

[91] D. Turnbull. Kinetics of heterogeneous nucleation. *The Journal of Chemical Physics*, 18(2): 198–203, 1950.

[92] A. I. Campbell and P. Bartlett. Fluorescent hard-sphere polymer colloids for confocal microscopy. *Journal of Colloid and Interface Science*, 256(2): 325 – 330, 2002.

[93] NIH. Imagej. date accessed: 14 February 2018.

[94] J. H. J. Thijssen, A. B. Schofield, and P. S. Clegg. How do (fluorescent) surfactants affect particle-stabilized emulsions? *Soft Matter*, 7: 7965–7968, 2011.

[95] V. Gun'ko, V. Zarko, R. Leboda, and E. Chibowski. Aqueous suspension of fumed oxides: particle size distribution and zeta potential. *Advances in Colloid and Interface Science*, 91(1): 1 – 112, 2001.

[96] J. Giermanska-Kahn, V. Schmitt, B. P. Binks, and F. Leal-Calderon. A new method to prepare monodisperse pickering emulsions. *Langmuir*, 18(7): 2515–2518, 2002.

[97] B. P. Binks and M. Kirkland. Interfacial structure of solid-stabilised emulsions studied by scanning electron microscopy. *Physical Chemistry Chemical Physics*, 4: 3727–3733, 2002.

[98] E. Dickinson. Food emulsions and foams: Stabilization by particles. *Current Opinion in Colloid and Interface Science*, 15(12): 40 – 49, 2010.

[99] I. Tavernier, W. Wijaya, P. V. der Meeren, K. Dewettinck, and A. R. Patel. Food-grade particles for emulsion stabilization. *Trends in Food Science & Technology*, 50: 159 – 174, 2016.

[100] A. Yusoff and B. S. Murray. Modified starch granules as particle-stabilizers of oil-in-water emulsions. *Food Hydrocolloids*, 25(1): 42 – 55, 2011.

[101] E. Dickinson. Use of nanoparticles and microparticles in the formation and stabilization of food emulsions. *Trends Food Sci. Technol.*, 24, 2012.

[102] G. Bosma, C. Pathmamanoharan, E. d. Hoog, A. v. Kegel, W.K.and Blaaderen, and H. Lekkerkerker. Preparation of monodisperse, fluorescent pmma-latex colloids by dispersion polymerization. *Journal of Colloid and Interface Science*, 245(2): 292 – 300, 2002.

[103] N. Ghoneim. Photophysics of nile red in solution: Steady state spectroscopy. *Spectrochimica Acta Part A: Molecular and Biomolecular Spectroscopy*, 56(5): 1003 – 1010, 2000.

[104] A. G. Gilani, M. Moghadam, and M. Zakerhamidi. Solvatochromism of nile red in anisotropic media. *Dyes and Pigments*, 92(3): 1052 – 1057, 2012.

[105] Thermo Fisher Scientific. Fluorescence SpectraViewer. date accessed: 30 November 2018.

[106] C. Sheppard and D. Shotton. *Confocal Laser Scanning Microscopy*. BIOS Scientific Publishers, Oxford, 1997.

[107] D. Dedovets, C. Monteux, and S. Deville. A temperature-controlled stage for laser scanning confocal microscopy and case studies in chemistry of materials. *Ultramicroscopy*, 195: 1–11, 2018.

[108] V. E. Centonze and J. G. White. Multiphoton excitation provides optical sections from deeper within scattering specimens than confocal imaging. *Biophysical Journal*, 75(4): 2015 – 2024, 1998.

[109] J. T. Gonçalves and R. Mostany. Intravital two-photon excitation microscopy in neuroscience: General concepts and applications. In R. Weigert, editor, *Advances in Intravital Microscopy: From Basic to Clinical Research*, pages 1–23. Springer Netherlands, 2014.

[110] K. Svoboda and R. Yasuda. Principles of two-photon excitation microscopy and its applications to neuroscience. *Neuron*, 50(6): 823 – 839, 2006.

[111] M. D. Larrañga, R. J. Lewis, and R. A. Lewis, editors. *Hawley's Condensed Chemical Dictionary*. Wiley, 16th edition, 2016.

[112] Sigma-Aldrich. n-hexadecane. Date accessed: 8 Feb 2018.

[113] J. O'Regan and D. Mulvihill. Heat stability and freeze-thaw stability of oil-in-water emulsions stabilised by sodium caseinate-maltodextrin conjugates. *Food Chemistry*, 2010.

[114] S. Ghosh and D. Rousseau. Freeze-thaw stability of water-in-oil emulsions. *Journal of Colloid and Interface Science*, 339(1): 91–102, 2009.

[115] W. L. Kerr and D. S. Reid. Thermodynamics and frozen foods. *The Physics Teacher*, 31(1): 52–55, 1993.

[116] H. Zhang, I. Hussain, M. Brust, M. Butler, S. Rannard, and A. Cooper. Aligned two- and three-dimensional structures by directional freezing of polymers and nanoparticles. *Nature Materials*, 4(10): 787–793, 2005.

[117] J. D. Hunt, K. A. Jackson, and H. Brown. Temperature gradient microscope stage suitable for freezing materiasl with melting points between -100 and +200 degrees c. *Review of Scientific Instruments*, 37(6): 805–&, 1966.

[118] W. L. Li, K. Lu, and J. Y. Walz. Freeze casting of porous materials: review of critical factors in microstructure evolution. *International Materials Reviews*, 57(1): 37–60, 2012.

[119] K. Cook and R. Hartel. Mechanisms of ice crystallization in ice cream production. *Comprehensive Reviews in Food Science and Food Safety*, 9(2): 213–222, 2010.

[120] COMSOL Inc. COMSOL. Date accessed: 11 October 2018.

[121] S. Deville. Freeze-casting of porous ceramics: A review of current achievements and issues. *Advanced Engineering Materials*, 10(3): 155–169, 2008.

[122] C. Vélez, M. Khayet, and J. O. de Zárate. Temperature-dependent thermal properties of solid/liquid phase change even-numbered n-alkanes: n-hexadecane, n-octadecane and n-eicosane. *Applied Energy*, 143: 383 – 394, 2015.

[123] DDBST GmbH. Dortmund Data Bank. Date accessed: 16 May 2018.

[124] G. S. Parks, G. E. Moore, M. L. Renquist, B. F. Naylor, L. A. McClaine, P. S. Fujii, and J. A. Hatton. Thermal data on organic compounds. xxv. some heat capacity, entropy and free energy data for nine hydrocarbons of high molecular weight. *Journal of the American Chemical Society*, 71(10): 3386–3389, 1949.

[125] S. Outcalt, A. Laesecke, and T. J. Fortin. Density and speed of sound measurements of hexadecane. *The Journal of Chemical Thermodynamics*, 42(6): 700 – 706, 2010.

[126] S. J. Ball and J. P. M. Trusler. Speed of sound of n-hexane and n-hexadecane at temperatures between 298 and 373 k and pressures up to 100 mpa. *International Journal of Thermophysics*, 22(2): 427–443, Mar 2001.

[127] P. Aussillous and D. Quéré. Liquid marbles. *Nature*, 411(6840): 924–927, 2001.

[128] O. D. Velev, K. Furusawa, and K. Nagayama. Assembly of latex particles by using emulsion droplets as templates. 1. microstructured hollow spheres. *Langmuir*, 12(10): 2374–2384, 1996.

[129] A. D. Dinsmore, M. F. Hsu, M. G. Nikolaides, M. Marquez, A. R. Bausch, and D. A. Weitz. Colloidosomes: Selectively permeable capsules composed of colloidal particles. *Science*, 298(5595): 1006–1009, 2002.

[130] K. L. Thompson, M. Williams, and S. P. Armes. Colloidosomes: Synthesis, properties and applications. *Journal of Colloid and Interface Science*, 447: 217 – 228, 2015.

[131] S. S. Datta, H. C. Shum, and D. A. Weitz. Controlled buckling and crumpling of nanoparticle-coated droplets. *Langmuir*, 26(24), 2010.

[132] F. Sicard and A. Striolo. Buckling in armored droplets. *Nanoscale*, 9: 8567–8572, 2017.

[133] H. Xu, S. Melle, K. Golemanov, and G. Fuller. Shape and buckling transitions in solid-stabilized drops. *Langmuir*, 21(22): 10016–10020, 2005.

[134] M. K. Mulligan and J. P. Rothstein. Deformation and breakup of micro- and nanoparticle stabilized droplets in microfluidic extensional flows. *Langmuir*, 27(16): 9760–9768, 2011.

[135] L. Bécu and L. Benyahia. Strain-induced droplet retraction memory in a pickering emulsion. *Langmuir*, 25(12): 6678–6682, 2009.

[136] Y. Mei, G. Li, P. Moldenaers, and R. Cardinaels. Dynamics of particle-covered droplets in shear flow: unusual breakup and deformation hysteresis. *Soft Matter*, 12: 9407–9412, 2016.

[137] C. Jordan, V. V. Shuvaev, M. Bailey, V. R. Muzykantov, and T. D. Dziubla. The Role of Carrier Geometry in Overcoming Biological Barriers to Drug Delivery. *Current Pharmaceutical Design*, 22(9): 1259–1273, 2016.

[138] E. A. Simone, T. D. Dziubla, and V. R. Muzykantov. Polymeric carriers: role of geometry in drug delivery. *Expert Opinion in Drug Deliver*, 5(12): 1283–1300, 2008.

[139] L. Wu, Z. Liao, M. Liu, X. Yin, X. Li, M. Wang, X. Lu, N. Lv, V. Singh, Z. He, H. Li, and J. Zhang. Fabrication of non-spherical pickering emulsion droplets by cyclodextrins mediated molecular self-assembly. *Colloids and Surfaces A: Physicochemical and Engineering Aspects*, 490: 163 – 172, 2016.

[140] S. A. Bon, S. D. Mookhoek, P. J. Colver, H. R. Fischer, and S. van der Zwaag. Route to stable non-spherical emulsion droplets. *European Polymer Journal*, 43(11): 4839 – 4842, 2007.

[141] A. R. Studart, H. C. Shum, and D. A. Weitz. Arrested coalescence of particle-coated droplets into nonspherical supracolloidal structures. *The Journal of Physical Chemistry B*, 113(12): 3914–3919, 2009.

[142] S.-H. Kim, C.-J. Heo, S. Y. Lee, G.-R. Yi, and S.-M. Yang. Polymeric particles with structural complexity from stable immobilized emulsions. *Chemistry of Materials*, 19(19): 4751–4760, 2007.

[143] H.-L. Cheng and S. S. Velankar. Controlled jamming of particle-laden interfaces using a spinning drop tensiometer. *Langmuir*, 25(8): 4412–4420, 2009.

[144] M. Allaby, editor. *A Dictionary of Geology and Earth Sciences*. Oxford University Press, fourth edition, 2013.

[145] A. Hashmi, A. Strauss, and J. Xu. Freezing of a liquid marble. *Langmuir*, 28(28): 10324–10328, 2012.

[146] N. Denkov, S. Tcholakova, I. Lesov, D. Cholakova, and S. K. Smoukov. Self-shaping of oil droplets via the formation of intermediate rotator phases upon cooling. *Nature*, 528(7582): 392+, 2015.

[147] E. W. Weisstein. *CRC Concise Encyclopedia of Mathematics*. Chapman & Hall /CRC, second edition, 2003. Pages 107, 894 and 1546.

[148] H. G. Merkus. *Particle Size, Size Distributions and Shape*, pages 13–42. Springer Netherlands, Dordrecht, 2009.

[149] S. Ramanujan. Modular equations and approximations to π. In G. Hardy, P. Seshu Aiyar, and B. Wilson, editors, *Collected Papers of Srinivasa Ramanujan*. AMS Chelsea Publishing, Providence, Rhode Island, 2000.

[150] S. O. Asekomhe, R. Chiang, J. H. Masliyah, and J. A. W. Elliott. Some observations on the contraction behavior of a water-in-oil drop with attached solids. *Industrial and Engineering Chemistry Research*, 44(5): 1241–1249, 2005.

[151] H. C. Shum, A. R. Abate, D. Lee, A. R. Studart, B. Wang, C.-H. Chen, J. Thiele, R. K. Shah, A. Krummel, and D. A. Weitz. Droplet microfluidics for fabrication of non-spherical particles. *Macromolecular Rapid Communications*, 31(2): 108–118, 2010.

[152] S. J. Mashl, R. A. Flores, and R. Trivedi. Dynamics of solidification in 2% corn starch-water mixtures: Effect of variations in freezing rate on product homogeneity. *Journal of Food Science*, 61(4): 760–765, 1996.

[153] D. Dedovets, C. Monteux, and S. Deville. Five-dimensional imaging of freezing emulsions with solute effects. *Science*, 360(6386): 303–306, 2018.

[154] R. Asthana and S. N. Tewari. The engulfment of foreign particles by a freezing interface. *Journal of Materials Science*, 28(20): 5414–5425, 1993.

[155] M. K. Lee, N.-O. Chung, and J. Lee. Membranes with through-thickness porosity prepared by unidirectional freezing. *Polymer*, 51(26): 6258 – 6267, 2010.

[156] P. J. Parker, A. G. Collins, and J. P. Dempsey. Effects of freezing rate, solids content, and curing time on freeze/thaw conditioning of water treatment residuals. *Environmental Science & Technology*, 32(3): 383–387, 1998.

[157] W. Mahler and M. Bechtold. Freeze-formed silica fibers. *Nature*, 285(5759): 27–28, 1980.

[158] H. Zhang and A. Cooper. Aligned porous structures by directional freezing. *Advanced Materials*, 19(11): 1529–1533, 2007.

[159] J. M. H. Schollick, R. W. Style, A. Curran, J. S. Wettlaufer, E. R. Dufresne, P. B. Warren, K. P. Velikov, R. P. A. Dullens, and D. G. A. L. Aarts. Segregated ice growth in a suspension of colloidal particles. *The Journal of Physical Chemistry B*, 120(16): 3941–3949, 2016.

[160] Y. Zhu, R. Zhang, S. Zhang, Y. Chu, and J. Chen. Macroporous polymers with aligned microporous walls from pickering high internal phase emulsions. *Langmuir*, 32(24): 6083–6088, 2016.

[161] U. G. K. Wegst, M. Schecter, A. E. Donius, and P. M. Hunger. Biomaterials by freeze casting. *Philosophical Transactions of the Royal Society of London A: Mathematical, Physical and Engineering Sciences*, 368(1917): 2099–2121, 2010.

[162] B. Rubinsky and M. Ikeda. A cryomicroscope using directional solidification for the controlled freezing of biological material. *Cryobiology*, 22(1): 55 – 68, 1985.

[163] C. Namperumal. A new cryostage design for cryomicroscopy. *Journal of Microscopy*, 192(2): 202–211, 2008.

[164] P. J. Fellows. *Food Processing Technology Principles and Practice*. Woodhead Publishing, Duxford, fourth edition, 2016.

[165] L. Zheng and D. Sun. Innovative applications of power ultrasound during food freezing processesa review. *Trends in Food Science & Technology*, 17(1): 16 – 23, 2006.

[166] P. Dempsey and P. Bansal. The art of air blast freezing: Design and efficiency considerations. *Applied Thermal Engineering*, 41: 71 – 83, 2012.

[167] R. Dash, Y. Li, and A. J. Ragauskas. Cellulose nanowhisker foams by freeze casting. *Carbohydrate Polymers*, 88(2): 789 – 792, 2012.

[168] S. Deville, E. Saiz, R. K. Nalla, and A. P. Tomsia. Freezing as a path to build complex composites. *Science*, 311(5760): 515–518, 2006.

[169] Y. Chino and D. C. Dunand. Directionally freeze-cast titanium foam with aligned, elongated pores. *Acta Materialia*, 56(1): 105 – 113, 2008.

[170] D. J. McClements. *Food Emulsions: Principles, Practices and Techniques*. CRC Press, second edition, 2004.

[171] D. R. Uhlmann, B. Chalmers, and K. A. Jackson. Interaction between particles and a solidliquid interface. *Journal of Applied Physics*, 35(10): 2986–2993, 1964.

[172] C. Körber, G. Rau, M. Cosman, and E. Cravalho. Interaction of particles and a moving ice-liquid interface. *Journal of Crystal Growth*, 72(3): 649 – 662, 1985.

[173] M. Worster and J. Wettlaufer. The fluid mechanics of premelted liquid films. In W. Shyy and R. Narayanan, editors, *Fluid Dynamics at Interfaces*. Cambridge University Press, Cambridge, United Kingdom, 1999.

[174] J. M. H. Schollick. *Real space study of pattern formation in freezing colloidal suspensions*. PhD thesis, University of Oxford, 2015.

[175] Sigma-Aldrich. n-dodecane. Date accessed: 24 Jan 2019.

[176] J. H. J. Thijssen and P. S. Clegg. Demixing, remixing and cellular networks in binary liquids containing colloidal particles. *Soft Matter*, 6: 1182–1190, 2010.

[177] Y. Zou, Z. Wan, J. Guo, J. Wang, S. Yin, and X. Yang. Modulation of the surface properties of protein particles by a surfactant for stabilizing foams. *RSC Advances*, 6: 66018–66026, 2016.

[178] E. Rio, W. Drenckhan, A. Salonen, and D. Langevin. Unusually stable liquid foams. *Advances in Colloid and Interface Science*, 205: 74 – 86, 2014.

[179] D. J. French, P. Taylor, J. Fowler, and P. S. Clegg. Making and breaking bridges in a pickering emulsion. *Journal of Colloid and Interface Science*, 441: 30 – 38, 2015.

[180] J. M. Belman-Flores, S. Ledesma, A. Gallegos-Munoz, and D. Hernandez. Thermal Simulation of the Fresh Food Compartment in a Domestic Refrigerator. *Energies*, 10(1), 2017.

[181] S. James, J. Evans, and C. James. A review of the performance of domestic refrigerators. *Journal of Food Engineering*, 87(1): 2 – 10, 2008.

[182] D. C. Connell and J. M. C. Tombs. The crystallization pressure of ice – a simple experiment. *Journal of Glaciology*, 10: 312–315, 1971.

[183] S. Meyer, C. Song, Y. Jin, K. Wang, and H. A. Makse. Jamming in two-dimensional packings. *Phys. A (Amsterdam, Neth.)*, 389: 5137 – 5144, 2010.

[184] A. Regand and H. Goff. Structure and ice recrystallization in frozen stabilized ice cream model systems. *Food Hydrocolloids*, 17(1): 95 – 102, 2003.

[185] S. Adapa, K. A. Schmidt, I. J. Jeon, T. J. Herald, and R. A. Flores. Mechanisms of ice crystallization and recrystallization in ice cream: A review. *Food Reviews International*, 16(3): 259–271, 2000.

[186] F. Broto and D. Clausse. A study of the freezing of supercooled water dispersed within emulsions by differential scanning calorimetry. *Journal of Physics C: Solid State Physics*, 9(23): 4251–4257, dec 1976.

[187] S. A. Bari and J. Hallett. Nucleation and growth of bubbles at an ice-water interface. *Journal of Glaciology*, 13(69): 48–520, 1974.

[188] K. A. Rumble, J. H. J. Thijssen, A. B. Schofield, and P. S. Clegg. Compressing a spinodal surface at fixed area: bijels in a centrifuge. *Soft Matter*, 12: 4375–4383, 2016.

[189] L. E. Scriven. Micellization, solubilization, and microemulsions. In K. L. Mittal, editor, *Micellization, Solubilization, and Microemulsions: Volume 2*, chapter Equilibrium Bicontinuous Structures, pages 877–893. Springer US, Boston, MA, 1977.

[190] M. E. Cates and P. S. Clegg. Bijels: a new class of soft materials. *Soft Matter*, 4: 2132–2138, 2008.

[191] K. Stratford, R. Adhikari, I. Pagonabarraga, J. Desplat, and M. E. Cates. Colloidal jamming at interfaces: A route to fluid-bicontinuous gels. *Science*, 309(5744): 2198–2201, 2005.

[192] E. Herzig, K. White, A. Schofield, W. Poon, and P. Clegg. Bicontinuous emulsions stabilized solely by colloidal particles. *Nature Materials*, 6(12): 966–971, 2007.

[193] H.-Y. Chen, Y. Kwon, and K. Thornton. Multifunctionality of three-dimensional self-assembled composite structure. *Scripta Materialia*, 61(1): 52 – 55, 2009.

[194] M. Martina, G. Subramanyam, J. C. Weaver, D. W. Hutmacher, D. E. Morse, and S. Valiyaveettil. Developing macroporous bicontinuous materials as scaffolds for tissue engineering. *Biomaterials*, 26(28): 5609 – 5616, 2005.

[195] M. N. Lee and A. Mohraz. Hierarchically porous silver monoliths from colloidal bicontinuous interfacially jammed emulsion gels. *Journal of the American Chemical Society*, 133(18): 6945–6947, 2011.

[196] D. Cai, F. H. Richter, J. H. J. Thijssen, P. G. Bruce, and P. S. Clegg. Direct transformation of bijels into bicontinuous composite electrolytes using a pre-mix containing lithium salt. *Materials Horizons*, 5: 499–505, 2018.

[197] H. Firoozmand and D. Rousseau. Food-grade bijels based on gelatin-maltodextrin-microbial cell composites. *Food Hydrocolloids*, 48: 208 – 212, 2015.

[198] M. Reeves, A. T. Brown, A. B. Schofield, M. E. Cates, and J. H. J. Thijssen. Particle-size effects in the formation of bicontinuous pickering emulsions. *Physical Review E*, 92: 032308, Sep 2015.

[199] A. Mohraz. Interfacial routes to colloidal gelation. *Current Opinion in Colloid & Interface Science*, 25: 89 – 97, 2016.

[200] J. W. Tavacoli, J. H. J. Thijssen, and P. S. Clegg. Bicontinuous emulsions stabilized by colloidal particles. In *Particle-Stabilized Emulsions and Colloids: Formation and Applications*, pages 129–168. The Royal Society of Chemistry, 2015.

[201] M. F. Haase, K. J. Stebe, and D. Lee. Continuous fabrication of hierarchical and asymmetric bijel microparticles, fibers, and membranes by solvent transfer-induced phase separation (strips). *Advanced Materials*, 27(44): 7065–7071, 2015.

[202] D. Cai, P. S. Clegg, T. Li, K. A. Rumble, and J. W. Tavacoli. Bijels formed by direct mixing. *Soft Matter*, 13: 4824–4829, 2017.

[203] J. K. Ferri, P. Carl, N. Gorevski, T. P. Russell, Q. Wang, A. Boeker, and A. Fery. Separating membrane and surface tension contributions in Pickering droplet deformation. *Soft Matter*, 4(11): 2259–2266, 2008.

[204] E. Kim, K. Stratford, R. Adhikari, and M. E. Cates. Arrest of fluid demixing by nanoparticles: A computer simulation study. *Langmuir*, 24(13): 6549–6556, 2008.

[205] M. E. Glicksman. *Principles of Solidification*. Springer-Verlag New York, 2011.

[206] K. Jackson and J. Hunt. Transparent compounds that freeze like metals. *Acta Metallurgica*, 13(11): 1212 – 1215, 1965.

[207] K. Araki and J. W. Halloran. Porous ceramic bodies with interconnected pore channels by a novel freeze casting technique. *Journal of the American Ceramic Society*, 88(5): 1108–1114, 2005.

[208] H. Ishiguro and B. Rubinsky. Mechanical interactions between ice crystals and red blood cells during directional solidification. *Cryobiology*, 31(5): 483 – 500, 1994.

[209] M. F. Butler. Instability formation and directional dendritic growth of ice studied by optical interferometry. *Crystal Growth and Design*, 1(3): 213–223, 2001.

[210] S. S. L. Peppin, J. S. Wettlaufer, and M. G. Worster. Experimental verification of morphological instability in freezing aqueous colloidal suspensions. *Physical Review Letters*, 100: 238301, 2008.

[211] S. S. Peppin, M. G. Worster, and J. Wettlaufer. Morphological instability in freezing colloidal suspensions. *Proceedings of the Royal Society A: Mathematical, Physical and Engineering Sciences*, 463(2079): 723–733, 2007.

[212] J. You, L. Wang, Z. Wang, J. Li, J. Wang, X. Lin, and W. Huang. Interfacial undercooling in solidification of colloidal suspensions: analyses with quantitative measurements. *Scientific reports*, 6: 28434, 2016.

[213] S. Vandebril, A. Franck, G. Fuller, P. Moldenaers, and J. Vermant. A double wall-ring geometry for interfacial shear rheometry. *Rheologica Acta*, 49(2), 2010.

[214] R. H. Ewoldt and G. H. McKinley. 4 creep ringing in rheometry or how to deal with oft-discarded data in step stress tests ! *Rheology Bulletin*, 76: 4–6, 2007.

[215] TA Instruments. Interfacial rheology - interfacial geometries. Date accessed: 8 March 2019.